The Dissertation Committee for Ahmed Kord Certifies that this is the approved version of the following Dissertation:

Magnetless Circulators Based on Linear Time-Varying Circuits

Committee:

Andrea Alù, Supervisor

Ranjit Gharpurey

Daniel Wasserman

Sriram Vishwanath

Harish Krishnaswamy

Magnetless Circulators Based on Linear Time-Varying Circuits

by

Ahmed Kord

Dissertation

Presented to the Faculty of the Graduate School of
The University of Texas at Austin
in Partial Fulfillment
of the Requirements
for the Degree of

Doctor of Philosophy

The University of Texas at Austin
May 2019

Dedication

To my family.

Acknowledgements

The pursuit of knowledge through independent and free thinking is in my opinion the most meaningful way to spend life. Scientific research in particular not only leads the enlightenment of mankind as a whole but it also, and most importantly, unveils some order in this seemingly absurd existence of ours, which consoles the anxious soul and satisfies the curious mind of the individual who undertakes this mission and considers it his own purpose of life. I am fortunate enough to have been enjoying this experience over the past few years and to be crowning it with a doctor of *philosophy* in electrical engineering. For this and for everything, I shall be thankful and forever beholden to Allah.

I am also indebted to many people who helped me grow into the human being I am today. First and foremost, I am wholeheartedly grateful to Prof. Andrea Alù for being my supervisor. He inundated me with invaluable guidance and provided me with everything I needed to fulfil my goals. I sincerely could have never wished for a better advisor. I should also extend my gratitude to Prof. Dimitrios Sounas of Wayne State University for being my mentor and my dear friend. His insightful comments were priceless in refining my thinking and in enhancing the quality of my work. I also would like to thank Prof. Harish Krishnaswamy of Columbia University, Prof. Ranjit Gharpurey of the University of Texas at Austin, and Prof. Matteo Rinaldi of Northeastern University for the useful discussions I had with them. I must also thank my parents without whom I would not have been able to make this achievement nor I would have even existed, to begin with. Lastly but not least, I would like to thank my friends and colleagues for all the good times we spent together and the precious moments we shared. This was an amazing journey and I have reached its final destination, thrilled, contented, and more eager than ever to explore what comes next!

Abstract

Magnetless Circulators Based on Linear Time-Varying Circuits

Ahmed Kord, Ph.D.
The University of Texas at Austin, 2019

Supervisor: Andrea Alù

In a crowded electromagnetic spectrum with an ever-increasing demand for higher data rates to enable multimedia-rich applications and services, an efficient use of the available wireless resources becomes crucial. For this reason, full-duplex communication, which doubles the transmission rate over a certain bandwidth compared to currently deployed half-duplex radios by operating the uplink and the downlink simultaneously on the same frequency, has been brought back into the spotlight after decades of being presumed impractical. This long-held assumption has been particularly due to the lack of high performance low-cost and small-size circulators that could mitigate the strong self-interference at the RF frontend interface of full-duplex transceivers while, at the same time, permitting low-loss bi-directional communication using a single antenna. Traditionally, such non-reciprocal components were almost exclusively based on magnetic biasing of rare-earth ferrite materials, which results in bulky and expensive devices that are not suitable for the vast majority of commercial systems. Despite significant research efforts over the past few decades, none of the previous works managed to eliminate the magnet while satisfying all the challenging requirements dictated by the standards of real systems. In this dissertation, we introduce several newly invented magnetless circulators based on linear time-varying circuits that can overcome for the first time the limitations of all previous approaches. We analyze the presented circuits rigorously and validate them through simulations and measurements, showing unprecedented performance in all relevant metrics, thus holding the promise to enable full-duplex radios in the near future.

Table of Contents

List of Tables

List of Figures

Chapter 1: Introduction

> Truth that has been merely learned is like an artificial limb, a false tooth, a waxen nose; at best, like a nose made out of another's flesh; it adheres to us only because it is put on. But truth acquired by thinking of our own is like a natural limb; it alone really belongs to us. This is the fundamental difference between the thinker and the mere man of learning. The intellectual attainments of a man who thinks for himself resemble a fine painting, where the light and shade are correct, the tone sustained, the color perfectly harmonized; it is true to life. On the other hand, the intellectual attainments of the mere man of learning are like a large palette, full of all sorts of colors, which at most are systematically arranged, but devoid of harmony, connection and meaning.
>
> Arthur Schopenhauer

1.1 FULL-DUPLEX COMMUNICATION

Modern communication networks are targeting tremendous increases in data rates to satisfy an ever-growing demand for faster and more efficient connectivity. Nevertheless, traditional sub 6 GHz bands of today’s systems have become crowded with plenty of indoor and outdoor services, thus making it difficult to satisfy the new throughput requirements. To overcome this problem, the consensus over the past few years has been to shift to higher frequencies, where wideband unlicensed spectrum is still available. However, electromagnetic (EM) waves at such frequencies are less capable of penetrating obstructions, thus reducing the area covered by each base station, complicating the tracking of fast-moving objects, and other challenges [1]-[2]. While many of these issues have already been addressed over the past decade thanks to numerous developments by both the academic and industrial communities, the cost of deploying and maintaining the operation of such high-frequency systems remains very high compared to that of the current wireless infrastructure. Furthermore, all these systems are exclusively half-duplex, employing either frequency or time division diplexing to achieve bi-directional communication, therefore limiting the maximum transmission rate to only half of the network capacity. To overcome these problems, full-duplex communication has been being investigated recently [3]-[11]. In such a system, both the transmitter (TX) and the receiver (RX) operate simultaneously on the same frequency (see Fig. 1(a)), which, in principle, doubles the spectral efficiency, or equivalently, reduces the operational cost by halving the required resources. Furthermore, full-duplex radios would provide a solution to many problems at the network layer level such as hidden terminals, high end-to-end latency, fairness and congestion. The key challenge in full-duplexing, however, is to maintain sufficient isolation between the TX and the RX nodes of each transceiver in order to prohibit the strong TX signal from leaking into the RX path thus reducing the overall signal-to-noise ratio (SNR), and consequently, the throughput. More importantly, if such leakage is not sufficiently suppressed as early as possible in the RF chain, i.e., close to the antenna interface, it may saturate the RX frontend modules thus blocking the detection of any RX signal altogether. Such TX-to-RX isolation, commonly referred to in the literature as self-interference cancellation (SIC), is very difficult to achieve under the requirements dictated by commercial standards. For example, WiFi signals are transmitted at +20 dBm average power and the noise floor is around –90 dBm, hence SIC is required to be as high as 110 dB. For many years, attaining this level of SIC was impossible, hence full-duplex radios were presumed irrelevant in practice. Recently, several works challenged this long-held assumption and demonstrated that full-duplexing can, in fact, be achieved by using a combination of radio-frequency (RF) [5]-[7], mixed-signal [8]-[9], and digital techniques [10]-[11], while co-ordinating the cancellation in all these domains. The basic idea in both digital and mixed-signal approaches is to subtract the “known” TX signal from the RX node. But since the strength contrast between these two signals can in general be billions or trillions of magnitude, the subtraction must be performed extremely accurately, otherwise it may end up adding more self-interference instead of reducing it. More importantly, it is actually the baseband TX signal that is already known, but once it is up-converted to the carrier frequency and gone through the noisy non-linear RF chain, it undergoes frequency, phase, and amplitude distortions, which makes the estimation of its echo into the receiver even harder. Because of these issues, RF cancellation right at the antenna interface is absolutely necessary, leveraging digital and mixed-signal techniques as complementary approaches to eliminate any residual interference and to maintain the total required SIC.

RF cancellation can be classified into three categories: (i) antenna cancellation [10]-[11], (ii) electrical-balance duplexers [12]-[13], and (iii) circulators [14]-[60]. Antenna cancellation requires at least two antennas and is sensitive to their placement, thus making full-duplex less attractive compared to conventional MIMO systems, which can also double the throughput using multiple antennas but with less complexity. Electrical-balance duplexers (EBDs), on the other hand, are theoretically limited to 3 dB insertion loss (>4 dB in practice), i.e., half of the signal power is wasted twice, once in transmission and another in reception, hence the communication link incurs an aggregated loss of at least 6 dB, solely because of the EBDs. Obviously, this nullifies the main argument of full-duplexing and makes it not worthy finding solutions to all other accompanied hurdles. Quite interestingly, all these problems can be overcome by using a circulator, a three-port non-reciprocal component which routes the signal from one port to another in a cyclic-rotating fashion. Not only this allows the TX and RX nodes of each transceiver to share a single antenna as shown in Fig. 1(b), but the incremental insertion loss can also approach zero. Therefore, circulators are ideal elements to maintain the first 20~30 dB of the total required SIC in a full-duplex system which significantly relaxes the design of the following layers of isolation based on mixed-signal or digital techniques. The challenge in this case, however, is that circulation is essentially a non-reciprocal phenomenon which requires breaking time-reversal symmetry, a task that is not easy to accompolish efficiently, as we explain in the next section.

1.2 NON-RECIPROCITY

Time-reversal symmetry is a fundamental property of many physical and engineering systems, which implies that the laws governing such systems are invariant if the evolution of time is reversed. Breaking this symmetry is essential to realize non-reciprocal components such as circulators. In general, this can be achieved by using: (i) magnetic-biased gyrotropic materials [14]-[19], (ii) active devices [20]-[24], (iii) non-linear elements [25]-[27], or (iv) time-varying circuits [28]-[60]. For decades, magnetic biasing of rare-earth ferrite cavities was the only successful approach that led to high-performance non-reciprocal components, but they were also bulky and expensive, thus limited in use to a handful of military applications. To increase their ubiquity, magnetless implementations based on active or non-linear devices have been pursued, but despite significant research over many years, they continued to suffer from a fundamentally poor noise figure, limited power handling and small dynamic range, thus limiting their potential applications even more severly than magnetic-biased components.

Recently, it was shown that linear periodically time-varying (LPTV) circuits can overcome all these limitations and achieve high-performance non-reciprocity at low-cost and small-size, simultaneously [28]-[60]. In this regard, [28] presented the idea of parametrically modulating a transmission line (TL) by loading it with varactors and injecting a modulation signal at one port. Such a line allows signal propagation in one direction (the direction opposite to propagation of the modulation signal) as a conventional TL, while in the opposite direction it mixes the injected modulation with the RF signal, upconverting the latter to a different frequency. Such an approach necessitates the TL length to be larger than the wavelength and, more importantly, it requires the use of a diplexer to isolate the two counter-propagating RF signals in the frequency spectrum, thus making it not suitable for integration and less attractive when compared to high performance magnetic-biased circulators.

Ref. [29] relied on staggered commutation of *N*-path filters to realize a highly miniaturized gyrator, which when embedded in a loop of reciprocal phase shifters yields the operation of a circulator. This was the first CMOS demonstration of this concept and it was followed by other contributions enhancing the performance of many metrics [30]-[32]. Specifically, [31] proposed a gyrator based on modulating the conductivity of a transmission line, thus leading to a circulator with much wider isolation bandwidth and allowing to reduce the modulation frequency to one-third of the fundamental harmonic. A state-of-the-art implementation of this concept was presented in [32]. Similarly, [33] presented an ultra-wideband circulator operating from 200 KHz to 200 MHz using sequentially switched co-axial cables. A miniaturized implementation of the same concept was presented in [34] using a 0.2 μm GaN HEMT technology. One major challenge with [29]-[34], however, is the inherent *asymmetry* of the structures therein, which increases their sensitivity to inevitable random variations in practical systems. For instance, clock jitter and synchronization errors produced by an actual phase-locked loop (PLL) circuitry can degrade the overall isolation and the receive path noise figure compared to their values under ideal conditions. A digitally modulated RF signal with a finite bandwidth and a high peak-to-average power can cause similar problems, especially when both the transmit (TX) and the receive (RX) signals are simultaneously fed to the circulator, as would be the case in real-life applications. Also, impedance variation at any of the circulator’s ports, especially at the antenna (ANT) terminal, can be challenging to tackle in real time and may require complicated mixed-signal techniques that would impose a restriction on the maximum power handling.

In order to overcome these crucial problems, a cyclic-symmetric implementation that mimics the operation of magnetic-biased devices and maintains the rotational symmetry of ferrite cavities is highly desirable. Towards this goal, [35] presented the idea of spatiotemporal modulation angular-momentum (STM-AM) biasing, based on a loop of three resonators modulated in time with a particular phase pattern. Nevertheless, all implementations of such concept at any frequency range [35], [36], [52], failed in showing any promising results for the metrics they investigated such as insertion loss and matching, with many other metrics never investigated altogether, including bandwidth, power handling, linearity, spurious emission, noise figure, size, power consumption, and transmission phase dispersion. This, in turn, casted a lot of doubt on whether this approach can provide any advantage compared to others and was therefore presumed irrelevant in practice. In this dissertation, we challenge and falsify this assumption by refining the STM-AM concept and inventing several new circuits which we validate through rigorous analysis, simulations, and measurements, showing unprecedented performance nearly in all metrics compared to previous works.

This dissertation is organized as follows. In Chapter 2, we investigate the physical principles behind breaking reciprocity in a cyclic-symmetric circulator and develop four single-ended circuits that provide this functionality without magnets. In Chapter 3, we focus on one of these circuits which results in the first Watt-level magnetless circulator ever presented [37]. In Chapter 4, we develop the differential architectures of these circuits, which improve the performance of all metrics considerably, particularly insertion loss and noise figure [38]. In Chapter 5, we use the differential circuits as unit elements to realize the so-called *N*-way circulators, which suppress the spurious emission below appropriate levels dictated by spectral mask commercial standards and increase the overall power handling significantly [39]. In Chapter 6, we introduce a bandwidth extension technique based on combining any of the previous narrowband circuits with conventional bandpass filters [40]. In Chapter 7, we focus on chip-scale implementations of these circuits to reduce the overall cost and size [41]. In Chapter 8, we explore the use of MEMS resonators to decrease the total inductance needed in all previous designs, thus allowing further miniaturization [42]. Finally, we draw our conclusions and provide an outlook on future directions in Chapter 9.

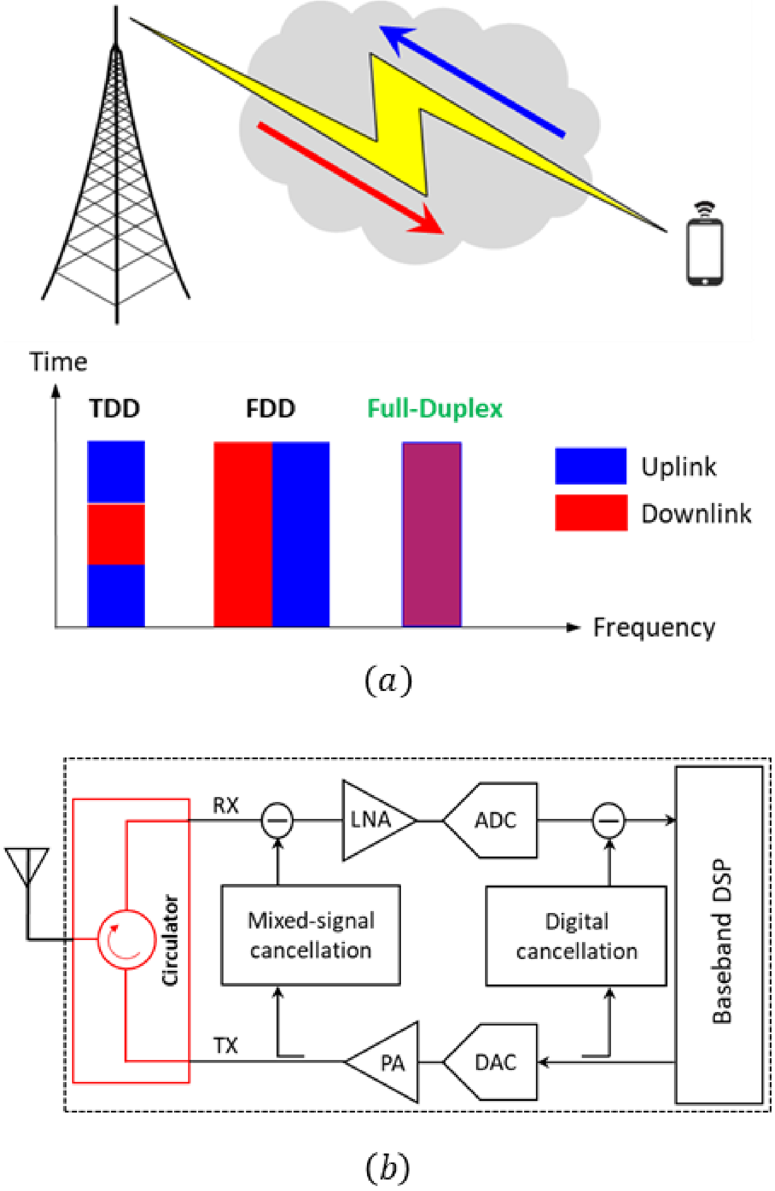

Figure 1: (a) Full-duplex versus currently deployed time-division duplex (TDD) and frequency-division duplex (FDD) systems. (b) Circulator in a full-duplex transceiver.

Chapter 2: Spatiotemporal Modulation Angular-Momentum Biasing

In this chapter, we explain the physical principles behind breaking reciprocity in a cyclic-symmetric circulator and discuss the main idea of how linear-time varying circuits are tantamount to magnetic-biased ferrite cavities.

2.1 THEORY

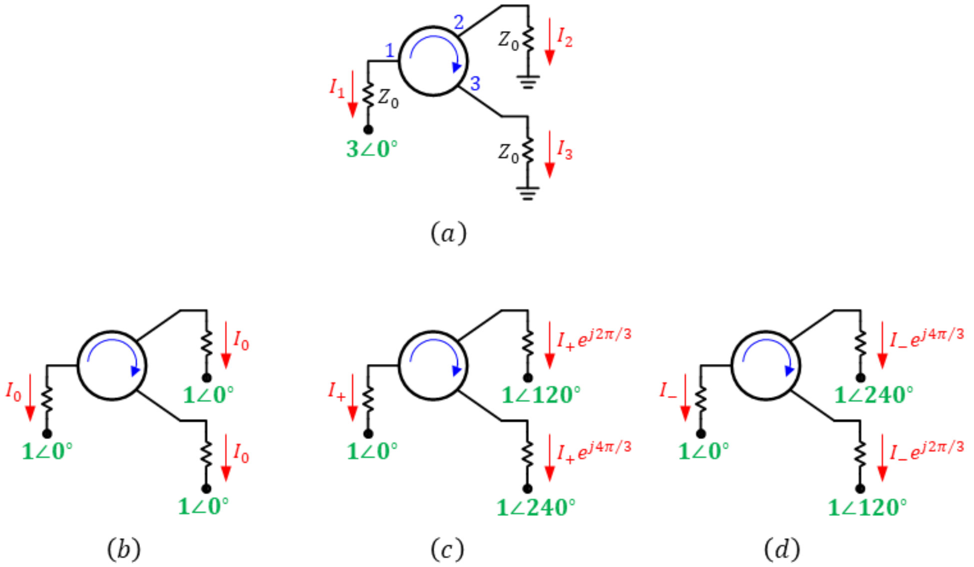

Figure 2: (a) Harmonic excitation at port 1 decomposed into a weighted summation of three components: (b) In-phase mode. (c) Clockwise mode. (d) Counter clockwise mode.

By definition, the *S*-parameters of any cyclic-symmetric circulator can be written in the following form

$$\overline{\overline{S}}(\omega)=\begin{bmatrix} S_{11} & S_{31} & S_{21} \\ S_{21} & S_{11} & S_{31} \\ S_{31} & S_{21} & S_{11} \end{bmatrix}, \tag{2.1}$$

where $\mathrm{RL} = -20\log_{10}\left(|S_{11}|\right)$ is the circulator's return loss, $\mathrm{IL} = -20\log_{10}\left(|S_{21}|\right)$ is the insertion loss, and $\mathrm{IX} = -20\log_{10}\left(|S_{31}|\right)$ is the isolation. Notice that in the ideal case, $S_{11} = S_{31} = 0$ and $S_{21} = 1$, assuming transmission in the following order $1 \rightarrow 2 \rightarrow 3$. These parameters are in general frequency dispersive, calculated with respect to the port impedance Z_0, and optimized to maintain a certain level of IL and IX, typically 3 dB and 20 dB, respectively, over a finite bandwidth (BW), which is centered around a particular design frequency, say f_0. The eigenvalues of this matrix can be calculated using $\left\| \bar{\bar{S}} - \lambda \bar{\bar{U}} \right\| = 0$, where $\bar{\bar{U}}$ is the unitary matrix, which yields

$$\lambda_c = S_{11} + S_{21} + S_{31} \tag{2.2}$$

$$\lambda_+ = S_{11} + e^{-j2\pi/3} S_{21} + e^{+j2\pi/3} S_{31} \tag{2.3}$$

$$\lambda_- = S_{11} + e^{+j2\pi/3} S_{21} + e^{-j2\pi/3} S_{31} \,. \tag{2.4}$$

The eigenvectors associated with (2.2)-(2.4) are also given by

$$\bar{V}_0 = \left[1,1,1\right]^{\mathrm{T}} \tag{2.5}$$

$$\bar{V}_+ = \left[1, e^{+j2\pi/3}, e^{-j2\pi/3}\right]^{\mathrm{T}} \tag{2.6}$$

$$\bar{V}_- = \left[1, e^{-j2\pi/3}, e^{+j2\pi/3}\right]^{\mathrm{T}} \,. \tag{2.7}$$

A harmonic excitation at any of the circulator's ports can be written as a summation of these eigenvectors. For instance, consider the excitation of port 1 as shown in Fig. 2(a) using a voltage source with an amplitude $3\angle 0^\circ$ and a matched source impedance Z_0, at an arbitrary frequency f, while terminating the other two ports with matched loads. This circuit can be decomposed using superposition into three sub-circuits, as shown in Fig. 2(b)-(d) (notice that $\sum_{n=1}^{3} e^{j(n-1)2\pi/3}=0$). In Fig. 2(b), the applied voltage sources are identical in both magnitude and phase, which is mathematically represented by the eigenvector $\bar{V}_0$. On the other hand, the voltage sources in Fig. 2(c) and Fig. 2(d) have the same magnitude but their phases increase by 120 deg either clockwise or counter-clockwise, which are also mathematically represented by the eigenvectors $\bar{V}_+$ and $\bar{V}_-$, respectively. Because of their distinctive phase pattern, we refer to these eigenvectors $\bar{V}_0$, $\bar{V}_+$, and $\bar{V}_-$ as the in-phase (0), clockwise (+), and counter clockwise (–) modes, respectively. The generated currents at all ports can also be written as a weighted summation of these modes, i.e.,

$$I_n = I_0 + I_+ e^{+j(n-1)2\pi/3} + I_- e^{-j(n-1)2\pi/3}, \tag{2.8}$$

where *n* is the port index, and the unknown weights I_0, I_+, and I_- rely on the specific implementation of the circulator itself. If we assume that this implementation guarantees that: (i) the in-phase current I_0 is zero and (ii) the rotating modes $I_\pm$ have the same amplitude but opposite phases, i.e., $I_\pm = I_g e^{\pm j\alpha}$, then (2.8) simplifies to

$$I_n = 2I_g \cos\left[(n-1)\frac{2\pi}{3}+\alpha\right]. \tag{2.9}$$

In the next sections, we explain how these two assumptions are satisfied in both magnetic and STM-AM circulators. Also, the phase α can be designed to be 30 deg at the center frequency f_0, which when substituted in (2.9) results in $I_3 = 0$ and $I_1 = -I_2 = \sqrt{3}I_g$, thus isolating port 3 from excitations at port 1 and transmitting the input power exclusively to port 2. Similarly, impinging signals on port 2 or port 3 would be routed exclusively to port 3 and port 1, respectively. As the input frequency deviates from f_0, however, α becomes different, thus reducing IX and increasing IL, which results in the typical dispersive *S*-parameters of circulators. It is worth mentioning that (2.9) neglects the impact of finite losses, which, if taken into account, will force the magnitudes of the rotating modes $I_\pm$, and consequently, the port currents $I_{1,2}$ to be slightly different, hence IL becomes finite. Interestingly, IX is not be impacted by these losses as long as the in-phase mode remains not excited. These remarks will become clearer in the next chapters when a rigorous small-signal analysis is presented. Nevertheless, the previous description, as simplistic as it is, is extremely valuable to begin with before delving into the details of a lengthy mathematical description so that the reader can gain an insight into the physical principles behind breaking reciprocity, either in magnetic or magnetless circulators.

2.2 MAGNETIC CIRCULATORS

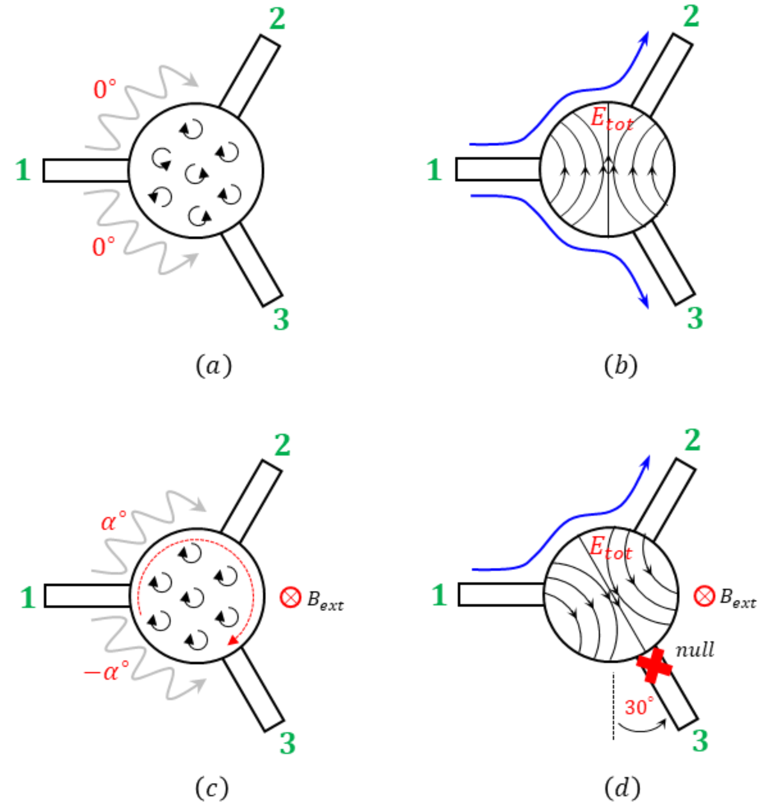

Figure 3: Magnetic circulator. (a) Magnetic dipole moments without bias. (b) Total electric field distribution without bias. (c) Magnetic dipole moments with bias. (d) Total electric field distribution with bias.

We see from the discussion in Sec. 2.1 that the underlying physical principles of cyclic-symmetric circulators are: (i) to ensure the in-phase mode is zero and (ii) to provide a preferred sense of precession for the counter-rotating modes that alters only their phases but not their amplitudes. In magnetic circulators, this is achieved by applying a magnetic bias to a ferrite cavity, which is symmetrically attached to three ports at 120° intervals, as shown in Fig. 3. Due to charge conservation, or equivalently Kirchhoff's current law (KCL), the in-phase mode current must be zero, otherwise charges will continue to accumulate boundlessly inside the cavity, hence the total electric field can be decomposed into a pair of rotating modes with azimuthal dependence $e^{\pm j\varphi}$. Without external bias, the magnetic dipole moments of the spinning electrons inside the ferrite disk are randomly oriented [see Fig. 3(a)] and the counter-rotating modes have the same resonant frequency. As a result, an incident wave at one port, say port 1, excites the counter-rotating modes with the same amplitude and phase, leading to a symmetrical field distribution with respect to the input port. For example, Fig. 3(b) shows the total field distribution for a driving frequency close to the resonance of the cavity. Due to the symmetry of the field distribution and the symmetry of the output ports with respect to the input one, the output signals at ports 2 and 3 are identical, showing that the unbiased junction operates as a symmetrical three-port bandpass filter. When a static magnetic bias is applied, however, along the axis of the ferrite cavity, the spinning electrons' dipole moments align in the same direction, as shown in Fig 1(c), which provides a preferred sense of precision for the counter rotating modes. In this case, the mode that propagates in the same direction of the precession will exhibit a different propagation velocity and, consequently, a different resonant frequency than the mode that propagates in the opposite direction, showing that the degeneracy of the rotating modes is lifted by the external bias. If the magnetic bias is also uniformly distributed across the cavity's cross section, then the strength of the rotating modes remains identical. Therefore, an incident wave at any port in the middle of the resonant frequencies of the rotating modes will excite the them with the same amplitude but with opposite phases $\pm\alpha$, resulting in a rotated electric field pattern, as illustrated in Fig. 3(d). For $\alpha = 30^\circ$, the rotated field pattern has a zero at port 3, resulting in zero transmission at this port, as shown in Fig. 3(d), and transmission of all the input power, assuming negligible losses, from port 1 to port 2. Similarly, for excitation at port 2 or 3, input power is exclusively transmitted to port 3 and 1, respectively.

2.3 MAGNETLESS CIRCULATORS

In Sec. 2.2, it was shown that magnetic circulators consist of a three-port resonant cavity, designed to ensure that a non-zero in-phase mode would violate KCL, and a preferred sense of precession is provided uniformly for the rotating modes such that they are excited with the same amplitude but with opposite phases. In light of these remarks, the STM-AM circulators can now be developed as follows. First, the resonant ferrite cavity is replaced by three series or parallel *LC* tanks connected in a loop or to a central node, which results in four possible combinations, namely, bandpass/wye, bandstop/delta, bandstop/wye, and bandpass/delta, as shown in Fig. 4. These circuits are essentially single-ended implementations of STM-AM circulators, as will become more clear in the next chapters, and they guarantee that the in-phase mode current is zero because otherwise it would violate KCL. A uniform preferred sense of precession is also provided for the rotating currents by modulating the instantaneous natural oscillation frequencies of the *LC* tanks, i.e., $\omega_n = 1/\sqrt{LC_n}$, through variable capacitors (varcaps) as follows

$$C_n = C_0 + \Delta C \cos\left(\omega_m t + \left(n-1\right) 2\pi/3\right), \tag{2.10}$$

where C_0 is the static capacitance and ΔC and ω_m are the modulation depth and frequency, respectively. Notice that the phases of the modulation signals increase by 120 deg in the clockwise direction similar to I_+ and, necessarily, opposite to I_-, however, the modulation depth and frequency are the same for all tanks. Therefore, only the phases of $I_\pm$ become different but their amplitudes remain identical. We refer to this modulation scheme as spatiotemporal modulation angular-momentum (STM-AM) biasing, since it involves phase variation in space (φ direction) and in time (*t*), which synthesizes an effective angular momentum that mimics the effect of the aligned dipole moments in magnetic-biased ferrite cavities, i.e., both provide uniformly a preferred sense of precession for the rotating modes

$I_{\pm}$. Therefore, the circuits of Fig. 4 are all expected to yield the functionality of a circulator. It is also worth mentioning that without modulation, both the bandpass/wye and the bandpass/delta topologies operate as a symmetrical three-port bandpass filter, similar to magnetic circulators when no bias is applied. In contrast, the bandstop/delta and the bandstop/wye topologies do not, in fact, allow any transmission between the ports when the modulation is turned OFF. While it does seem counter intuitive, the previous analysis still applies and both circuits do work as magnetless circulators. More specifically, the STM-AM bias lifts the degeneracy of the rotating modes at the resonance frequency $\omega_0 = 1/\sqrt{L_0 C_0}$, therefore when the modulation is applied, the circuit actually oscillates at $\omega_0 \pm \omega_m$ rather than ω_0. In between these two frequencies, the skirts of the resonances do allow transmission and they exhibit opposite phases. Therefore, if an input signal is incident at one port at the middle of these two frequencies, i.e., at ω_0, it will excite the two resonances with equal magnitude and opposite phase, thus allowing to achieve isolation at one port and perfect transmission to another. This is consistent with the previous description based on providing a preferred sense of precession. In the next chapter, we explain this even further by analyzing the bandstop/delta topology rigorously to derive closed-form expression for the *S*-parameters when the STM-AM bias is applied. We also validate the analysis with detailed simulated and measured results showing remarkable performance in several metrics, particularly, isolation and power handling.

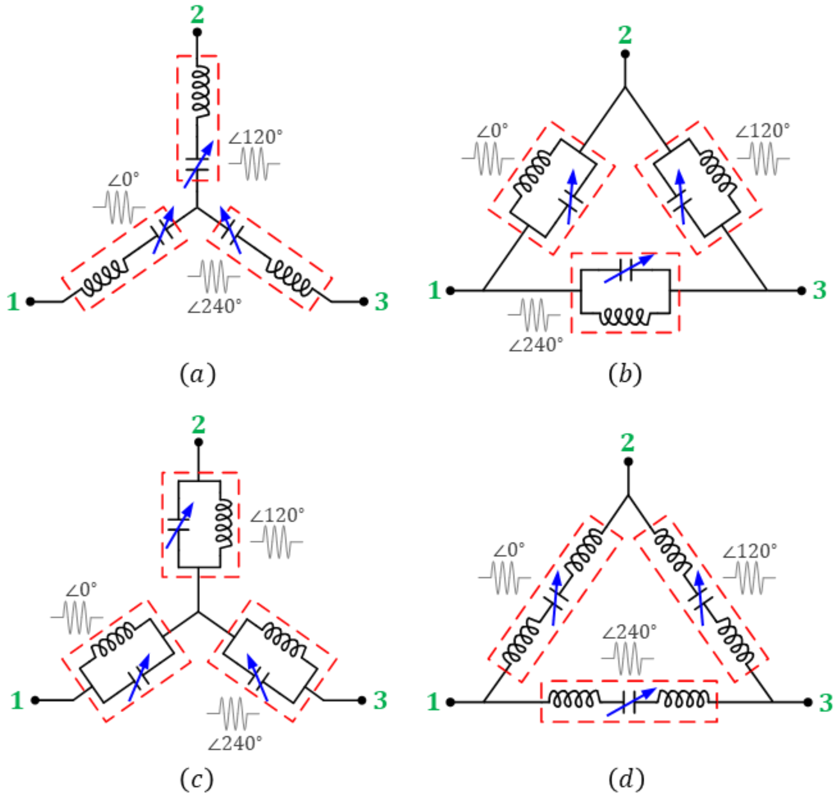

Figure 4: Single-ended STM-AM circulators: (a) Bandpass/wye. (b) Bandstop/delta. (c) Bandstop/wye. (d) Bandpass/delta.

Chapter 3: Single-Ended STM-AM Circulators[1]

In this chapter, we provide a rigorous analysis, simulated, and measured results for the bandstop/delta topology, as an example to validate the functionality of the single-ended STM-AM circulators developed in Chapter 2.

3.1 ANALYSIS

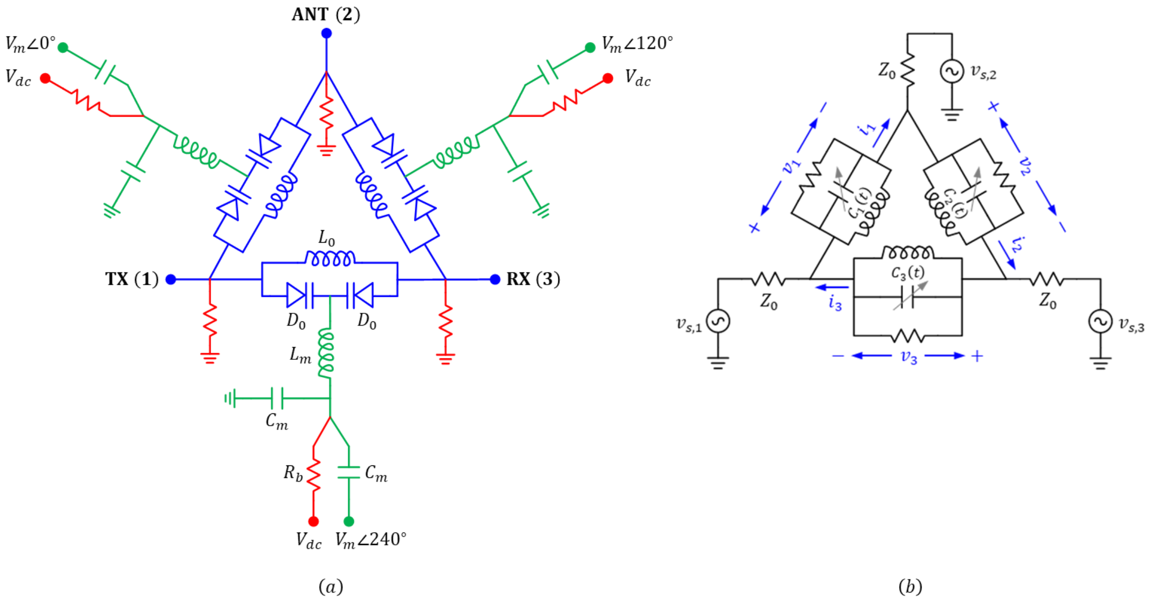

Figure 5: Bandstop/delta topology. (a) Complete schematic. (b) Small-signal model at the input frequency of the TX and RX signals.

Fig. 5(a) shows the complete schematic of the bandstop/delta topology, which consists of three identical parallel *LC* tanks connected in a loop, the terminals of which are connected to the TX, ANT, and RX ports, which all have an impedance Z_0 (typically 50 Ohm). As explained in Chapter 2, an effective STM-AM bias that makes this circuit work

---

[1] The content of this chapter is published in [37].

as a circulator is synthesized by modulating the oscillation frequencies of the tanks $f_n = 1/2\pi\sqrt{L_0 C_n}$, where *n* is the tank index, L_0 and C_n are the inductance and capacitance of the *n*-th tank, respectively, through varacaps [see (2.1)]. In Fig. 5(a), the varacaps are implemented via pairs of common-cathode varactors D_0 and the modulation signals with frequency f_m, amplitude V_m, and phase $(n-1)2\pi/3$, are injected to the common-cathode node through matching networks (L_m and C_m). These networks serve as bandstop filters for the TX and RX signals, thus prohibiting their leakage into the modulation ports. Moreover, large resistors R_b are used to combine the DC bias V_{dc} with the modulation signals and to DC ground the varactor's anode as well. In general, three additional filters may be needed at the RF ports to prohibit the modulation signals from leaking into them. However, thanks to the 120 deg phase shifts of the modulation signals and the rotational symmetry of the delta topology, the ports exhibit a virtual ground at f_m, which alleviates the necessity of using these filters.

At the input frequency of the TX and RX signals, the complete schematic of Fig. 5(a) simplifies as shown in Fig. 5(b), which is essentially the same as Fig. 4(b) after incorporating an additional resistance R_0 in parallel with each *LC* tank. This resistance models the finite losses of the varactors and inductors and it results in a total unloaded quality factor $Q_0 = R_0 / \omega_0 L_0$. For simplicity, we assume R_0, and consequently Q_0, are both non-dispersive, which is a reasonable approximation over narrow bandwidths, as is the case in this circuit which relies on first-order *LC* resonators. It is also worth highlighting that electronic varactors based on PN junctions are generally non-linear, i.e.,

$$C_n = C_0 + \sum_{k=1}^{\infty} a_k v_n^k , \tag{3.1}$$

where C_0 is the effective static capacitance of each common-cathode varactors' pair set by the DC bias V_{dc}, a_k are the coefficients of a polynomial that models the non-linear CV characteristics around the quiescent point, and

$$v_n = v_n^{rf} + v_n^{\mathrm{mod}}, \tag{3.2}$$

is the total AC voltage across the *n*-th tank. Since the *S*-parameters are, by definition, calculated under the small-signal assumption $v_n^{rf} << v_n^{\mathrm{mod}}$, then (3.1) can be simplified to

$$C_n = C_0 + a_1 v_n^{mod} + a_2 (v_n^{mod})^2 + \ldots. \tag{3.3}$$

If we further assume that the modulation index is relatively weak, i.e., $\Delta C / C_0 < 0.5$ as is the case with any physical varactor, then we can keep the terms up to first order and (3.3) further simplifies to

$$C_n = C_0 + a_1 V_m \cos\left(\omega_m t + \varphi_n\right), \tag{3.4}$$

which is exactly the same as (2.1) after substituting $\varphi_n = \left(n-1\right) 2\pi/3$ and $\Delta C = a_1 V_m$. Since (3.4) already embeds the DC and modulation voltages into the definition of C_n, then we can interpret the tank voltages in Fig. 5(b) as the RF component solely, i.e., $v_n = v_n^{rf}$, and omit the superscript *rf* from this point onward. Applying Kirchhoff's current law (KCL) to the *n*-th tank in Fig. 5(b), we get

$$v_n = L_0 i'_{L,n} \tag{3.5}$$

$$i_{L,n} = i_n - \frac{v_n}{R_0} - C_n v'_n, \tag{3.6}$$

where $' = \frac{d}{dt}$, $i_{L,n}$ is the current in the inductor of the *n*-th tank, i_n is the total current in the *n*-th branch (see Fig. 5(b)). Taking the derivative of (3.6) and substituting it into (3.5), we get

$$i_n' = C_n v_n'' + \left(\frac{1}{R_0} + C_n' \right) v_n' + \frac{1}{L_0} v_n , \tag{3.7}$$

where $'' = \frac{d^2}{dt^2}$. Substituting (3.4) into (3.7), we get

$$i_n' = \left[C_0 + \Delta C \cos\left(\omega_m t + \varphi_n\right) \right] v_n'' + \left[\frac{1}{R_0} - \Delta C \omega_m \sin\left(\omega_m t + \varphi_n\right) \right] v_n' + \frac{1}{L_0} v_n . \tag{3.8}$$

Equation (3.8) can be rewritten in a matrix form as follows

$$\left(C_0 \overline{\overline{U}} + \Delta C \overline{\overline{C_c}} \right) \overline{v}'' + \left(\frac{1}{R_0} \overline{\overline{U}} - \Delta C \omega_m \overline{\overline{C_s}} \right) \overline{v}' + \frac{1}{L_0} \overline{v} = \overline{i}' , \tag{3.9}$$

where $\overline{v} = \{v_1, v_2, v_3\}$ and $\overline{i} = \{i_1, i_2, i_3\}$ are the vectors of the tank voltages and currents, respectively, $\overline{\overline{U}}$ is the unitary matrix, and $\overline{\overline{C}}_c$ and $\overline{\overline{C}}_s$ are two matrices given by

$$\overline{\overline{C}}_c = \begin{bmatrix} \cos\left(\omega_m t\right) & 0 & 0 \\ 0 & \cos\left(\omega_m t + 2\pi/3\right) & 0 \\ 0 & 0 & \cos\left(\omega_m t + 4\pi/3\right) \end{bmatrix} \tag{3.10}$$

$$\overline{\overline{C}}_s = -\frac{1}{\omega_m} \overline{\overline{C}}_c' = \begin{bmatrix} \sin\left(\omega_m t\right) & 0 & 0 \\ 0 & \sin\left(\omega_m t + 2\pi/3\right) & 0 \\ 0 & 0 & \sin\left(\omega_m t + 4\pi/3\right) \end{bmatrix} . \tag{3.11}$$

The tank currents $\overline{i}$ can be related to the source sources $\overline{i}_s = \{i_{s,1}, i_{s,2}, i_{s,3}\}$ using KCL at the terminals of the delta loop, which results in

$$\overline{i}_s = -\overline{\overline{G}} \overline{i} , \tag{3.12}$$

where

$$\overline{\overline{G}} = \begin{bmatrix} +1 & -1 & 0 \\ 0 & +1 & -1 \\ -1 & 0 & +1 \end{bmatrix} . \tag{3.13}$$

Substituting (3.12) into (3.9) yields

$$\left(C_0\bar{\bar{G}}+\Delta C\bar{\bar{G}}\bar{\bar{C}}_c\right)\bar{v}''+\left(\frac{1}{R_0}\bar{\bar{G}}-\Delta C\omega_m\bar{\bar{G}}\bar{\bar{C}}_s\right)\bar{v}'+\frac{1}{L_0}\bar{\bar{G}}\bar{v}=-\bar{i}_s' \,. \tag{3.14}$$

Equation (3.14) is essentially a system of three second-order coupled differential equations that governs the single-ended bandstop/delta circulator. In order to solve such system of equations, three boundary conditions are needed. Obviously, these are determined by the port terminations. In the case under consideration, the ports are connected to three different voltage sources through identical impedances Z_0, as depicted in Fig. 5(b). Using KVL, this results in the following boundary equation

$$\bar{\bar{G}}\bar{i}_s=\frac{1}{Z_0}\bar{\bar{G}}\bar{v}_s+\frac{1}{Z_0}\left(\bar{\bar{G}}-\bar{\bar{U}}\right)\bar{v}\,, \tag{3.15}$$

which when substituted into (3.14) results in

$$\left(C_0\bar{\bar{J}}+\Delta C\bar{\bar{J}}\bar{\bar{C}}_c\right)\bar{v}''+\left(\frac{1}{R_0}\bar{\bar{J}}-\Delta C\omega_m\bar{\bar{J}}\bar{\bar{C}}_s-\frac{1}{Z_0}\left(\bar{\bar{U}}-\bar{\bar{G}}\right)\right)\bar{v}'+\frac{1}{L_0}\bar{\bar{J}}\bar{v}=-\frac{1}{Z_0}\bar{\bar{J}}\bar{v}_s'\,, \tag{3.16}$$

where $\bar{\bar{H}}$ is given by

$$\bar{\bar{J}}=\bar{\bar{G}}^2=\begin{bmatrix}1 & -2 & 1\\ 1 & 1 & -2\\ -2 & 1 & 1\end{bmatrix}. \tag{3.17}$$

As explained in Chapter 2, the voltage sources $\bar{v}_s$ can be expressed a superposition of three modal quantities, which would simplify the analysis since the in-phase mode excitation does not force any current flow into the circuit, thus reducing (3.16) into two, rather than three, coupled differential equations. As a matter of fact, this transformation can also be applied to the tank voltages $\bar{v}$ as follows

$$\bar{v} = \bar{\bar{T}}\,\hat{v}\,, \tag{3.18}$$

where $\hat{v} = \{v_0, v_+, v_-\}$ and the operator $\bar{\bar{T}}$ is given by

$$\bar{\bar{T}} = \begin{bmatrix} 1 & 1 & 1 \\ 1 & e^{j\alpha} & e^{-j\alpha} \\ 1 & e^{j2\alpha} & e^{-j2\alpha} \end{bmatrix}. \tag{3.19}$$

Substituting (3.18) into (3.16) yields

$$3Z_0C_0v_0'' + v_0' + \frac{3Z_0}{L_0}v_0 = 0 \tag{3.20}$$

$$\begin{gathered} 3Z_0C_0v_+'' + \frac{3}{2}Z_0\Delta Ce^{-j\omega_m t}v_-'' + \left(1+\frac{3Z_0}{R_0}\right)v_+' - \frac{j3}{2}Z_0\Delta C\omega_m e^{-j\omega_m t}v_-' + \frac{3Z_0}{L_0}v_+ \\ = \frac{1}{6}\left(3 - j\sqrt{3}\right)v_{s,1}' - \frac{1}{6}\left(3 + j\sqrt{3}\right)v_{s,2}' + \frac{j}{\sqrt{3}}v_{s,3}' \end{gathered} \tag{3.21}$$

$$\begin{gathered} 3Z_0C_0v_-'' + \frac{3}{2}Z_0\Delta Ce^{j\omega_m t}v_+'' + \left(1+\frac{3Z_0}{R_0}\right)v_-' + \frac{j3}{2}Z_0\Delta C\omega_m e^{j\omega_m t}v_+' + \frac{3Z_0}{L_0}v_- \\ \frac{1}{6}\left(3 + j\sqrt{3}\right)v_{s,1}' - \frac{1}{6}\left(3 - j\sqrt{3}\right)v_{s,2}' - \frac{j}{\sqrt{3}}v_{s,3}' \end{gathered}. \tag{3.22}$$

As expected, (3.20) has the trivial solution $v_0 = 0$. On the other hand, (3.21) and (3.22) can be further simplified by substituting $v_{s,2} = v_{s,3} = 0$, i.e., only port 1 is excited, since a general $\bar{v}_s$ can be constructed using a linear superposition of individual port excitations, and, thanks to the circuit's symmetry, excitations from ports 2 and 3 can be inferred from excitation at port 1. Notice that this is how small-signal *S*-parameters are also calculated, i.e., one port is excited at a time while the other ports are terminated with matched loads. Moreover, the solution of (3.21) and (3.22) can be easily obtained in frequency rather than in time domain by applying Fourier transform, which yields

$$V_\pm(\omega) = \sum_{k=-1}^{1} H_k^\pm(\omega)V_{s,1}(\omega + k\omega_m)\,, \tag{3.23}$$

where $V_+(\omega)$ and $V_-(\omega)$ are the Fourier transforms of $v_+(t)$ and $v_-(t)$, respectively, $V_{s,1}(\omega)$ is the Fourier transform of $v_{s,1}(t)$,

$$H_0^{\pm}(\omega)=\frac{\frac{j\omega}{6}\left(3\mp j\sqrt{3}\right)}{D_{\pm}(\omega)}\left(\begin{array}{c}-3C_0Z_0\left(\omega\pm\omega_m\right)^2+\frac{3Z_0}{L_0}\\ +j\left(\omega\pm\omega_m\right)\left(1+\frac{3Z_0}{R_0}\right)\end{array}\right) \tag{3.24}$$

$$H_{-1}^{-}(\omega)=\frac{\frac{j}{4}\left(3-j\sqrt{3}\right)\Delta CZ_0\omega\left(\omega-\omega_m\right)^2}{D_-(\omega)} \tag{3.25}$$

$$H_1^{+}(\omega)=\frac{\frac{j}{4}\left(3+j\sqrt{3}\right)\Delta CZ_0\omega\left(\omega+\omega_m\right)^2}{D_+(\omega)}, \tag{3.26}$$

and $H_{-1}^{+}(\omega)=H_1^{-}(\omega)=0$. The denominator functions $D_{\pm}(\omega)$ are also given by

$$\begin{aligned}D_{\pm}(\omega)&=-\frac{9}{4}\Delta C^2Z_0^2\omega^2\left(\omega\pm\omega_m\right)^2\\&+\left(-3C_0Z_0\omega^2+\frac{3Z_0}{L}+j\omega\left(1+\frac{3Z_0}{R_0}\right)\right)\\&\times\left(-3C_0Z_0\left(\omega\pm\omega_m\right)^2+\frac{3Z_0}{L_0}+j\left(\omega\pm\omega_m\right)\left(1+\frac{3Z_0}{R_0}\right)\right)\end{aligned}. \tag{3.27}$$

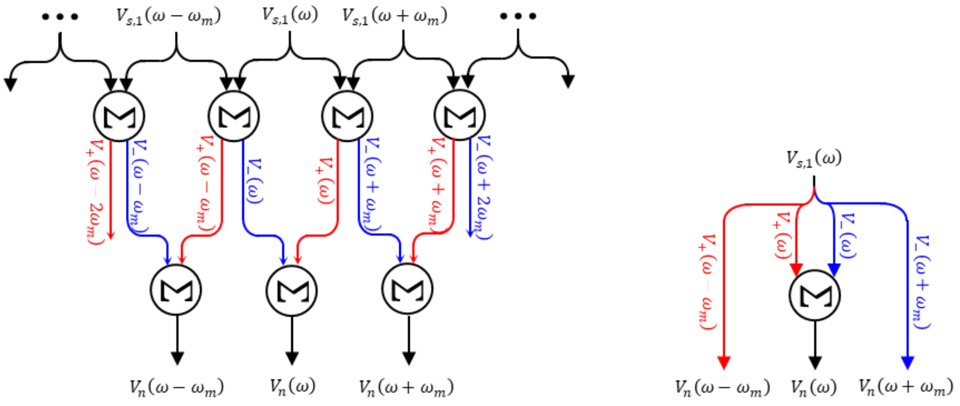

(a) (b)

Figure 6: Frequency mixing map. (a) BW>2f_m. (b) BW < 2f_m.

Equation (3.23) shows that the counter-rotating voltages $V_\pm$ at any frequency ω depend, in general, on the source voltages at three different frequencies, i.e., ω, $\omega+\omega_m$, and $\omega-\omega_m$, as a result of the modulation. A graphical representation of the frequency mixing mechanism in this case is provided in Fig. 6(a). If the BW of the input signals is smaller than $2f_m$, the mixing map simplifies as shown in Fig. 6(b) and closed-form expression for the modal amplitudes at ω, $\omega+\omega_m$, and $\omega-\omega_m$ can be found as follows

$$\frac{V_\pm(\omega)}{V_{s,1}(\omega)} = \frac{\frac{j\omega}{6}\left(3\mp j\sqrt{3}\right)}{D_\pm(\omega)}\begin{pmatrix} -3C_0Z_0\left(\omega\pm\omega_m\right)^2+\frac{3Z_0}{L_0} \\ +j\left(\omega\pm\omega_m\right)\left(1+\frac{3Z_0}{R_0}\right)\end{pmatrix} \tag{3.28}$$

$$\frac{V_\pm\left(\omega\mp\omega_m\right)}{V_{s,1}(\omega)} = \frac{\frac{j}{4}\left(3\pm j\sqrt{3}\right)\Delta C Z_0\left(\omega\mp\omega_m\right)\omega^2}{D_\mp(\omega)}, \tag{3.29}$$

and $V_\pm\left(\omega\pm\omega_m\right)=0$. The original tank voltages $\bar{V}=\{V_1,V_2,V_3\}$ can now be calculated using (3.18), while recognizing that $V_c=0$, which yields

$$V_n\left(\omega_k\right)=e^{j(n-1)2\pi/3}V_+\left(\omega_k\right)+e^{-j(n-1)2\pi/3}V_-\left(\omega_k\right), \tag{3.30}$$

where $\omega_k=\omega+k\omega_m$ and $k=-1,0,1$ is the harmonic index. The tank currents $I_n\left(\omega_k\right)$ can also be calculated by Fourier transforming (3.7), resulting in

$$I_n(\omega)=\left(\frac{1}{R_0}+j\omega C_0+\frac{1}{j\omega L_0}\right)V_n(\omega)+\frac{j}{2}\Delta C\begin{bmatrix} e^{j(n-1)\alpha}\left(\omega-\omega_m\right)V_n\left(\omega-\omega_m\right) \\ +e^{-j(n-1)\alpha}\left(\omega+\omega_m\right)V_n\left(\omega+\omega_m\right)\end{bmatrix} \tag{3.31}$$

$$I_n\left(\omega\pm\omega_m\right)=\frac{j}{2}\Delta C e^{\pm j(n-1)\alpha}\omega V_n(\omega)+\left(\frac{1}{R_0}+j\left(\omega\pm\omega_m\right)C_0+\frac{1}{j\left(\omega\pm\omega_m\right)L_0}\right)V_n\left(\omega\pm\omega_m\right). \tag{3.32}$$

Notice that the source currents $I_s\left(\omega_k\right)$ can also be found by substituting (3.31) and (3.32) into the Fourier transform of equation reference goes here, which is simply $\bar{I}_s(\omega)=-\bar{\bar{G}}\bar{I}(\omega)$. Finally, the harmonic *S*-parameters are, by definition, given by

$$S_{ji}\left(\omega_k,\omega\right)=\delta_{ji}\delta_{k0}-2\frac{Z_0 I_{s,j}\left(\omega_k\right)}{V_{s,i}\left(\omega\right)}\,, \tag{3.33}$$

where δ_{ji} is the Kronecker delta function, which is equal to 1 for $i=j$ and equal to zero otherwise. Notice that for $k=0$, (3.33) results in the conventional *S*-parameters defined for linear time-invariant (LTI) systems, which relate the input and output powers at the same frequency. For $k\neq 0$, however, (3.33) describes the amount of power transferred from the fundamental harmonic of the incident signal to the intermodulation products (IMPs) at all ports. From this point onward, the *S*-parameters will refer to the conventional ones, unless stated otherwise. The harmonic input impedances $Z_{in}\left(\omega_k,\omega\right)$ are identical at all ports due to symmetry, and they can be calculated as follows

$$Z_{in}\left(\omega_k,\omega\right)=\frac{V_{s,n}\left(\omega\right)}{I_{s,n}\left(\omega_k\right)}-Z_0\,. \tag{3.34}$$

Like for the *S*-parameters, $k=0$ yields the conventional input impedance, which relates voltages and currents having the same frequency. Yet, for $k\neq 0$, $Z_{in}\left(\omega_k,\omega\right)$ corresponds to a trans-impedance which relates the input voltage at ω to the excited current at ω_k. It is also worth mentioning that $Z_{in}\left(\omega_k,\omega\right)=Z_0\frac{1+S_{jj}\left(\omega_k,\omega\right)}{1-S_{jj}\left(\omega_k,\omega\right)}$ still holds for all k.

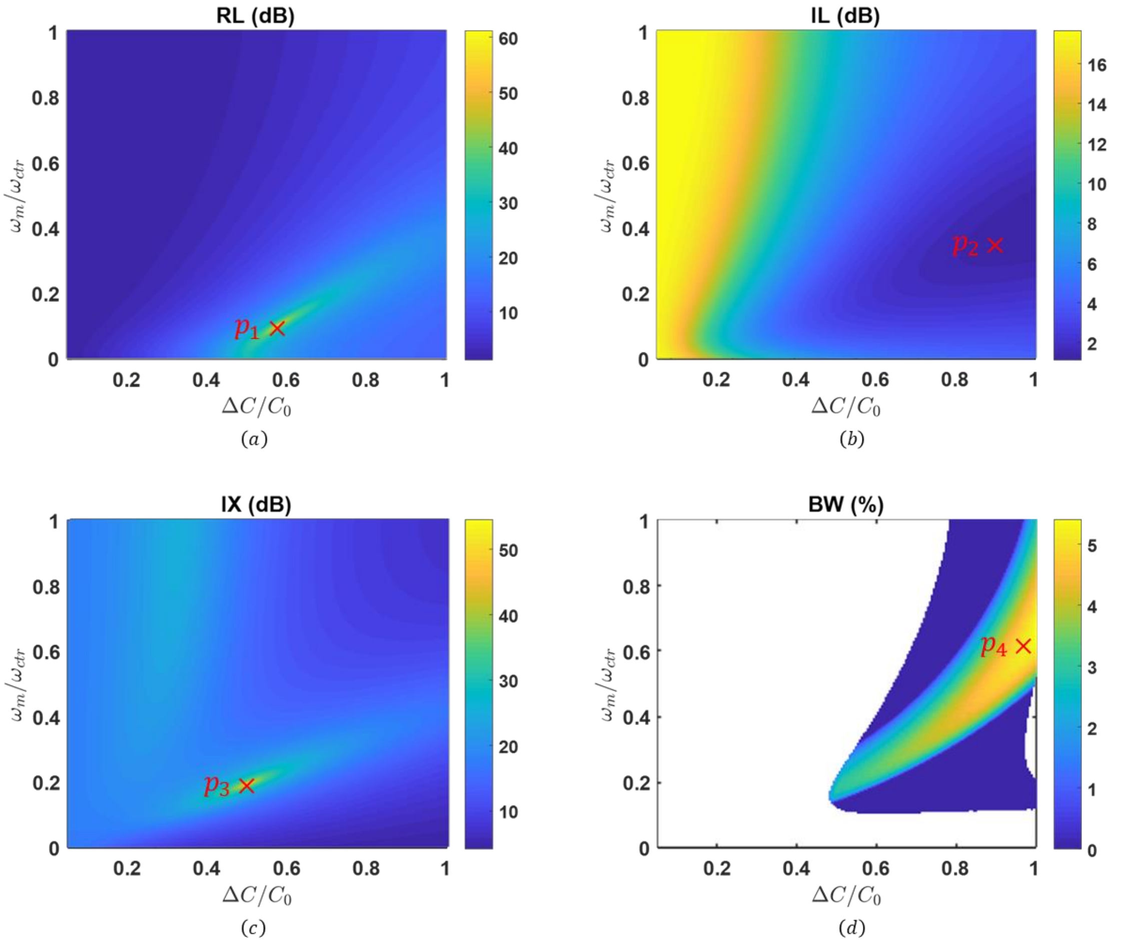

Figure 7: Analytical *S*-parameters at ω_{ctr} versus the normalized modulation parameters ω_m/ω_{ctr} and $\Delta C/C_0$. (a) RL. (b) IL. (c) IX. (d) BW.

Equation (3.33) gives the *S*-parameters as a function of the circuit elements L_0 and C_0 and the modulation parameters f_m and ΔC. These parameters should be chosen for operation around a desired center frequency f_{ctr} while satisfying certain specifications on IL, RL, IX, and BW. For example, for $f_{ctr} = 1$ GHz, $L_0 = 3.4$ nH, and $C_0 = 7.67$ pF, Fig. 7 shows the IL, RL, and IX at 1 GHz, and the fractional BW around the same frequency, all versus the normalized modulation parameters f_m/f_{ctr} and $\Delta C/C_0$. The optimal values of these metrics are also marked by the points p_1, p_2, p_3, and p_4. Notice that these points are not aligned, therefore one may need to trade off one or several of the desired specs. For instance, if we choose to maximize the IX at the center frequency, then the required modulation parameters are specified by point p_3, which are summarized in Table 1. Substituting these values into (3.33), the *S*-parameters can be calculated at all frequencies, as shown in Fig. 8(a). As expected, IX at 1 GHz is as large as 56 dB. Also, IL and RL at the same frequency are 2.9 dB and 10.8 dB, respectively, and the fractional BW is 2.7% (27 MHz). Fig. 8(b) also shows that the transmission phase is quite linear within the BW of interest, thus introducing minimal dispersion to the TX and RX signals and allowing the use of this circulator in any coherent or non-coherent communication system.

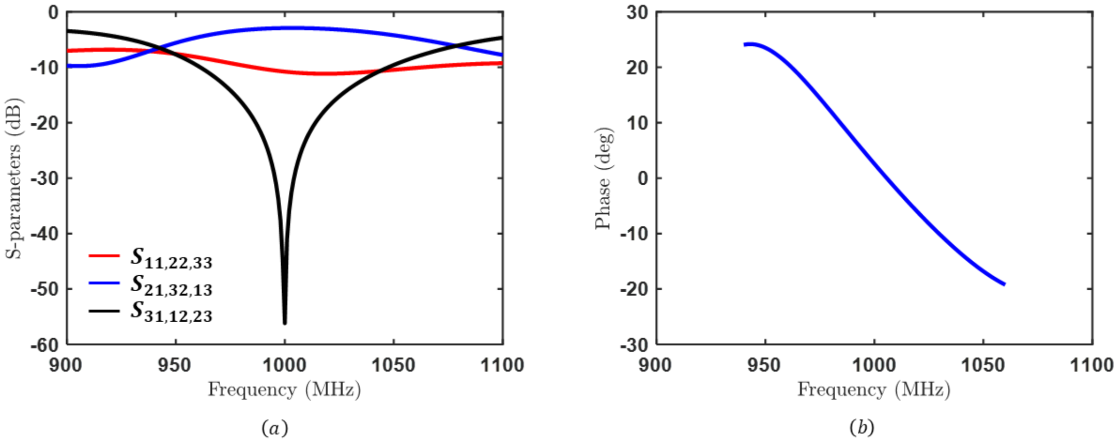

Figure 8: (a) Analytical *S*-parameters. (b) Analytical transmission phase.

Element\Value		Theo.		Sim.	Meas.
Main circuit	f_{ctr} (MHz)	1000		1000	1000
	f_m/f_{ctr} (%)	19		19	19
	L_0 (nH)	3.4	$Q_0 = 70$	3.3 (Coilcraft)	3.3 (Coilcraft)
	C_0 (pF)	7.67		BB439 (Infineon)	BB439 (Infineon)
	$\Delta C/C_0$ (%)	46			
Modulation network	V_m (Vpp)	N/R		7.24	10.8
	L_m (nH)	N/R		72 (Coilcraft)	72 (Coilcraft)
	C_m (pF)	N/R		24 (Coilcraft)	24 (Murata)
DC bias network	V_{dc} (Volt)	N/R		21.6	19.6
	R_b (KΩ)	N/R		100 (KOA)	100 (KOA)
	C_b (pF)	N/R		1000 (Murata)	1000 (Murata)

Table 1: Values of all design parameters used in obtaining the theoretical, simulated and measured results of the single-ended bandstop/delta STM-AM circulator.

Fig. 9 also shows the analytical spectrums at the ANT and RX ports for a monochromatic TX excitation with an input frequency f_{in} of 1 GHz and an input power P_{in} of 0 dBm. The second-order IMPs at $f_{in} \pm f_m$, are both –13 dBc, where dBc is a normalized unit describing the IMPs magnitude at all ports with respect to the incident TX tone. It is worth highlighting that these products are the result of time variation without any contribution from the inevitable non-linearities of the varactors, since the above analysis is based on linear small signals (see (3.1)-(3.4)). In reality, however, non-linearities not only make the IMPs at stronger, but they also lead to many other mixing spurs at and high-order harmonics at and , where *k* and *l* are integers and is the input frequency. In fact, if the input signal has a finite BW, as is the case in any real system, the situation becomes more complicated and the spurious emission becomes even worse. This issue will be investigated in detail through simulations and measurements in Sec. 3.2.2.

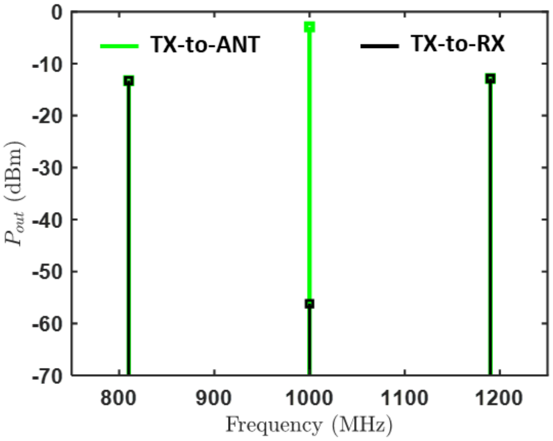

Figure 9: Analytical spectrums at the ANT and RX ports for a monochromatic TX excitation with an input frequency f_{in} of 1 GHz and an input power P_{in} of 0 dBm.

3.2 RESULTS

Based on the theoretical analysis presented in Sec. 3.1, a single-ended badnstop/delta STM-AM circulator operating at 1 GHz was designed in Keysight ADS. The performance was optimized through post-layout circuit/EM co-simulations by combining commercially available measured *S*-parameters for all lumped elements with the layout parasitics extracted by ADS Momentum full-wave analysis. The circuit was then fabricated and tested on a printed circuit board (PCB) using commercial off-the-shelf discrete components as listed in Table 1. Fig. 10 shows a photograph of the board and the circulator’s form factor is 13mm×11mm. The measured results were obtained using the experimental setups discussed in detail in Appendix A, and they are all in excellent agreement with simulations.

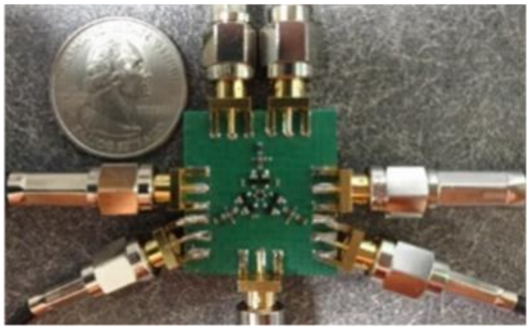

Figure 10: Photograph of the fabricated single-ended STM-AM circulator.

3.2.1 *S*-PARAMETERS

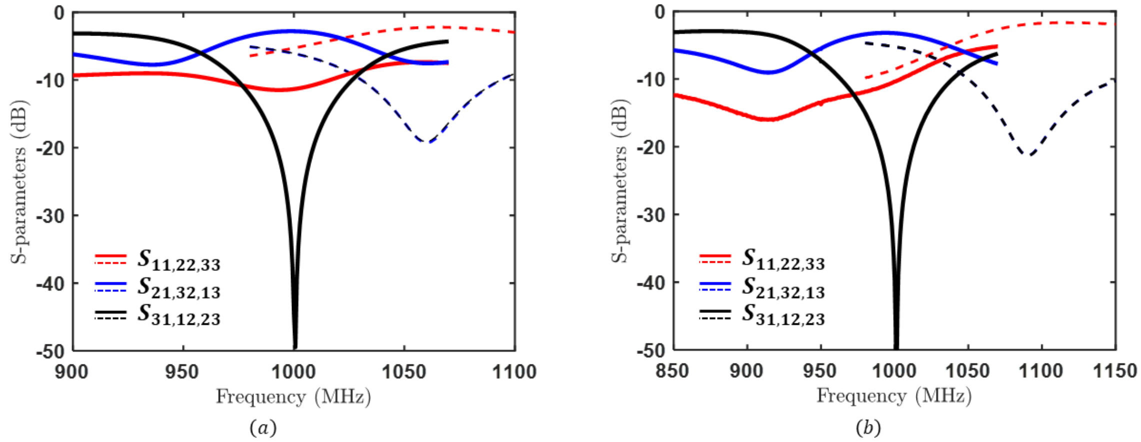

Figure 11: Comparison between the *S*-parameters with and without modulation. (a) Simulated. (b) Measured.

Fig. 11 shows the simulated and measured *S*-parameters with and without modulation. Without modulation, i.e., $V_m = 0$, the circuit is clearly reciprocal and exhibits a typical bandstop response. When the modulation is turned on, however, with $f_m = 190$ MHz and $V_m = 3.62$ V, the circuit yields the functionality of a circulator, as expected, and the center frequency is shifted down to 1 GHz. This shift of 60 MHz and 90 MHz observed in both simulations and measurements, respectively, is due to the varactors' even-order non-linearities as will be explained in Sec. 3.2.3. Also, the simulated IL, RL, and IX at 1 GHz are 2.8 dB, 11.34 dB, and 55 dB, respectively, and the simulated BW is 1.8% (18 MHz). Similarly, the measured IL, RL, and IX are 3.3 dB, 10.8, 55 dB, respectively, and the measured BW is 2.4% (24 MHz). We also notice that the measured RL is asymmetric with respect to the center frequency of 1 GHz, which is mainly due to the varactors' parasitics resulting in a self-resonance frequency (SRF) closer to 1 GHz than predicted by their spice model in simulations. It is worth stressing that this RL asymmetry should not be confused with the circulator's three-port cyclic-symmetry which is preserved, i.e., $S_{11} = S_{22} = S_{33}$, $S_{21} = S_{32} = S_{13}$, and $S_{31} = S_{12} = S_{23}$. The circuit can also be reconfigured for operation at different channels (different f_{ctr}) by simply changing the DC bias and adjusting the modulation voltage to account for the different slopes of the varactors' CV characteristics. For example, Fig. 12 shows the *S*-parameters for three different channels. The maximum tunability range is found to be 100 MHz (10% of f_{ctr}) in simulations and 60 MHz (6% of f_{ctr}) in measurements. Fig. 12(b) and Fig. 12(d) also show that transmission phase is linear within the BW of interest, similar to the analytical results of Fig. 8(b).

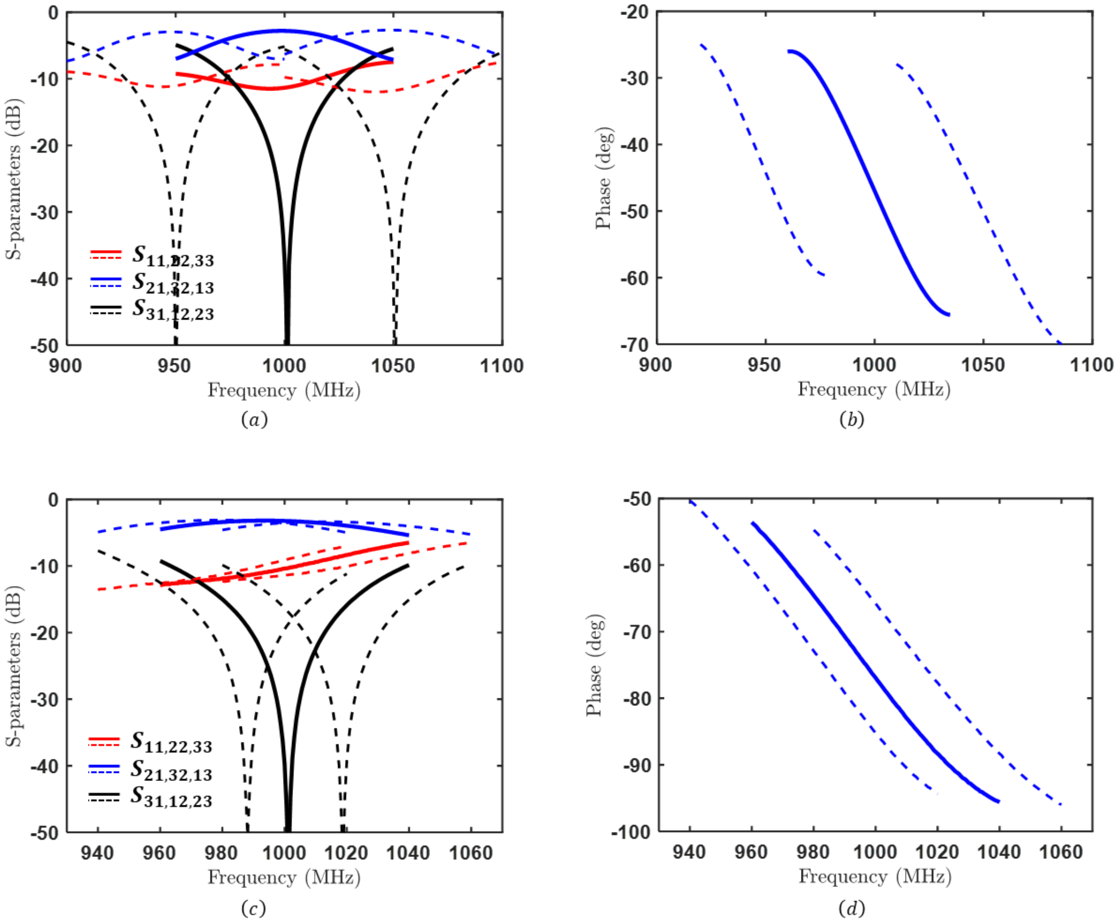

Figure 12: (a) Simulated *S*-parameters. (b) Simulated transmission phase. (c) Measured *S*-parameters. (d) Measured transmission phase.

3.2.2 SPURIOUS EMISSION

Fig. 13 shows the spectrums at both the ANT and RX ports for a monochromatic TX excitation with an input frequency f_{in} of 1 GHz and an input power P_{in} of 0 dBm. The simulated fundamental component at the ANT port is about –2.8 dBm, which indeed exhibits the same amount of IL predicted by the *S*-parameters. At the RX port, however, the fundamental component is –46 dBm, which is 9 dB larger than predicted by IX, simply because the null in Fig. 11(a) is not perfectly aligned at 1 GHz. Similar remarks apply to the measured results, i.e., the fundamental components at the ANT and RX ports in this case are –3.3 dBm and –48 dBm, respectively. On the other hand, the simulated second-order IMPs at $f_{in} - f_m$ and $f_{in} + f_m$ are both about –18 dBc, and the measured values are –18 dBc and –14 dBc, respectively. Though not shown in Fig. 11(a) and Fig. 11(b), higher-order IMPs are also present, but they are generally smaller than the second-order ones and they can be rejected with filters, therefore we can neglect them. Furthermore, one additional tone is present in simulations at $5f_m$ with an amplitude of –60 dBc while in measurements two tones are present, one at $5f_m$ and another at $6f_m$ with amplitudes of –41 dBc and –55 dBc, respectively. These are basically high-order harmonics of the modulation signals due to the varactors' non-linear CV characteristics and because of them, it is desirable not to have f_{ctr} / f_m as an integer number, in order to avoid any of these harmonics landing on top of the desired signal.

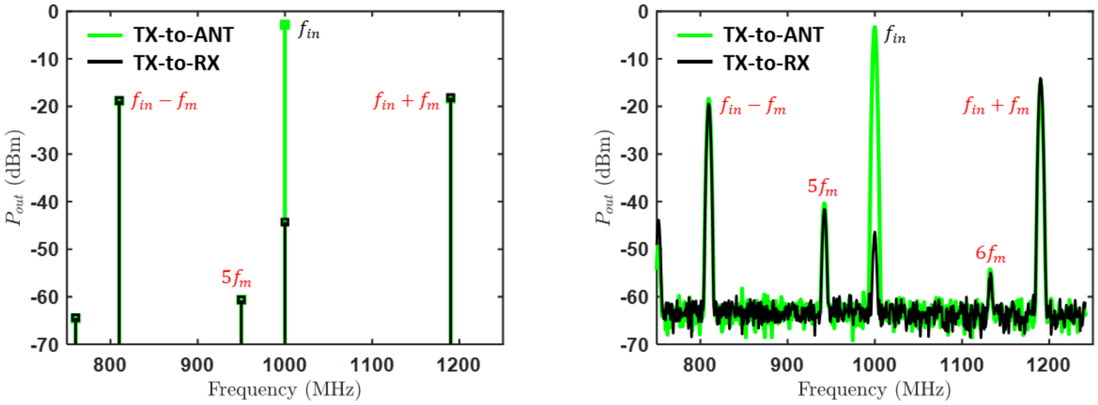

(a) (b)

Figure 13: ANT and RX spectrums for a monochromatic TX excitation with an input frequency f_{in} of 1 GHz and an input power P_{in} of 0 dBm. (a) Simulated. (b) Measured.

Obviously, such spurious emission is not satisfactory and will not pass the regulations of any practical system on such metric. While filtering may partially solve this problem by rejecting the high-order IMPs as mentioned earlier, it will be challenging to do the same for the second-order spurs at $f_{in} \pm f_m$ since they are much closer to the desired BW. Furthermore, the use of sharp filters is generally not preferable since they add more losses and increase the overall cost and form factor. More importantly, by filtering the spurs, the power carried by them is wasted, which is essentially a lossy channel to the fundamental harmonic itself. In fact, these spurs are the main reason why the IL, either in theory, simulations, or measurements, is always larger than 2.8 dB at best, and the design points for optimal IL, RL, and IX in Fig. 7 are not aligned. This issue will be discussed in more detail in Chapter 4 and will lead to the development of the differential architectures of STM-AM circulators, which partially overcome this problem. In Chapter 5, the so-called *N*-way STM-AM circulators will be presented, which permit increasing the power handling beyond tens of Watts and dramatically suppress the overall spurious emission.

3.2.3 POWER HANDLING AND LINEARITY

The limitation on power handling and linearity in STM-AM circulators originates solely from the varcaps. In the specific implementation under consideration of Fig. 5(a), these elements are built using varactors, which exhibit a finite forward conduction voltage V_f, a finite breakdown voltage V_b, and non-linear CV characteristics as given by (3.1). Obviously, the V_f and V_b thresholds impose a limitation on the maximum possible swing across the varactors. To maximize this swing, the varactors should be biased at $V_{dc} = \left(V_f + V_b\right)/2$. Clearly, as the DC bias deviates from this optimal value, e.g., as we tune the circulator for operation at a different channel, the maximum possible swing and, consequently, the circulator's power handling are both reduced. On the other hand, the exponentially non-linear CV characteristics of the varactors between the V_f and V_b thresholds degrade the circulator’s spurious emission, as explained in Sec. 3.2.2, which leads eventually to IL and IX compression, thus limiting the power handling. This can be demonstrated by substituting $v_n = V_m \cos(\omega_m t) + V_1 \cos(\omega_1 t) + V_2 \cos(\omega_2 t)$ in (3.1), which yields

$$\begin{aligned} C &= b_0 + \sum_{k=1}^{\infty} b_k \cos(k\omega_m t) + d_k \cos(k\omega_1 t) + e_k \cos(k\omega_1 t) \\ &+ \sum_{k=-\infty}^{\infty} \sum_{q=-\infty}^{\infty} \sum_{l=-\infty}^{\infty} r_{kql} \cos\left[(k\omega_m + q\omega_1 + l\omega_2) t \right] \end{aligned} , \tag{3.35}$$

where b_k, d_k, e_k, and r_{kql} are polynomial coefficients, which up to the first few terms are given by

$$\begin{aligned} b_0 &= C_0 + \frac{1}{2} a_2 \left(V_m^2 + V_1^2 + V_2^2 \right) + \cdots \\ b_1 &= a_1 V_m + \frac{3}{4} a_3 V_m^3 + \cdots \\ d_1 &= a_1 V_1 + \frac{3}{4} a_3 V_1^3 + \cdots \\ e_1 &= a_1 V_2 + \frac{3}{4} a_3 V_2^3 + \cdots \end{aligned} . \tag{3.36}$$

Notice that for simplicity, the phases of all sinusoids were neglected since they are irrelevant to this analysis. The DC term b_0 represents the effective static capacitance in the presence of large modulation and RF signals while taking into account the varactors’ non-linearities. We notice a shift in such capacitance with respect to the static value C_0 due to the second-order non-linearity. Generally, all even order terms in would result in a similar shift but the second-order one is predominant. For a convex CV curve, as for all varactors based on reverse-biased pn junctions, a_3 is positive, therefore, the resonance frequency is shifted “down” in agreement with the result in Fig. 11. For $V_1 << V_m$ and $V_2 << V_m$, this shift is constant and independent of the RF signal, however, when either V_1 or V_2 (or both) becomes sufficiently large, b_0 changes with the input power, or in other words, the varactor is compressed. Clearly, when this occurs, both IL and IX will also compress. Indeed, this is observed in the simulated and measured results of Fig. 14(a) and Fig. 14(c), respectively, which depict IL and IX versus the power P_{in} of a single input tone at 1 GHz. Specifically, the simulated 1 dB input compression point of IL (P1dB) and the 20 dB compression point of IX (IX20dB) are +28 dBm and +26.7 dBm, respectively, and the measured value of both metrics is +29 dBm.

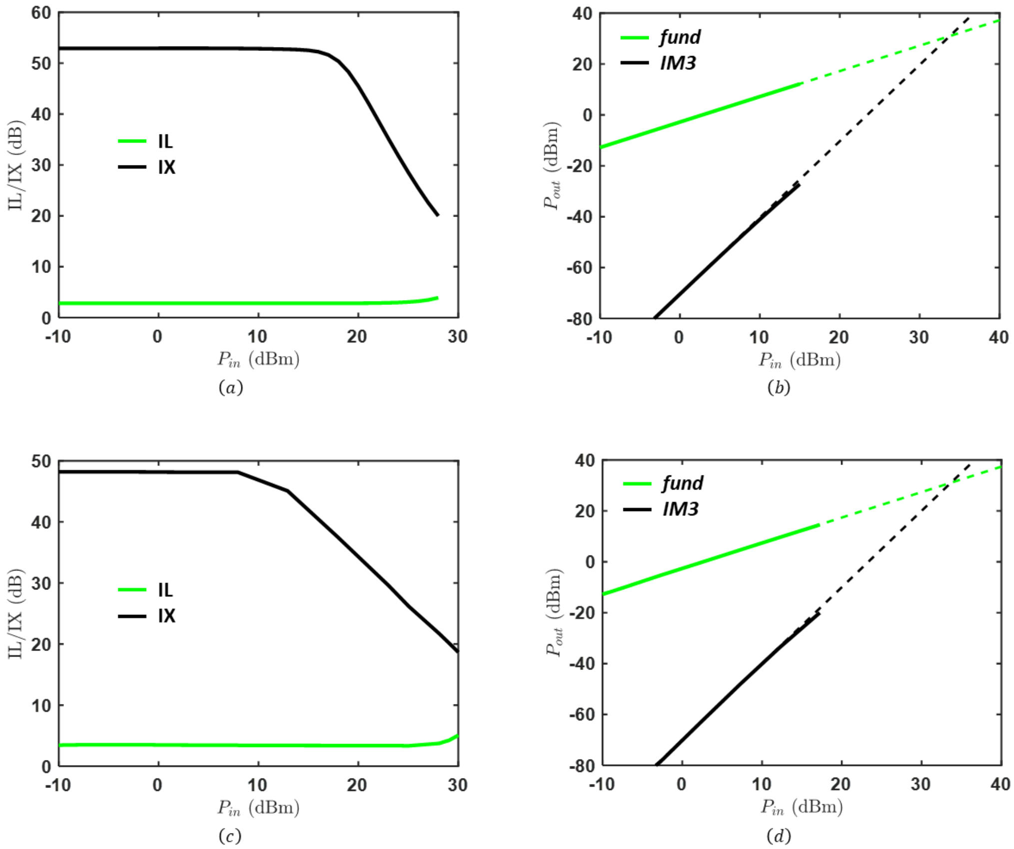

Figure 14: (a) Simulated P1dB and IX20dB. (b) Simulated IIP3. (d) Measured P1dB and IX20dB. (d) Measured IIP3.

Furthermore, since f_1 and f_2 are generally two RF frequencies close the circulator's center frequency f_{ctr}, i.e., $f_{1,2} = f_{ctr} \pm \Delta f/2$, their mixing will lead to in-band IMPs very close to f_{ctr} as well. The same remark applies to the IMPs resulting from mixing between either of these two frequencies and the relatively low modulation frequency f_m. The strength of all these mixing spurs is captured by the r_{kql} coefficients in (3.35) and their impact on the circulator's performance can be quantified by calculating the third-order input-referred intercept point (IIP3). Assuming $\Delta f = 1$ MHz, the simulated and measured IIP3 are both found to be +33.8, as shown in Fig. 14(b) and Fig. 14(d), respectively. Notice that the difference between IIP3 and P1dB, either in simulations or measurements, is not 9.6 dB as expected in third-order time-invariant systems since STM-AM circulators are, in fact, time varying. It is also worth mentioning that these values of P1dB, IX20dB, and IIP3, exceed by several orders of magnitude the results of all previous works. In fact, this is the first Watt-level magnetless circulator ever presented and experimentally validated.

3.2.4 NOISE FIGURE

Noise performance of the circulator is another critical metric since it comes at the forefront of the RX path, even superseding the low noise amplifier (LNA). Therefore, it is highly desirable that the circulator adds minimal noise in order not to limit the overall SNR of the transceiver. In the following discussion, we detail the different noise mechanisms in the STM-AM circuits and explain their impact at the circulator's performance. Although the analysis focuses on the RX port, the results also apply to the ANT and TX ports, due to the symmetry of the circuit. Total noise at the RX port can be decomposed into three components: (i) incoming noise from the ANT and TX ports, (ii) noise added by the circuit itself, and (iii) noise resulting from random variations in the modulation signals, including amplitude and phase noise.

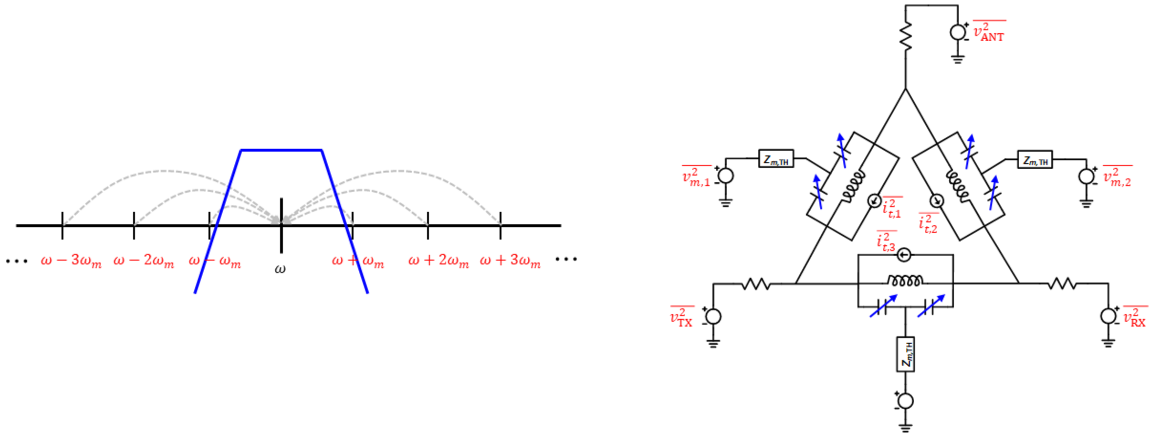

(*a*) (*b*)

Figure 15: (a) Noise folding from the IMPs into the desired BW. (b) Noise sources.

The TX and ANT noise are both transmitted to the RX port through the circulator's harmonic *S*-parameters. Notice that since the circuit is time-variant, output noise at the RX port at a particular frequency not only comes from the ANT or TX noise at the same frequency, but it also folds from the IMPs as shown in Fig. 15(a). Therefore, the RX noise due to the ANT and TX incoming noise is given by

$$\overline{v}^2_{\text{RX}}(\omega) = \sum_{k=-N}^{N} \overline{v}^2_{\text{ANT}}(\omega + k\omega_m)\left|S_{21}(\omega, \omega + k\omega_m)\right|^2 + \overline{v}^2_{\text{TX}}(\omega)\left|S_{31}(\omega, \omega + k\omega_m)\right|^2 \qquad (3.37)$$

where N is the total number of the IMPs and $\overline{v}^2_{\text{RX}}(\omega)$, $\overline{v}^2_{\text{TX}}(\omega)$, and $\overline{v}^2_{\text{ANT}}(\omega)$ are the power spectral densities (PSDs) of the RX, TX, and ANT noise, respectively. Notice that $\left|S_{31}(\omega,\omega)\right|^2 << \left|S_{21}(\omega,\omega)\right|^2$ over the circulator's BW; therefore, TX's contribution at $k = 0$ in (3.37) can be neglected. One can argue that the circulator should not be penalized by the input noise folding, since there is no desired signal at the IMPs. A channel pre-selection bandpass filter, which is similar to image reject filters in heterodyne transceivers, can thus be added at the antenna port in order to knock down this out-of-band noise as shown in Fig. 15(a). Unlike double-side band mixers, however, where the conversion gain seen by the desired signal and its image is the same, IMPs harmonic transfer functions in the circulator’s case are, in fact, much smaller than IL, therefore noise folding from IMPs is already very small compared to the in-band noise and can be neglected even without filtering. As for the noise added by the circuit itself, it is attributed to the thermal noise of the biasing resistors, the inductors’ finite quality factors, the varactors and the output impedance of the modulation sources. Fig. 15(b) shows these noise sources where noise of the biasing resistors is neglected compared to the input noise from the ports, since $R_b >> Z_0$. Also for simplicity, total noise of the *n*-th *LC* tank, either due to the varactors or the inductors, is lumped into a single parallel current source $\bar{i}_{t,n}^2$. One can split each $\bar{i}_{t,n}^2$ into two fully correlated shunt current sources with opposite currents at the two terminals of the corresponding tank, therefore allowing the calculation of their contribution at the RX port using the harmonic *S*-parameters. Furthermore, incoming noise from the modulation/DC ports is injected into the common-cathode node of the corresponding tank through a voltage source $\bar{v}_{m,n}^2$ in series with a noiseless complex impedance Z_m where $\bar{v}_{m,n}^2$ and Z_m can be found using Thevenin-equivalence looking back into the modulation ports. One can interpret $\bar{v}_{m,n}^2$ as an amplitude variation of the modulation signal applied to the varactors, which is equivalent to an effecti$\delta C_n(t)$ve random capacitance variation $\delta C_n(t)$ in (5). Similarly, phase noise of the modulation signals can be represented as a random phase $\theta_n(t)$, hence (3.4) can be rewritten as follows

$$C_n = C_0 + \left[\Delta C + \delta C_n(t)\right]\cos\left(\omega_m t + \varphi_n + \theta_n(t)\right). \tag{3.38}$$

Equation (3.38) shows that in a realistic scenario, the modulation signal is not a pure sinusoidal tone with frequency f_m, but rather a random signal with a finite bandwidth which increases the folded noise into the circulator’s instantaneous BW and further degrades its noise figure.

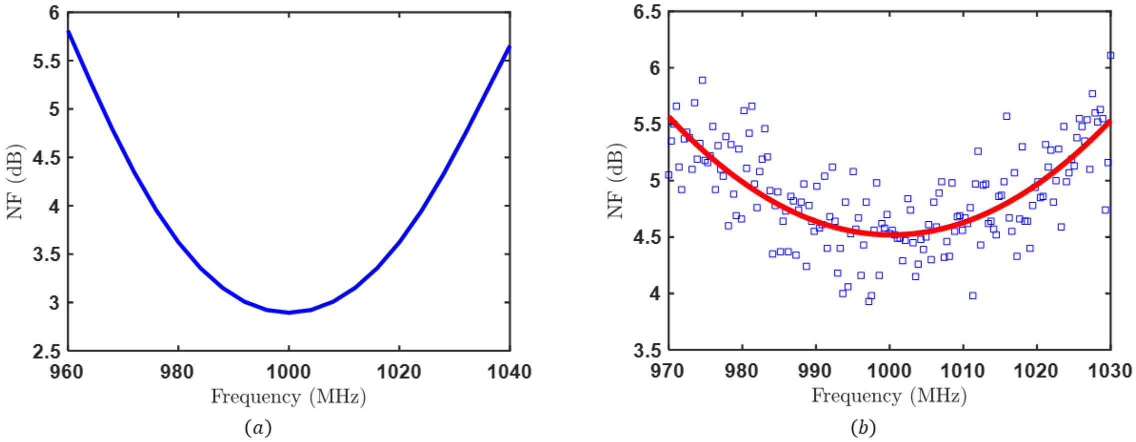

Figure 16: (a) Simulated NF. (b) Measured NF.

Analytical calculation of the exact total output noise at the RX port can be very tedious; however, simulation tools such as ADS harmonic balance significantly simplify the task. Also, since the presented circulator is a passive LPTV circuit, one should expect that the overall noise figure (NF) is approximately equal to the IL but slightly higher due to noise folding from the IMPs and phase noise in the modulation signals. Indeed, Fig. 16(a) shows that the simulated NF is 2.9 dB at 1 GHz, which is only 0.1 dB higher than IL, and less than 3.1 dB over the BW. Similarly, Fig. 16(b) shows the measured NF is 4.5 dB at 1 GHz and less than 4.7 dB over the BW.

Chapter 4: Differential STM-AM Circulators[2]

In this chapter, we develop the differential voltage- and current-mode architectures of STM-AM circulators, which improve the performance of all metrics and drastically reduce the required modulation frequency and amplitude. As an example, we provide a rigorous analysis, simulated, and measured results for the voltage-mode topology to validate the functionality of these circuits.

4.1 THEORY

As illustrated in Chapter 3, single-ended STM-AM circulators can achieve strong non-reciprocity with very good performance in many metrics, particularly, IX, P1dB, and IX20dB. However, they still suffer from several problems. Specifically, IL was shown to be limited to about 3 dB in practice, even when losses are incidental, which makes these circuits less attractive compared to passive LTI EBDs and weakens the main argument for full-duplex systems, i.e., doubling the spectral efficiency using the same resources (including energy per bit). Furthermore, it was not possible to achieve optimal IL, RL, IX, and BW simultaneously, since the required modulation parameters f_m and V_m in each case were different. Even optimizing for only one of these metrics such as IX was still problematic since it required considerably large modulation amplitude of about 10 Vpp. These problems are in fact all rooted in one issue, i.e., the generation of large IMPs in close proximity to the desired BW. It is important to make a distinction here between the IMPs due to the time-varying nature of STM-AM circulators and those resulting from non-linearities. The latter are in fact less of an issue as they are not related to the non-reciprocal operation itself of these circuits, but they are rather a secondary phenomenon. In other

---

[2] The content of this chapter is published in [38].

words, strong non-reciprocity can be achieved with perfectly linear elements and in complete absence of any non-linear IMPs. However, parametric modulation is essentially and fundamentally the mechanism that breaks reciprocity. Therefore, the IMPs resulting from it cannot be avoided, at least in single-ended implementations, and they have a strong impact on the overall performance. For instance, they draw power from the fundamental harmonic of the input signal regardless of its amplitude, thus leading to the 3 dB limit on IL even under the linear small-signal assumption. Also, since they are considerably large, i.e., only 10 dB below the fundamental harmonic, then even their partial reflections by the port impedances back into the circuit is sufficient to misalign the optimal design points of IL, RL, IX, and BW [see Fig. 7]. On the other hand, these products equally appear at all ports for excitation at a single port. Therefore, the IMPs resulting from the TX signal at the RX port could saturate its RF front-end regardless of how much isolation is achieved at the fundamental frequency. Similarly, the IMPs resulting from the RX signal at the TX port can cause instability issues to the power amplifier (PA) because of load-pull effects. More importantly, the IMPs at the ANT port, either due to the TX or the RX signal, would pose a serious interference problem to adjacent channels and would prohibit compliance with the spectral mask regulations of most commercial systems. Therefore, the rejection of these products is pivotal. Although filtering may sound a reasonable option, it is, in fact, far from being practical (at least on its own), since it suffers from many problems. Specifically, adding filters at the circulator's ports increases the overall size and degrades the total IL. It also imposes a restriction on the lowest possible modulation frequency, in order to relax the requirements on the sharpness of these filters. More importantly, if the IMPs are filtered by dissipating them into dummy resistors, for instance, then the 3 dB IL limit is not overcome. On the other hand, if they are reflected back into the circuit, this may still prohibit simultaneous optimization of all *S*-parameters. Hence, the rejection of the IMPs must be accomplished carefully in a way that permits solving all these problems. To find this optimal solution, let us consider adding a constant phase θ to all modulation signals, i.e.,

$$C_n = C_0 + \Delta C \cos\left(\omega_m t + (n-1)2\pi/3 + \theta\right). \tag{4.1}$$

One can prove from the analysis in Chapter 3, that the fundamental component of the rotating modes, i.e., $V_\pm(\omega)$ in the delta topologies and $I_\pm(\omega)$ in the wye topologies, remain exactly the same, while the IMPs at $\omega \pm \omega_m$ become

$$V_\pm\left(\omega \mp \omega_m, \omega\right) = V_\pm\left(\omega \mp \omega_m, \omega\right)\Big|_{\theta=0^\circ} e^{\pm j\theta} \tag{4.2}$$

$$I_\pm\left(\omega \mp \omega_m, \omega\right) = I_\pm\left(\omega \mp \omega_m, \omega\right)\Big|_{\theta=0^\circ} e^{\pm j\theta}. \tag{4.3}$$

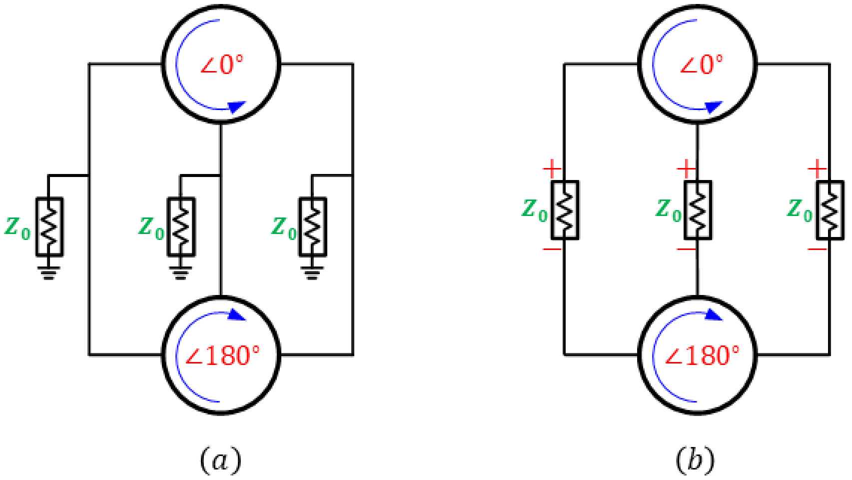

Figure 17: Differential STM-AM circulators. (a) Current-mode. (b) Voltage-mode.

This finding suggests that combining two single-ended wye topologies in parallel as shown in Fig. 17(a) or two single-ended delta topologies in series as shown in Fig. 17(b), while maintaining a constant 180 deg phase difference between their modulation signals, can cancel these products entirely. In analogy with passive mixers, we refer to these two differential circuits as the current- and voltage-mode architectures of STM-AM circulators, respectively. It is worth highlighting that the constituent single-ended circulators in the current-mode architecture must be based on either the bandpass or the bandstop wye topologies depicted in Fig. 4(a) and Fig. 4(c), respectively. This is because the IMPs in this architecture are expected to arise as out-of-phase currents at the single-ended terminals, hence they can be cancelled out by summing them up through simple nodal connection. In contrast, the single-ended circulators in the voltage-mode architecture must be constructed using either the bandstop or the bandpass delta topologies depicted in Fig. 4(b) and Fig. (d), respectively. As one may expect from duality, this is because the IMPs in this case are expected to arise as common voltages, hence they can be cancelled by subtracting them through baluns. Therefore, there are only four possible implementations of differential STM-AM circulators, namely, current-mode bandpass/wye, current-mode bandstop/wye, voltage-mode bandpass/delta, and voltage-mode bandstop/delta topologies.

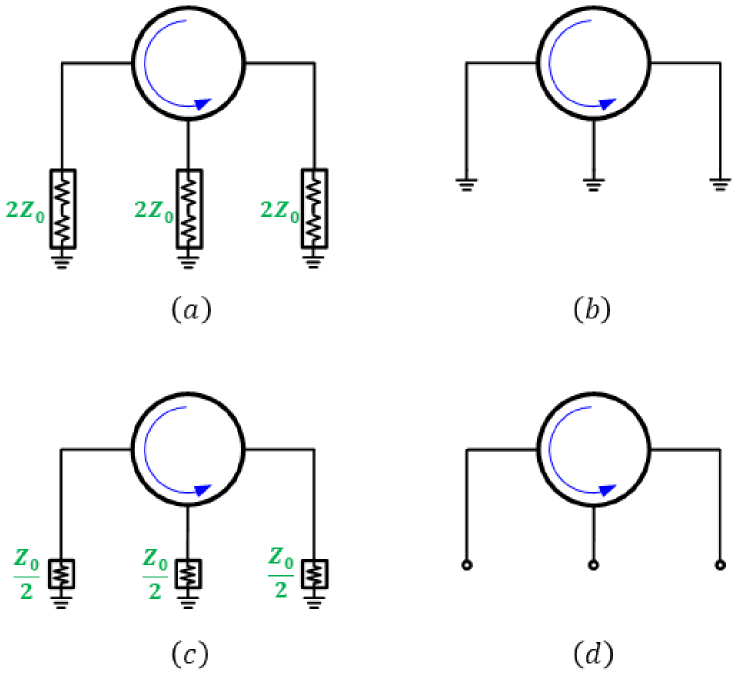

Figure 18: Half-circuit models. (a) Current-mode at the fundamental harmonic. (b) Current-mode at the second-order harmonics. (c) Voltage-mode at the fundamental harmonic. (d) Voltage-mode at the second-order IMPs.

In light of power conservation, one must wonder what happens to the power carried by the IMPs in the differential STM-AM circulators. As it turns out through rigorous analysis, this power is fully transferred back to the fundamental component and this is the reason why all metrics improve significantly. Before delving into the mathematical details of the analysis, let us examine this first intuitively by developing the half-circuit models as follows. In the current-mode architecture, the fundamental components of the constituent single-ended circuits exhibit an even symmetry, thus leading to an effective port impedance of $2Z_0$ seen by each single-ended circuit, as shown in Fig. 18(a). On the other hand, the IMPs exhibit an odd symmetry due to the 180 deg phase difference between the modulation signals of the constituent single-ended circuits, therefore the ports in this case become virtual grounds, as shown in Fig. 18(b). Unlike the fundamental components, the effective short-circuited input impedance *seen* by the IMPs prohibits any current flow, and consequently any power transfer, to the ports at these frequencies. From duality, one can find that the voltage-mode topology provides opposite symmetries, i.e., odd for the fundamental component and even for the IMPs, as shown in Fig. 18(c) and Fig. 18(d), respectively. Notice that the IMPs in this case see an effective open-circuit at all ports. From Fig. 18(b) and Fig. 18(d), one can realize that these products are entirely reflected back into the single-ended circulators either out-of-phase or in-phase thanks to the short-circuited or open-circuited ports, respectively. Consequently, they can be regarded as new input excitations at $\omega \pm \omega_m$. Notice that these products are equally present at all ports, as mentioned before, and they also maintain the same rotational phase pattern of the modulation signals that resulted in them, i.e., their phases increase by 120 deg in a particular direction. Therefore, their reflections are, in fact, either a clockwise or a counter clockwise excitation, as depicted in Fig. 2(c) and Fig. 2(d), respectively, therefore they are allowed to mix with the modulation signals again and generate new harmonics at ω, $\omega \pm \omega_m$, and $\omega \pm 2\omega_m$. The ω and $\omega \pm \omega_m$ components will enter the single-ended circulators again, mix with the modulation signals in the exact same way, and continue this recursive process until they reach a steady state when the reflections become weaker than the noise floor. On the other hand, the second-order spurs at $\omega \pm 2\omega_m$ will either leak to the ports, since they exhibit the same symmetry as the fundamental component at ω, or they will partially reflect back into the circulator, since matching at $\omega \pm 2\omega_m$ is not necessarily guaranteed. Similarly, this gives rise to new harmonics at $\omega \pm \omega_m$, $\omega \pm 2\omega_m$, and $\omega \pm 3\omega_m$. Ostensibly, this qualitative analysis suggests that the spectrum at the RF ports will contain all the even-order harmonics ω, $\omega \pm 2\omega_m$, $\omega \pm 4\omega_m$, … with decaying magnitudes. In this case, the performance improvement due to the differential configuration would be incremental and only associated with a weakening of the higher-order IMPs compared to the original second-order spurs of the single-ended circuit at $\omega \pm \omega_m$. But if one keeps track of these recursive reflections more rigorously, the steady state solution will show, quite interestingly, that the output spectrums only contain the fundamental frequency. This, however, is an exhausting and very tedious analytical task. Fortunately, a simpler approach to find this steady state solution is to analyze the entire differential circuit as a single entity, as we explain in the next section. The analysis indeed proves that the power of all higher-order harmonics are transferred back to the fundamental component, thus making the differential STM-AM circulators quasi-linear time-invariant (QLTI) networks. However, this is under the linear small-signal assumption. Since non-linearities are inevitable in any real circuit, finite IMPs will still manifest themselves in simulations and measurements, but it is important to realize that the parametric modulation does not contribute to any of these products, as explained earlier, therefore, the overall performance of many metrics dramatically improves.

4.2 ANALYSIS

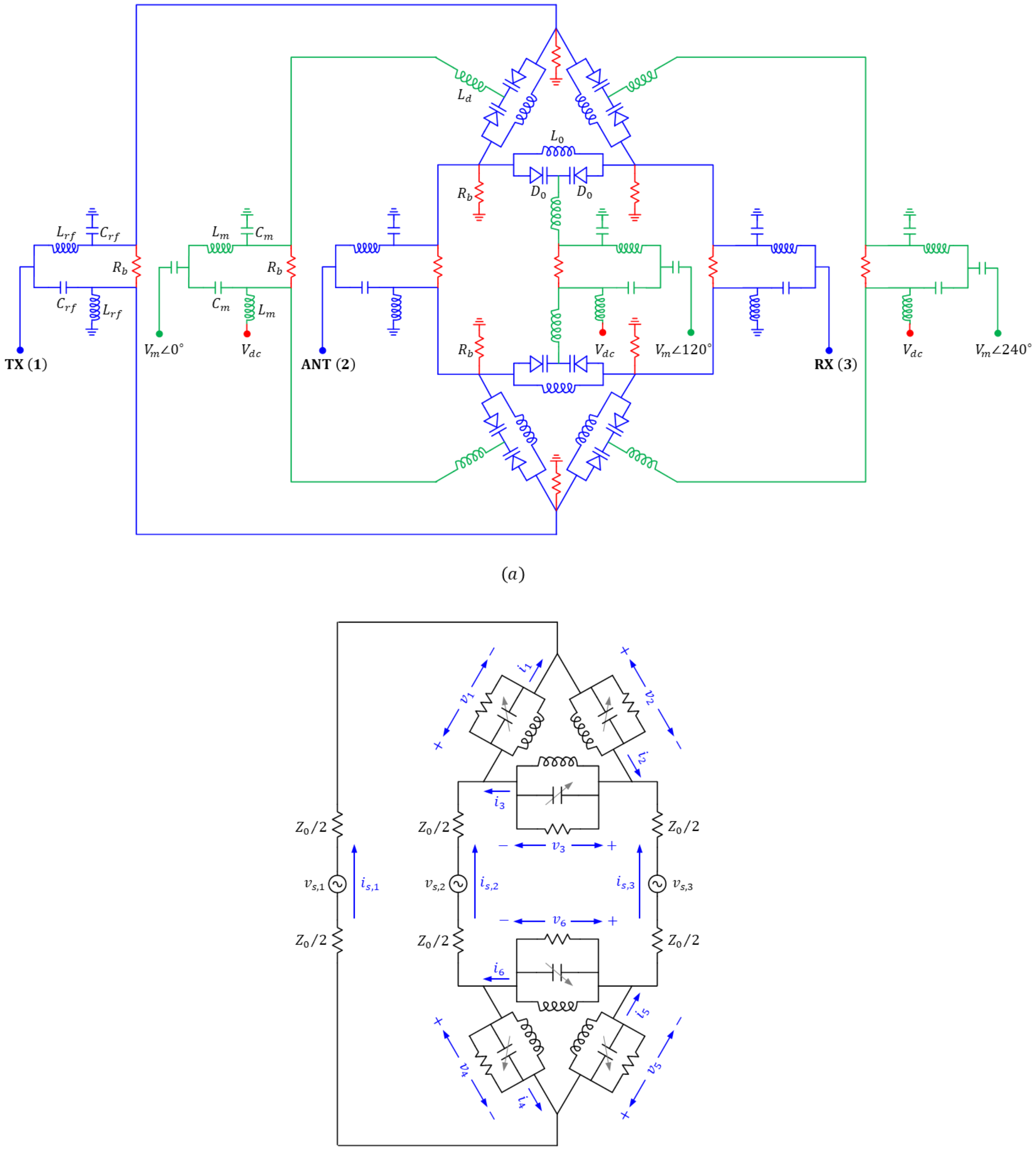

(*a*)

(*b*)

Figure 19: Voltage-mode bandstop/delta topology. (a) Complete schematic. (b) Small-signal model.

As an example, we analyze in this chapter the voltage-mode bandstop/delta topology and validate it with simulations and measurements in the next section. For completeness, we present the complete schematic and the analysis of the dual current-mode bandpass/wye topology in Appendix B. Fig. 19(a) shows the complete circuit implementation of the voltage-mode bandstop/delta STM-AM circulator, which consists of two single-ended bandstop/delta topologies connected differentially through *LC* baluns (L_{rf} and C_{rf}). Similarly, *LC* baluns (L_m and C_m) are used to generate the differential modulation signals of the constituent single-ended circuits from three sources. Recall that these sources have the same amplitude V_m and frequency f_m but their phases increase by 120 deg in the clockwise direction. Large resistors R_b are used for DC biasing and the bias voltage itself V_{dc} is injected through the shunt inductance of the modulation baluns. Also, recall that each single-ended circuit consists of three parallel *LC* tanks realized using inductors L_0 and a pair of varactors D_0. The varactors are in common-cathode configuration and the common node is connected to an inductor L_d so that they form together a bandpass resonance at f_m, allowing the modulation signal to pass through while, at the same time, prohibiting the RF signal from leaking out of the delta loop. Under the small-signal assumption, Fig. 19(a) can be simplified as shown in Fig. 19(b), where the TX, RX, and ANT ports along with the RF baluns are all replaced by differential voltage sources with a total impeance Z_0 (output impedance of the baluns). Also, the common-cathode varactors and the DC/modulation network are replaced by varcaps, the instantaneous capacitance of which is given by

$$C_n = \begin{cases} C_0 + \Delta C\cos\left(\omega_m t + \varphi_n\right), & n = 1,2,3 \quad \forall SE1 \\ C_0 - \Delta C\cos\left(\omega_m t + \varphi_n\right), & n = 4,5,6 \quad \forall SE2 \end{cases} \tag{4.4}$$

where *SE1* and *SE2* are the constituent single-ended circulators, C_0 is the static capacitance of the common-cathode varactors as set by the DC bias and ΔC is the effective capacitance variation which is proportional to the modulation voltage V_m. We also assume that the varactors' and the inductors' losses of each tank are combined into a non-dispersive parallel resistance $R_0 = Q_0 \omega_0 L_0$, where Q_0 is the unloaded quality factor of the tanks.

From Chapter 3, the single-ended circulators, denoted by *SE1* and *SE2*, are known to be governed by the following differential equations

$$\left(C_0 \bar{\bar{G}} + \Delta C \bar{\bar{G}} \overline{\overline{C_c}}\right) \bar{v}''_{SE1} + \left(\frac{1}{R_0} \bar{\bar{G}} - \Delta C \omega_m \bar{\bar{G}} \overline{\overline{C_s}}\right) \bar{v}'_{SE1} + \frac{1}{L_0} \bar{\bar{G}} \bar{v}_{SE1} = -\bar{i}'_s \tag{4.5}$$

$$\left(C_0 \bar{\bar{G}} + \Delta C \bar{\bar{G}} \overline{\overline{C_c}}\right) \bar{v}''_{SE2} + \left(\frac{1}{R_0} \bar{\bar{G}} - \Delta C \omega_m \bar{\bar{G}} \overline{\overline{C_s}}\right) \bar{v}'_{SE2} + \frac{1}{L_0} \bar{\bar{G}} \bar{v}_{SE2} = \bar{i}'_s , \tag{4.6}$$

where $\bar{v}_{SE1} = \{v_1, v_2, v_3\}$ and $\bar{v}_{SE2} = \{v_4, v_5, v_6\}$ are the vectors of the tank voltages, $\bar{i} = \{i_{s,1}, i_{s,2}, i_{s,3}\}$ is the vector of the source currents flowing into *SE1* and out of *SE2*, and the matrices $\bar{\bar{U}}$, $\bar{\bar{C}}_c$, and $\bar{\bar{C}}_s$ were all defined in Chapter 3. In order to simplify the analysis, the tank voltages $\bar{v}_{SE1}$ and $\bar{v}_{SE2}$ can be replaced by their differential ($\bar{v}_d$) and common ($\bar{v}_c$) components as follows

$$\bar{v}_{SE1} = \bar{v}_c + \bar{v}_d \tag{4.7}$$

$$\bar{v}_{SE2} = \bar{v}_c - \bar{v}_d \, . \tag{4.8}$$

In this case, the port terminations of Fig. 19(b) results in the following boundary equation

$$\bar{\bar{G}} \bar{i}_s = \frac{1}{Z_0} \bar{\bar{G}} \bar{v}_s + \frac{2}{Z_0} \left(\bar{\bar{G}} - \bar{\bar{U}}\right) \bar{v}_d \, . \tag{4.9}$$

Substituting (4.7)-(4.9) into (4.5) and (4.6) yields

$$C_0 \bar{\bar{J}} \bar{v}_d'' + \left(\frac{1}{R_0} \bar{\bar{J}} - \frac{2}{Z_0} \left(\bar{\bar{U}} - \bar{\bar{G}} \right) \right) \bar{v}_d' + \frac{1}{L_0} \bar{\bar{J}} \bar{v}_d + \Delta C \bar{\bar{J}} \bar{\bar{C}}_c \bar{v}_c'' - \Delta C \omega_m \bar{\bar{J}} \bar{\bar{C}}_s \bar{v}_c' = -\frac{1}{Z_0} \bar{\bar{G}} \bar{v}_s' \tag{4.10}$$

$$C_0 \bar{v}_c'' + \frac{1}{R_0} \bar{v}_c' + \frac{1}{L_0} \bar{v}_c + \Delta C \bar{\bar{C}}_c \bar{v}_d'' - \Delta C \omega_m \bar{\bar{C}}_s \bar{v}_d' = 0\,, \tag{4.11}$$

where $\bar{\bar{J}} = \bar{\bar{G}}^2$ as defined in Chapter 3. Similar to the analysis of the single-ended circuit in Chapter 3, (4.10) and (4.11) can be further simplified if we express $\bar{v}_d$ and $\bar{v}_c$ as a superposition of their in-phase, clockwise, and counter-clockwise modes as follows

$$\bar{v}_d = \bar{\bar{T}} \hat{v}_d \tag{4.12}$$

$$\bar{v}_c = \bar{\bar{T}} \hat{v}_c\,, \tag{4.13}$$

where $\hat{v}_d = \{v_{d,0}, v_{d,+}, v_{d,-}\}$ and $\hat{v}_c = \{v_{c,0}, v_{c,+}, v_{c,-}\}$ are the vectors of the modal voltages for the differential and common components, respectively, and the operator $\bar{\bar{T}}$ is given by (3.19). If we further assume that $\bar{v}_s = \{1, 0, 0\}$ and recognize that the in-phase voltages $v_{d,0}$ and $v_{c,0}$ are both equal to zero, then substituting (4.12) and (4.13) into (4.10) and (4.11) results in

$$\begin{gathered} \frac{\Delta C}{2C_0} \begin{pmatrix} 0 & e^{-j\omega_m t} \\ e^{+j\omega_m t} & 0 \end{pmatrix} \begin{pmatrix} v_{c,+}'' \\ v_{c,-}'' \end{pmatrix} - j \frac{\Delta C}{2C_0} \omega_m \begin{pmatrix} 0 & e^{-j\omega_m t} \\ -e^{+j\omega_m t} & 0 \end{pmatrix} \begin{pmatrix} v_{c,+}' \\ v_{c,-}' \end{pmatrix} \\ + \begin{pmatrix} v_{d,+}'' \\ v_{d,-}'' \end{pmatrix} + \frac{2R_0 + 3Z_0}{3R_0 Z_0 C_0} \begin{pmatrix} v_{d,+}' \\ v_{d,-}' \end{pmatrix} + \frac{1}{L_0 C_0} \begin{pmatrix} v_{d,+} \\ v_{d,-} \end{pmatrix} = \frac{-2/\sqrt{3}}{Z_0 C_0} \begin{pmatrix} e^{+j\pi/6} \\ e^{-j\pi/6} \end{pmatrix} v_{s,1}' \end{gathered} \tag{4.14}$$

$$\begin{gathered} \begin{pmatrix} v_{c,+}'' \\ v_{c,-}'' \end{pmatrix} + \frac{1}{R_0 C_0} \begin{pmatrix} v_{c,+}' \\ v_{c,-}' \end{pmatrix} + \frac{1}{L_0 C_0} \begin{pmatrix} v_{c,+} \\ v_{c,-} \end{pmatrix} + \frac{\Delta C}{2C_0} \begin{pmatrix} 0 & e^{-j\omega_m t} \\ e^{+j\omega_m t} & 0 \end{pmatrix} \begin{pmatrix} v_{d,+}'' \\ v_{d,-}'' \end{pmatrix} \\ - j \frac{\Delta C}{2C_0} \omega_m \begin{pmatrix} 0 & e^{-j\omega_m t} \\ -e^{+j\omega_m t} & 0 \end{pmatrix} \begin{pmatrix} v_{d,+}' \\ v_{d,-}' \end{pmatrix} = 0 \end{gathered}\,. \tag{4.15}$$

Fourier transforming (4.14) and (4.15) yields

$$\frac{V_{d,\pm}(\omega)}{V_{s,1}(\omega)}=\frac{\dfrac{j\omega\, e^{\pm j\pi/6}}{3\sqrt{3}Z_0C_0}\left[(\omega\pm\omega_m)^2-\dfrac{1}{R_0C_0}\,j(\omega\pm\omega_m)-\dfrac{1}{L_0C_0}\right]}{D_\pm(\omega)} \tag{4.16}$$

$$\frac{V_{c,\mp}(\omega\pm\omega_m)}{V_{s,1}(\omega)}=\frac{-j\left(1\pm j/\sqrt{3}\right)}{12}\frac{\dfrac{\Delta C}{Z_0C_0{}^2}\omega^2(\omega\pm\omega_m)}{D_\pm(\omega)}, \tag{4.17}$$

where

$$\begin{aligned}D_\pm(\omega)=&-\left(\frac{\Delta C}{2C_0}\right)^2\omega^2(\omega\pm\omega_m)^2+\left[\omega^2-\frac{2R_0+3Z_0}{3R_0Z_0C_0}\,j\omega-\frac{1}{L_0C_0}\right]\\&\times\left[(\omega\pm\omega_m)^2-\frac{1}{R_0C_0}\,j(\omega\pm\omega_m)-\frac{1}{L_0C_0}\right]\end{aligned}. \tag{4.18}$$

Equations (4.16) and (4.17) show that the only frequency components existing in the circuit are the fundamental harmonics at ω and the second-order IMPs at $\omega\pm\omega_m$ without any additional higher-order products, as claimed in Sec. 4.1. Also, the fundamental harmonics are exclusively excited as differential components, allowing them to flow to the ports while the second-order IMPs are exclusively excited as in-phase components, hence they are trapped inside the resonant junction and cannot carry power to the external ports. This result shows that, under the linear small-signal assumption, the proposed circulator hides the intrinsic time-variant characteristics from the external ports, making it essentially a quasi-LTI circuit. In order to find the *S*-parameters, the original source currents $\bar{I}_s=\{I_{s,1},I_{s,2},I_{s,3}\}$ are calculated first from their rotating-modes using

$$I_{s,n}(\omega)=e^{j(n-1)2\pi/3}I_{s,+}(\omega)+e^{-j(n-1)2\pi/3}I_{s,-}(\omega). \tag{4.19}$$

Finally, the *S*-parameters can be calculated as follows

$$S_{11}(\omega)=2\left[-\frac{1}{6}-\frac{V_{d,+}(\omega)+V_{d,-}(\omega)}{V_{s,1}(\omega)}+\frac{j}{\sqrt{3}}\frac{V_{d,+}(\omega)-V_{d,-}(\omega)}{V_{s,1}(\omega)}\right] \tag{4.20}$$

$$S_{21}(\omega)=2\left[\frac{1}{3}+\frac{V_{d,+}(\omega)+V_{d,-}(\omega)}{V_{s,1}(\omega)}+\frac{j}{\sqrt{3}}\frac{V_{d,+}(\omega)-V_{d,-}(\omega)}{V_{s,1}(\omega)}\right] \tag{4.21}$$

$$S_{31}(\omega)=2\left[\frac{1}{3}-j\frac{2}{\sqrt{3}}\frac{V_{d,+}(\omega)-V_{d,-}(\omega)}{V_{s,1}(\omega)}\right]. \tag{4.22}$$

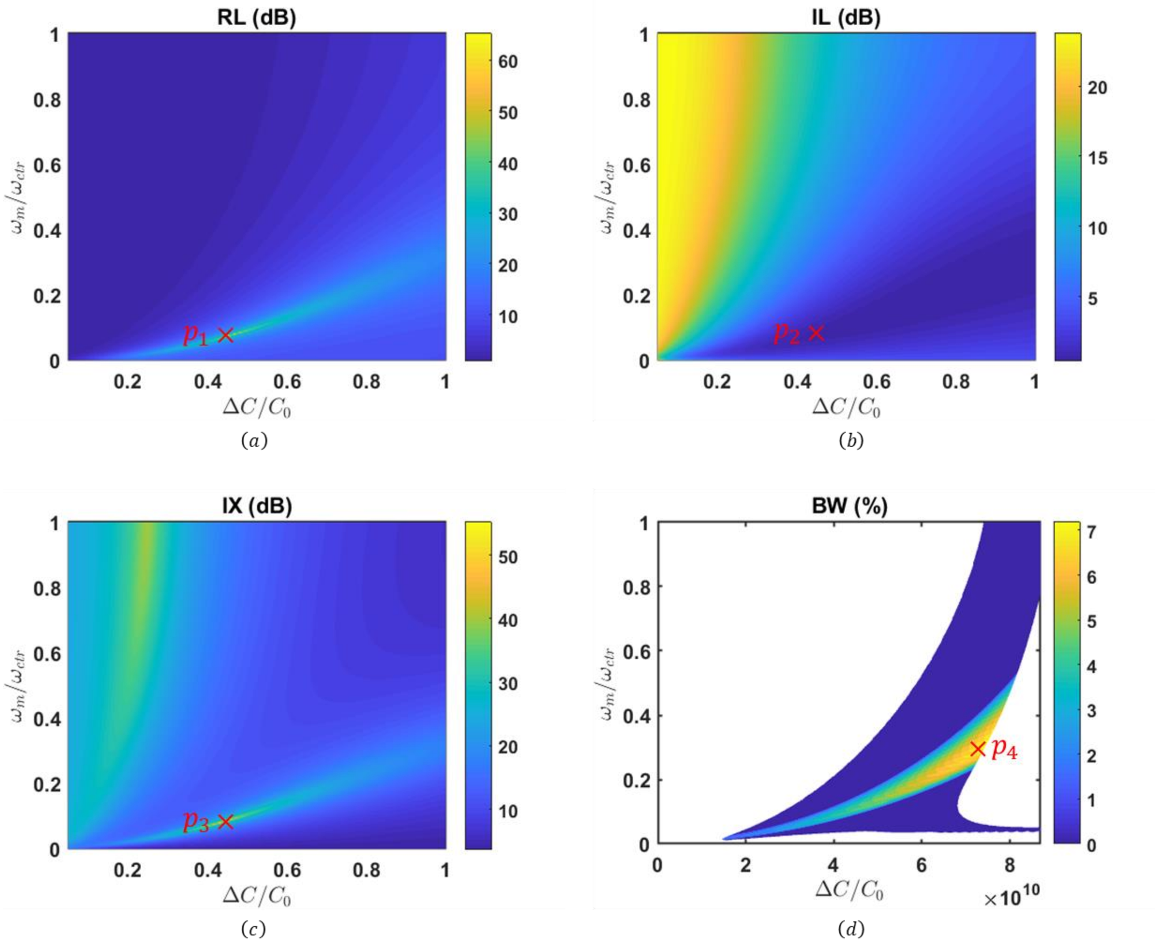

Figure 20: Analytical *S*-parameters at ω_{ctr} versus the normalized modulation parameters ω_m/ω_{ctr} and $\Delta C/C_0$. (a) RL. (b) IL. (c) IX. (d) BW.

Due to the circulator's threefold rotational symmetry, the rest of the *S*-parameters can be found by rotating the indices as $(1,2,3)\to(2,3,1)\to(3,1,2)$. With proper choice of the circuit elements and modulation parameters, $V_{d,\pm}$ can be designed to destructively interfere at one port and sum up at the other, as required to achieve infinite isolation. More specifically, port 3 can be isolated if $V_{d,\pm}/V_{s,1}=\mp j\big/\left(4\sqrt{3}\right)$, which, when substituted in (4.16) , results in the following two conditions

$$\frac{\left[\left(\omega_{ctr}+\omega_m\right)^2-\omega_0^2\right]\left[\omega_{ctr}^2+\dfrac{\sqrt{3}\omega_0}{Q_l}\omega_{ctr}-\omega_0^2\right]}{\left[\left(\omega_{ctr}-\omega_m\right)^2-\omega_0^2\right]\left[\omega_{ctr}^2-\dfrac{\sqrt{3}\omega_0}{Q_l}\omega_{ctr}-\omega_0^2\right]}=\frac{\left(\omega_{ctr}+\omega_m\right)^2}{\left(\omega_{ctr}-\omega_m\right)^2} \tag{4.23}$$

$$\left(\frac{\Delta C}{2C_0}\right)^2=\frac{\left[\left(\omega_{ctr}\pm\omega_m\right)^2-\omega_0^2\right]\left[\omega_{ctr}^2\pm\dfrac{\sqrt{3}\omega_0}{Q_l}\omega_{ctr}-\omega_0^2\right]}{\omega_{ctr}^2\left[\omega_{ctr}^2\pm\omega_m^2\right]}, \tag{4.24}$$

where $Q_l=Q_0\,||\,Q_r$ and $Q_r=\omega_0\left(3Z_0/2\right)C_0$ (recall that $Q_0=\omega_0R_0C_0$ is the unloaded quality factor of the resonant tanks). For operation at a given frequency ω_{ctr}, (4.23) and (4.24) can be used to calculate the required modulation parameters ω_m and ΔC to achieve infinite isolation. Quite interestingly, the same conditions lead to unitary transmission at the third port, assuming a lossless circuit. Also, from power conservation, this leads to perfect matching at the input port. Therefore, the proposed differential circuits allow, in the lossless case, to realize an ideal circulator with *S*-matrix given by

$$\bar{\bar{S}}=\begin{bmatrix}0&0&1\\1&0&0\\0&1&0\end{bmatrix}. \tag{4.25}$$

In order to get further insight into this result, Fig. 20 shows the IL, RL, IX at the circulator's center frequency f_{ctr}, and the fractional BW around such frequency, versus the normalized modulation parameters ω_m/ω_{ctr} and $\Delta C/C_0$, assuming $Z_0 = 50\,\Omega$, $Q_0 = 70$, and $f_{ctr} = 1$ GHz. It can be seen that indeed the required modulation parameters to optimize RL, IL, and IX as indicated by points p_1, p_2, and p_3, respectively, are nearly the same (the negligible misalignment is due to the finite Q_0). However, the optimal point p_4 that maximizes the BW is still greatly misaligned and it generally requires a larger f_m. Recall that the BW was defined as the maximum frequency range to maintain a 3 dB IL and a 20 dB IX. Obviously, the BW is maximized by trading off the values of IL, RL, and IX at the center frequency, similar to any other RF component such as amplifiers and filters. Since the BW is a more relevant metric in practice and it is even desirable to minimize the dispersion of the in-band IX in particular to simplify the design of the following layers of SIC in full-duplex systems, then we choose to design the circuit in this chapter to maximize it. But the capacitance ratio at p_4 is impractical, therefore we operate at $\Delta C/C_0 = 0.5$ and $f_m/f_{ctr} = 0.1$, which assumes the maximum realistic capacitance variation of commercial off-the-shelf varactors, hence results in the best possible realistic BW, and at the same time is close to p_2 where IL becomes minimum. The values of all design parameters are summarized in Table 2 for convenience. In such a case, Fig. 21(a) shows the analytical *S*-parameters where IL, RL, and IX at the center frequency are 0.6 dB, 27.5 dB, and 31.5 dB, respectively, and the BW is 3.6% (36 MHz). For the sake of comparison, Fig. 21(b) shows the *S*-parameters of a single-ended circulator designed using the same modulation parameters where the results are clearly much worse. Specifically, IL, RL, and IX at 1 GHz all degrade to 2.31 dB, 21.8 dB, and 10 dB, respectively, and the BW becomes undefined since the minimum level of 20 dB IX is not satisfied.

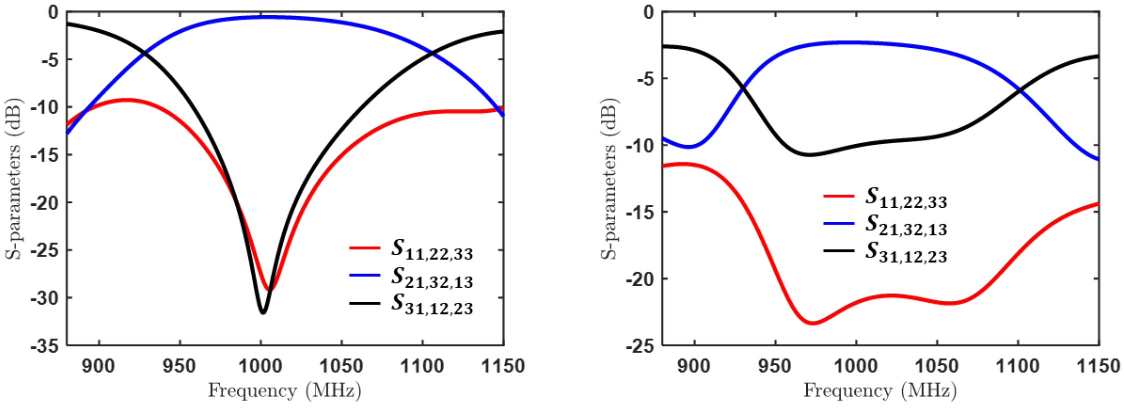

(a) (b)

Figure 21: Comparison between the analytical *S*-parameters of single-ended and differential STM-AM circulators. (a) Differential. (b) Single-ended.

Fig. 22 also shows a comparison between the ANT and RX spectrums of both single-ended and differential circuits for a monochromatic TX excitation with an input frequency f_{in} of 1 GHz and an input power P_{in} of 0 dBm. As expected, the differential circulator is IM-free which justifies the low IL of only 0.6 dB. The single-ended circuit, on the other hand, suffers from large –12 dBc second-order products in close proximity to the input frequency of 1 GHz (only ± 100 MHz apart), which also justifies the larger IL of 2.3 dB and the very low IX of only 10 dB. It is worth mentioning that these remarks hold for input excitation at any other port or any other frequency.

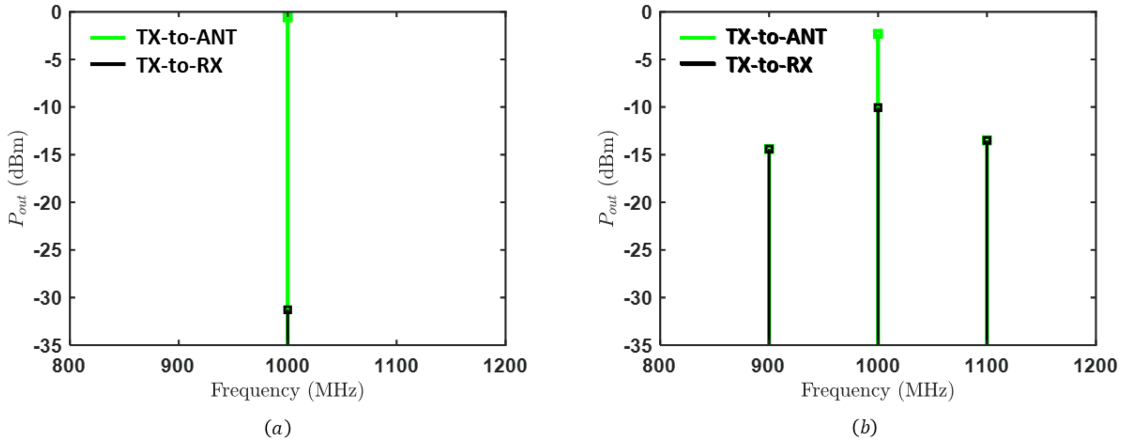

Figure 22: Comparison between the analytical spectrums of single-ended and differential STM-AM circulators. (a) Differential. (b) Single-ended.

4.3 RESULTS

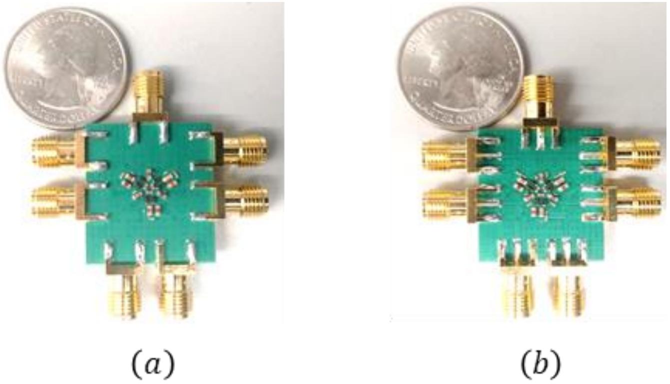

Figure 23: Photograph of the fabricated differential STM-AM circulator. (a) Top view. (b) Bottom view.

Based on the theoretical analysis presented in Sec. 4.2, a differential voltage-mode bandstop/delta STM-AM circulator operating at 1 GHz was designed in Keysight ADS. The performance was optimized through post-layout circuit/EM co-simulations by combining commercially available measured *S*-parameters for all lumped elements with the layout parasitics extracted by ADS Momentum full-wave analysis. The circuit was then fabricated and tested on a printed circuit board (PCB) using commercial off-the-shelf discrete components as listed in Table 2. Fig. 23 shows a photograph of the board and the circulator's form factor is 2×(13mm×11mm). Notice that both the top and bottom sides of the PCB are populated, each with one single-ended circulator to have a symmetric and more compact layout. The measured results were obtained using the experimental setups discussed in Appendix A, and they are all in excellent agreement with simulations.

Element\Value		Theo.		Sim.	Meas.
Main circuit	f_{ctr} (MHz)	1000		1000	1000
	f_m/f_{ctr} (%)	10		10	10
	L_0 (nH)	2.23	$Q_0 = 70$	4.3 (Coilcraft)	4.3 (Coilcraft)
	C_0 (pF)	11.5		BBY55 (Infineon)	BBY55 (Infineon)
	$\Delta C/C_0$ (%)	50			
	L_{rf} (nH)	N/R		11 (Coilcraft)	11 (Coilcraft)
	C_{rf} (pF)	N/R		2.2 (Murata)	2.2 (Murata)
Modulation network	V_m (Vpp)	N/R		3	2.3
	L_d (nH)	N/R		150 (Coilcraft)	150 (Coilcraft)
	L_m (nH)	N/R		56 (Coilcraft)	56 (Coilcraft)
	C_m (pF)	N/R		43 (Murata)	43 (Murata)
DC bias network	V_{dc} (Volt)	N/R		8.5	7.3
	R_b (KOhm)	N/R		100 (KOA)	100 (KOA)
	C_b (pF)	N/R		1000 (Murata)	1000 (Murata)

Table 2: Values of all design parameters used in obtaining the theoretical, simulated, and measured results of the differential voltage-mode bandstop/delta STM-AM circulator.

4.3.1 *S*-PARAMETERS

Fig. 24 shows the *S*-parameters in magnitude and phase in different channels. The maximum simulated and measured tunability ranges were found to be 100 MHz and 60 MHz, respectively. Also, the simulated IL, RL, and IX at the center frequency of all channels are 1.7 dB, 22 dB, and 24 dB, respectively, and the fractional BW is 2.3% (23 MHz). Similarly, the measured IL, RL, and IX at the circulator's center frequency of 1 GHz are 1.78 dB, 23 dB, and 24 dB, respectively, and the fractional BW is 2.3% (23 MHz). Clearly, simulated and measured *S*-parameters are in excellent agreement, yet they are different than the theoretical results in Fig. 21(b). This is partially due to the additional parasitics of real components but more importantly because of the RF baluns which were neglected in the small-signal analysis of Sec. 4.2 for simplicity. The additional losses incurred by these baluns are estimated using circuit/EM co-simulations to be 0.5 dB each, which if de-embedded from the measured results, the actual IL of the differential circulator becomes 0.78 dB. Obviously, this is in excellent with the theoretical results of Fig. 21(b). To the best of our knowledge, this is the lowest IL of all passive magnetless circulators presented to the date of writing this dissertation. Notice that the inband transmission phase is also linear, similar to the single-ended circuits.

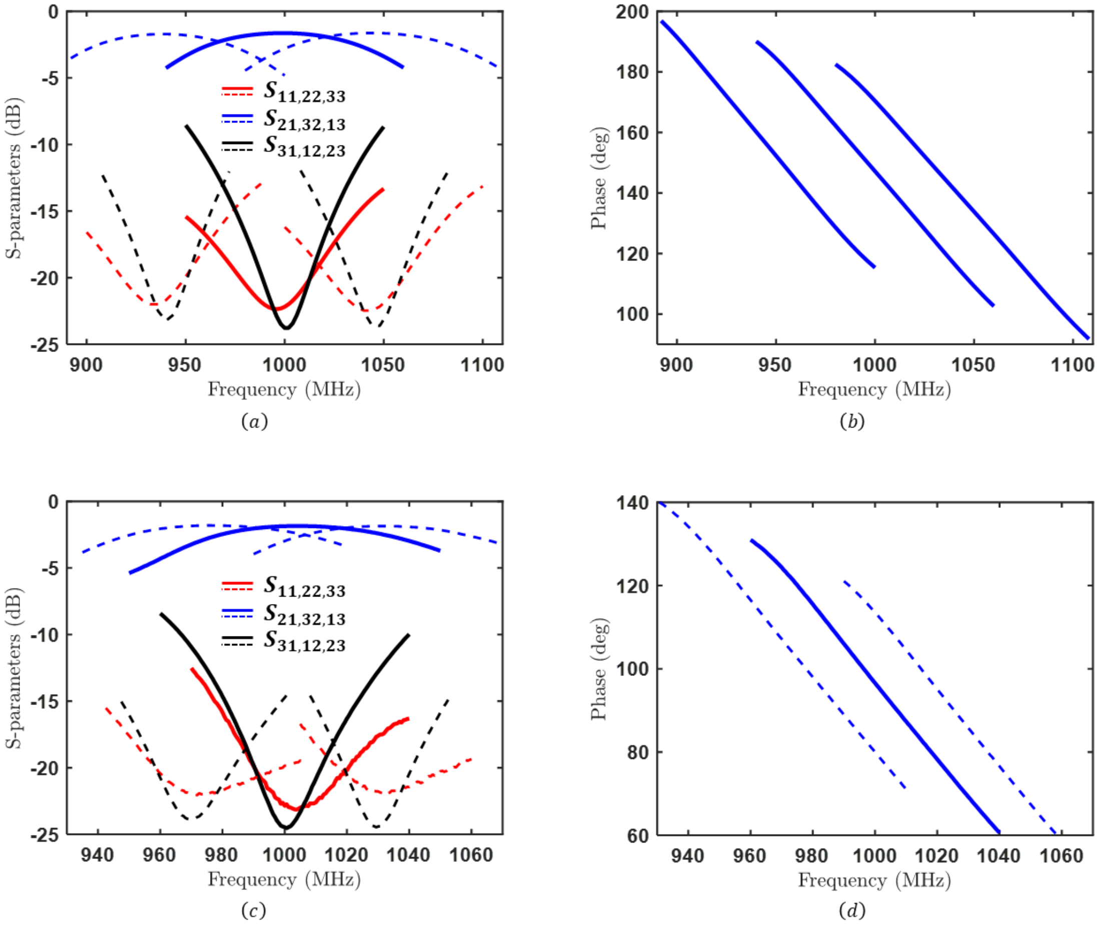

Figure 24: (a) Simulated *S*-parameters. (b) Simulated transmission phase. (c) Measured *S*-parameters. (d) Measured transmission phase.

4.3.2 SPURIOUS EMISSION

Fig. 25 shows the harmonic spectrums at the ANT and RX ports for a monochromatic TX excitation with an input frequency f_{in} of 1 GHz and an input power P_{in} of 0 dBm. In contrast to the linear small-signal results of Fig. 22(b), the simulated and measured IMPs are still finite. Specifically, the second-order spurs at $f_{in} \pm f_m$ are both about –32 dBc in simulations and –29 dBc in measurements. Higher order products are also of the same value, approximately. Such non-zero spurious emission is mainly due to the non-linear CV characteristics of the varactors, as explained earlier, and also due to layout asymmetries, random variations in the used elements, or modulation phase errors, which both lead to finite imbalance between the constituent single-ended circuits. However, the impact of this imbalance in the design under consideration is insignificant as can be deduced from the fact that the measured IMPs are in good agreement with simulations where this issue is neglected. Compared to the single-ended design presented in Chapter 3, the IMPs herein are at least 17 dB smaller (=1/50), even though f_m was reduced from 190 MHz to only 100 MHz. Furthermore, the contribution of parametric modulation to these products has become negligible, as evident by the reduction of the measured IL from 3.3 dB to 1.78 dB.

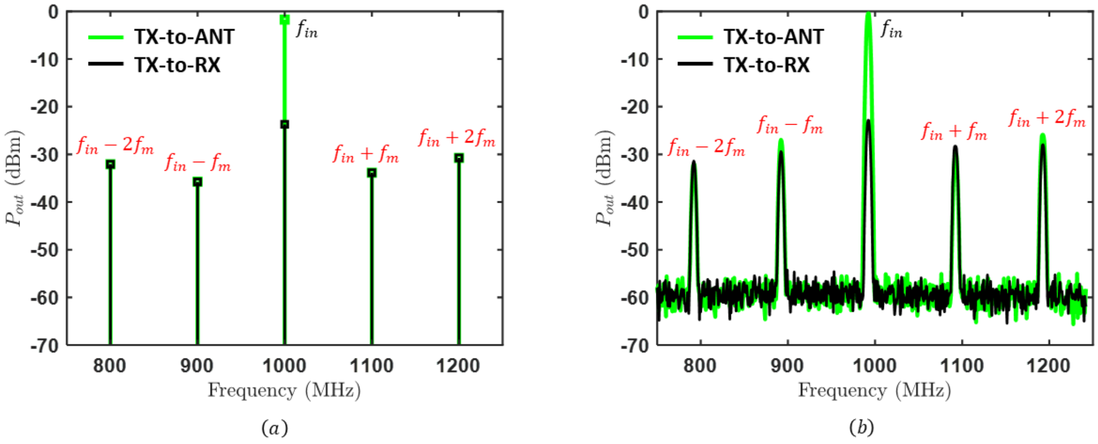

Figure 25: ANT and RX spectrums for a monochromatic TX excitation with an input frequency f_{in} of 1 GHz and an input power P_{in} of 0 dBm. (a) Simulated. (b) Measured.

4.3.3 POWER HANDLING AND LINEARITY

Fig. 26(a) and Fig. 26(c) show the IL and IX versus the power P_{in} of a single input tone at 1 GHz. The simulated P1dB and IX20dB are both +30 dBm while the measured value, also for both metrics, is +28 dBm. We also notice a peaking in IX before it starts to compress. This is because the capacitance variation $\Delta C/C_0$ at such high power levels is effectively reduced by the varactors' even-order non-linearities as explained in Sec. 3.2.3 [see Eq. (3.35) and (3.36)], hence the operation point in the design charts shown in Fig. 20 is shifted down closer to p_3 where IX becomes maximum. Fig. 26(b) and Fig. 26(d) also show the simulated and measured results of the two-tone test, respectively. The simulated and measured IIP3 are found to be +33.8 dBm and +31 dBm, respectively. It is worth mentioning that the measured P1dB of this differential circuit is 1 dB less than that of the single-ended design presented in Chapter 3, solely because the varactors used herein have a lower breakdown voltage. If the same varactor were used in both implementations, the differential architecture would, in fact, increase both P1dB and IX20dB by +3 dB, since the input power would be halved between the constituent single-ended circuits. Also, the reason why different varactors were used in both designs is that the modulation parameters f_m/f_{ctr} and $\Delta C/C_0$ are very different, which, in turn, requires varactors with different CV characteristics. Despite this artifact, the results of Fig. 26 are still amongst the largest compression points and highest linearity of all magnetless circulators presented to the date of writing this dissertation.

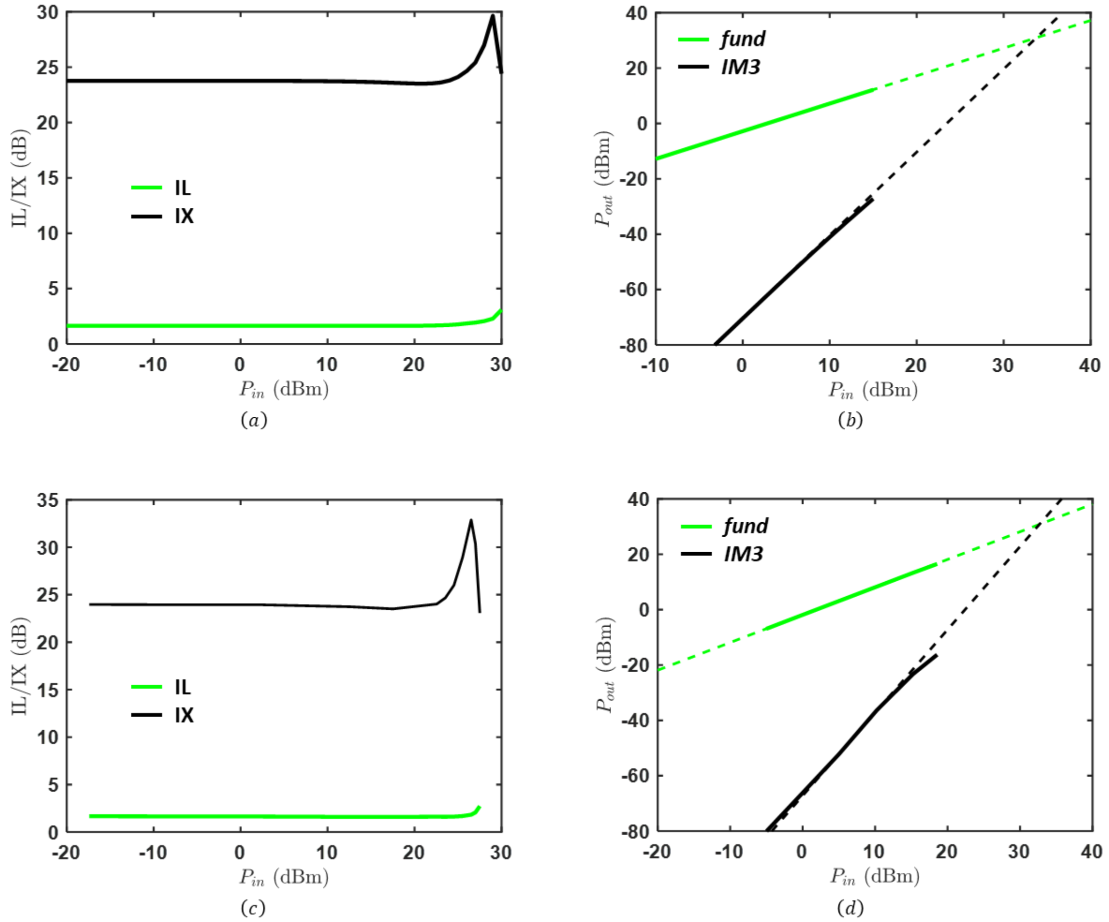

Figure 26: (a) Simulated P1dB and IX20dB. (b) Simulated IIP3. (d) Measured P1dB and IX20dB. (d) Measured IIP3.

4.3.4 NOISE FIGURE

As explained in Chapter 3, different mechanisms contribute to the NF of STM-AM circulators. This includes incoming noise from the RF ports, which remains the same as in the single-ended topologies, assuming the typical 50 Ohm termination in both cases. However, noise generated by the circuit itself is doubled. In fact, the voltage-mode topology increases it even further because of the additional loss incurred by the RF baluns. Notice that the current-mode topology does not have this problem, as explained earlier.

Amplitude and phase noise in the modulation sources also add to the total NF, yet if the anti-phase STM-AM bias of the constituent single-ended circulators is generated from the same sources, as is this case herein, then this noise becomes strongly correlated at the terminals of the differential ports and, therefore, cancels out. Noise folding from the IMPs also adds to the NF, but since the proposed differential circuits reduce these products, then their contribution becomes negligible. The reduction of the last two noise mechanisms, i.e., from the modulation sources and due to folding, is stronger than the increased thermal noise generated by the circuit, therefore the overall NF improves. In fact, since the differential circuits are passive QLTI networks, the NF should be expected to be very close to the IL. Indeed, Fig. 27 shows that the simulated and measured NF at 1 GHz are 2.5 dB and 1.8 dB, respectively, which are both nearly equal to the simulated and measured IL, respectively. To the best of our knowledge, this is the smallest NF of all magnetless circulators presented to the date of writing this dissertation.

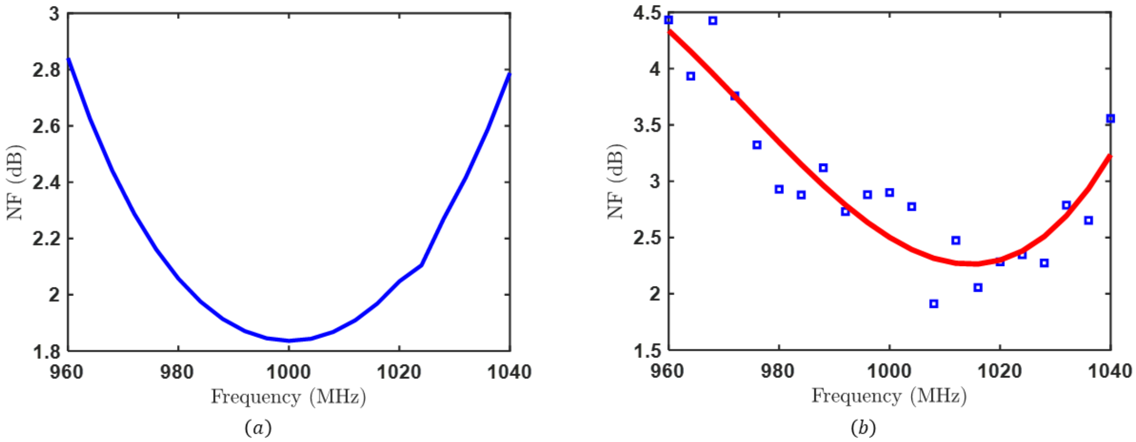

Figure 27: (a) Simulated NF. (b) Measured NF.

Chapter 5: *N*-Way STM-AM Circulators[3]

In this chapter, we introduce the so-called *N*-way implementations of STM-AM circulators, which consist of *N* units of QLTI differential circulators connected either in series or in parallel and exhibiting a particular phase pattern between their modulation signals. We show that these circuits increase the overall power handling by $3\log_2 N$ dB compared to the unit element and suppress the mixing spurs which are not separated from the fundamental harmonic by a multiple of Nf_m.

5.1 THEORY

The analysis of the differential STM-AM circulators presented in Chapter 4 shows that they exhibit QLTI characterestics, at least in theory. This result, however, was found under several assumptions, namely, (i) the involved elements are all linear, (ii) the modulation scheme is exactly sinusoidal, (iii) the constituent single-ended circuits are identical and perfectly balanced, and (iv) all phases are accurately synchronized. In reality, these assumptions are nearly impossible to be satisfied. For instance, if varactors are used to achieve the modulation as in Chapter 3 or Chapter 4, the CV characteristics of such pn junctions are known to be exponentially non-linear, which violates the first assumption. Similarly, switched caps, while they reduce the complexity of the biasing and modulation network as will be explained in more detail in Chapter 7, they still exhibit strong non-linearity due to the switches' non-linear on-resistance and off-capacitance. Furthermore, the capacitance variation of switched caps is quantized which produces finite IMPs of all orders regardless of the elements' linearity. On the other hand, inevitable layout asymmetries, parasitics and random variations in the elements, and phase errors between

---

[3] The content of this chapter is published in [39].

the modulation signals, can easily perturb the differential balance and further contribute to the generation of finite spurs. Lastly, the modulation signals themselves, or their higher-order harmonics resulting from non-linearities, may also leak to any of the circulator's ports, thus contaminating the spectrum even more. These remarks are manifested in Fig. 28, which depicts the simulated spectrums from DC to 2 GHz at the ANT and RX ports of the voltage-mode bandstop/delta topology for a monochromatic TX excitation with an input frequency f_{in} of 1 GHz and an input power P_{in} of 0 dBm. Notice that the same results were presented in Fig. 25 in Chapter 4 but over a much narrower frequency range, i.e., from 750 MHz to 1250 MHz, since the goal therein was to investigate the impact of reducing the second-order IMPs, due to time-variation specifically, on the *S*-parameters and the required modulation frequency. In this chapter, however, the entire spurious emission is of major concern and it must be suppressed below the noise floor, which does not have a considerable impact on the *S*-parameters or the modulation frequency per se, but is crucial to comply with the spectral mask regulations of commercial systems. Fig. 28 shows that the spectrums are indeed contaminated with many spurs, the largest of which are about –21 dBc at f_m and –25 dBc at $3f_m$, where $f_m = 100$ MHz. These are essentially the modulation leakage and its third-order harmonic, respectively. Also, the second-order harmonic at $2f_m$ is –34 dBc. On the other hand, several of the IMPs at $f_{in} \pm kf_m$ are also quite large. Specifically, the second-order spurs at $f_{in} - f_m$ and $f_{in} + f_m$ are –41 dBc and –30 dBc, respectively, the third-order spurs at $f_{in} - 2f_m$ and $f_{in} + 2f_m$ are –30 dBc and –27 dBc, respectively, the fourth-order spurs at $f_{in} - 3f_m$ and $f_{in} + 3f_m$ are –41 dBc and –38 dBc, respectively, and the fifth-order spurs at $f_{in} - 4f_m$ and $f_{in} + 4f_m$ are –41 dBc and –40 dBc, respectively. The rest of the IMPs are all less than –54 dBc and, at the same time, are sufficiently far from the circulator's center frequency $f_{ctr} = f_{in}$, therefore, they can be rejected with filters. Similarly, the modulation leakage and its high-order harmonics can be filtered out. Nevertheless, the necessity of using filters to reject these spurs is in general a drawback as it increases the overall size and cost considerably. Furthermore, the first few IMPs are much more challenging to be filtered out since they are closer to f_{ctr} .

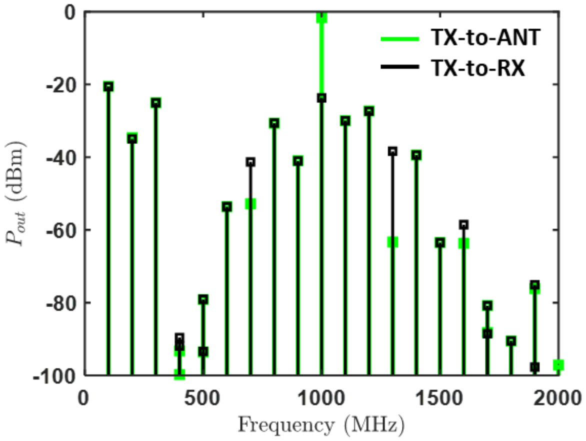

Figure 28: Simulated spurious emission at the ANT and RX ports of a voltage-mode bandstop/delta topology for a monochromatic TX excitation with an input frequency f_{in} of 1 GHz and an input power P_{in} of 0 dBm.

In addition to this strong spurious emission, non-linearities also lead to finite power handling. In fact, all magnetless circulators presented to the date of writing this dissertation are more or less limited to about 1 Watt input power. Quite interestingly, this value was claimed in many previous works based on IL compression solely, which is misleading since IX also compresses as explained in Chapter 3 and Chapter 4, and IX20dB might, in general, be smaller than P1dB. Recall that P1dB and IX20dB were defined in Chapter 3 as the maximum input powers that maintain an IL and IX compression less than 1 dB and 20 dB, respectively. For an accurate description of the circulator’s power handling, we pitch a new benchmark metric so-called Pmax, which is defined as follows

$$\mathrm{Pmax} = \min\left\{\mathrm{P1dB}, \mathrm{IX20dB}\right\} - \mathrm{BO}, \tag{5.1}$$

where BO is an additional back-off power to maintain the mixing spurs below a certain level, lest they saturate the RX frontend even if it is sufficiently isolated from the fundamental haromonic.

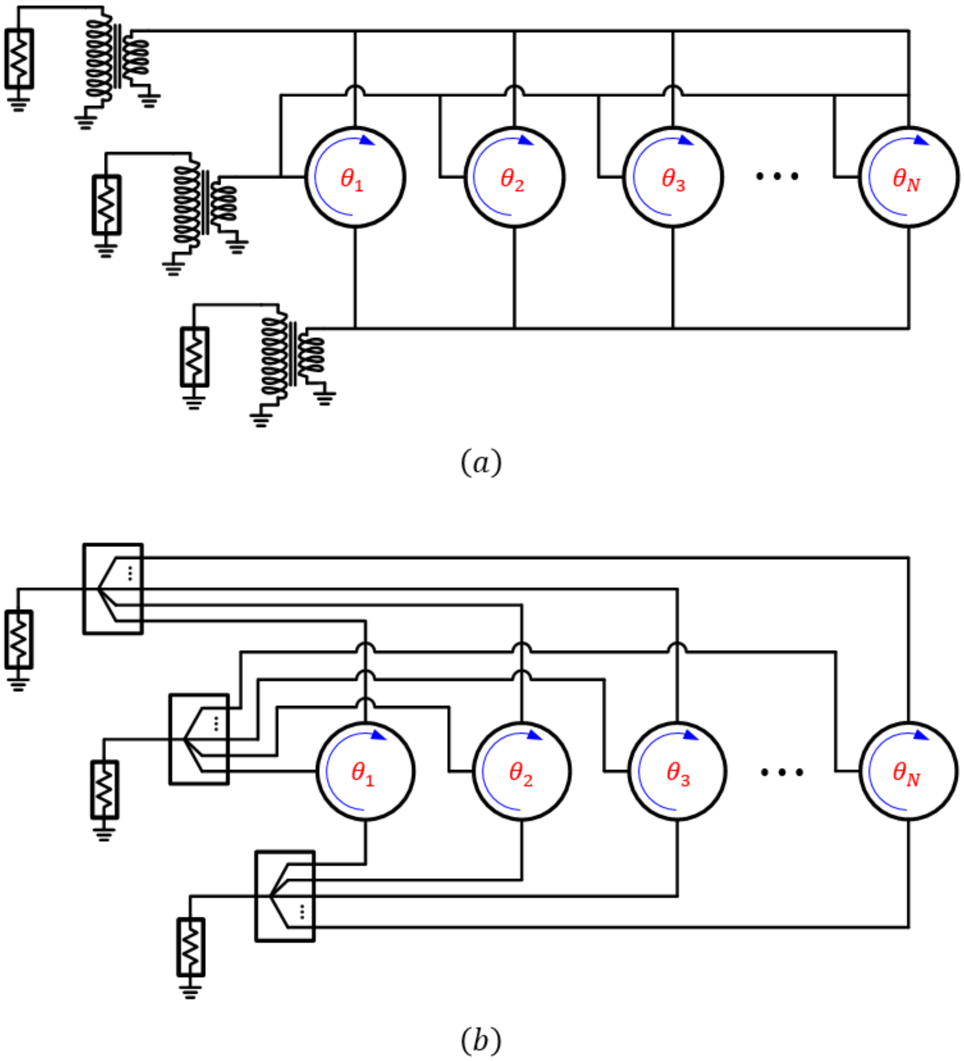

Figure 29: *N*-way STM-AM circulator. (a) Parallel interconnection. (b) Series interconnection.

In order to maximize Pmax and suppress the spurious emission, we introduce herein the so-called *N*-way STM-AM circulators, which consist of *N* circulator units, either connected in parallel or in series as shown in Fig. 29(a) and Fig. 29(b), respectively, and the modulation scheme is as follows

$$C_n = C_0 + \Delta C \cos\left(\omega_m t + (n-1)\frac{2\pi}{3} + (i-1)\frac{2\pi}{N}\right), \tag{5.2}$$

where $i = 1:N$ is the unit index and $n = 1:3$ is the tank index in the *i*-th unit. To simplify the design procedure of such circuits, the unit circulator is assumed to be differential rather than SE. The reason is that the IMPs of the differential circuit are already below a sufficient level, i.e., –30 dBc, which guarantees that the *S*-parameters of all units, when interconnected together, are not perturbed by loading effects. In other words, IMPs of different orders do not interact with each other and the impact of their cancellation on the fundamental harmonic is minimal, hence the overall *S*-parameters of the combined network remain almost identical to those of the unit element. This, in turn, simplifies the design procedure of the *N*-way circuit by allowing to optimize the individual unit element separately. Hence, the operation of the *N*-way circulator can be explained by tracking the individual transmissions through the already-known stages as follows. First, the input power is split amongst *N* paths, either through a transformer followed by a current splitter (which is simply a nodal connection) as in Fig. 29(a), or through a power divider/combiner as in Fig. 29(b). The *N* portions of the input signal are then routed by the identical circulator units in the same direction, while exhibiting the same dispersion. Finally, the signals are summed up again at the output ports. Also, the impedance transformers in Fig. 29(a) have a down conversion ratio of $\sqrt{N}$ in order to match the Z_0 ports to the Z_0/N impedance of the parallel-interconnected units. In Fig. 29(b), however, the units are combined through power dividers/combiners which are already matched at all ports to Z_0, hence impedance transformation is not required. Based on this discussion, we reckon that the overall power handling would increase by $3\log_2 N$ dB. On the other hand, thanks to the phase pattern of (5.2), the IMPs at $kf_{in} \pm lf_m$, where f_{in} and f_m are the input and modulation frequencies, respectively, and k and l are positive integers, would exhibit a phase increment of $l \times (i-1)2\pi/N$ at the *i*-th branch. Therefore, the summation of these products at any port is proportional to $\sum_{i=1}^{N} e^{j[l \times (i-1)2\pi/N]}$, which yields zero for any l that is not a multiple integer of N. In other words, in ideal *N*-way circulators, IMPs occur at an Nf_m interval from f_{in}. In the next section, we present detailed results that validate these remarks.

5.2 RESULTS

In this section, we present a detailed comparison between the results of a 1-way, a 2-way, a 4-way, and an 8-way STM-AM circulator, based on the schematic of Fig. 29(a). The required impedance transformers for $N \neq 1$ are built using a *CLC* π-section of a $\lambda/4$ TL transformer. Also, in all four cases, the unit element is built using the voltage-mode bandstop/delta topology [see Fig. 19(a)], which was experimentally validated in Chapter 4 with excellent agreement between the simulated and measured results of all metrics. Therefore, we reckon that simulations are sufficient to validate the *N*-way circuits in this chapter. It is worth emphasizing that in obtaining the following results, we extracted the layout parasitics using a full-wave simulation and combined them with commercially available full non-linear spice models of all involved elements to perform circuit/EM co-simulations in Keysight ADS. Furthermore, we introduced a random phase error in the phases of (5.2) with a maximum value of ± 5 deg to account for inevitable desynchronization (or dephasing) of the modulation signals in practice.

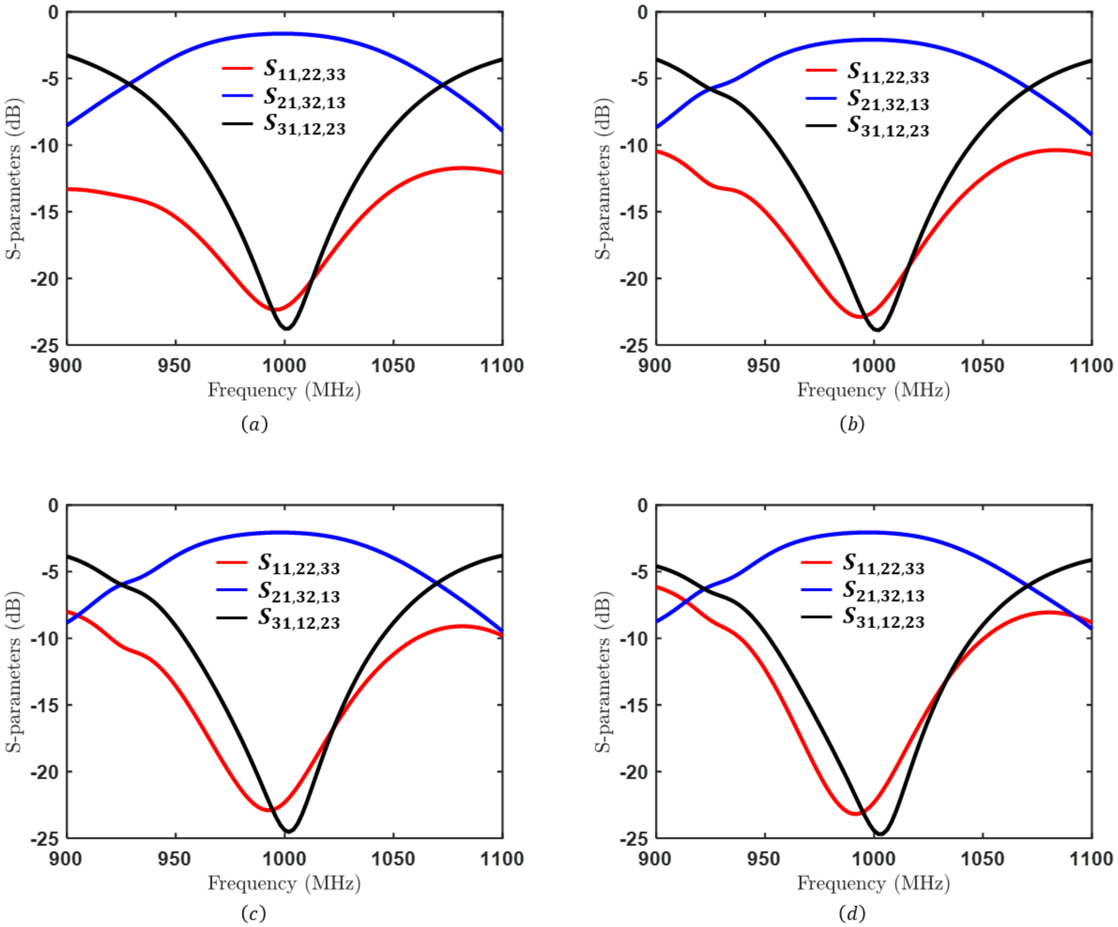

Figure 30: Simulated *S*-parameters. (a) 1-way. (b) 2-way. (c) 4-way. (d) 8-way.

Fig. 30 shows the *S*-parameters of all 1-way, 2-way, 4-way, and 8-way circuits. The IL, RL, and IX of the 1-way circuit at the center frequency f_{ctr} = 1 GHz are 1.7 dB, 22 dB, and 24 dB, respectively. The 2-way, 4-way, 8-way circulators all result in nearly the same values of RL and IX but IL increases to 2 dB at f_{ctr} due to the additional losses incurred by the impedance transformers. Such transformers also change the dispersion of the *S*-parameters, particularly RL and IX, thus increasing the BW from 2.3% (23 MHz) in the 1-way circuit to 2.6% (26 MHz) in the 2-way circuit and finally to 3% (30 MHz) in both the 4-way and 8-way circuits.

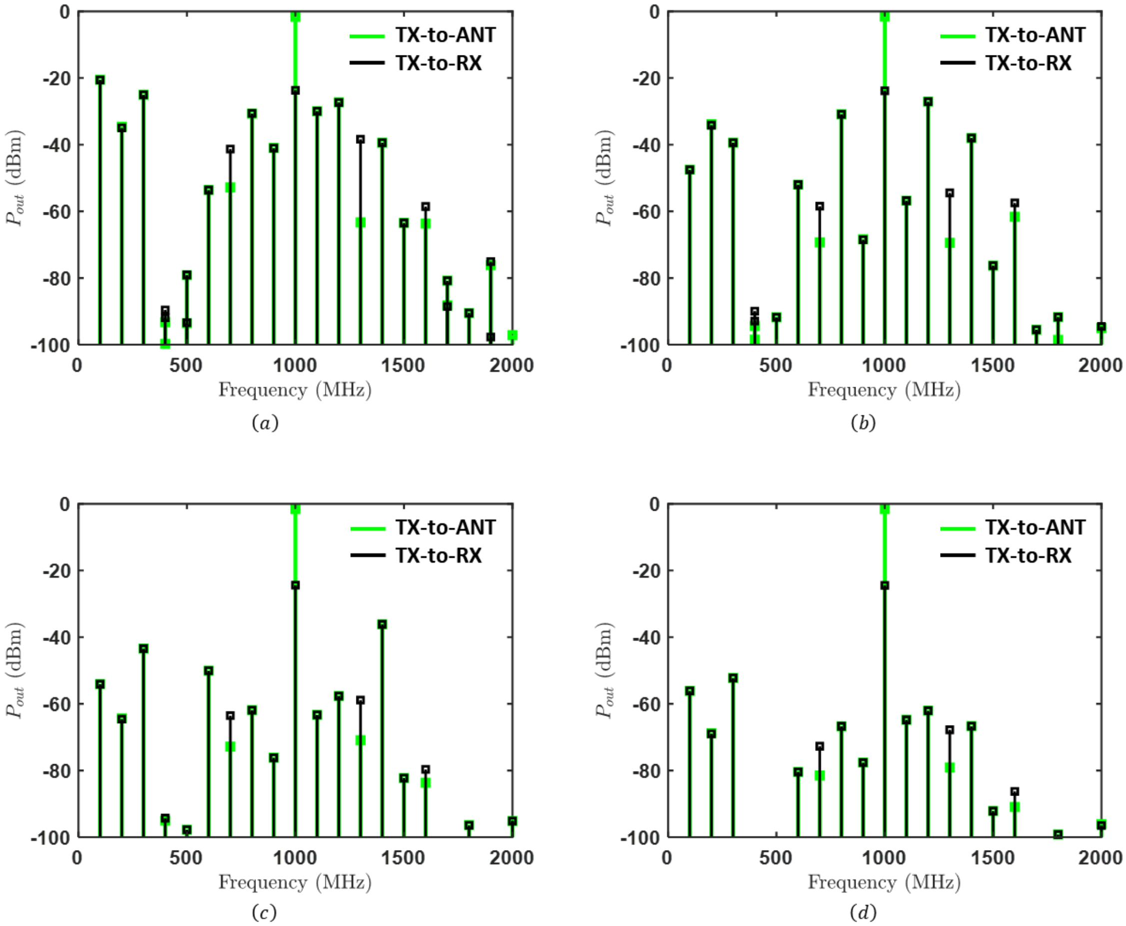

Figure 31: Simulated spurious emission. (a) 1-way. (b) 2-way. (c) 4-way. (d) 8-way.

Fig. 31 also shows the spectrums at both the ANT and RX ports for a monochromatic TX excitation with an input frequency f_{in} of 1 GHz and an input power P_{in} of 0 dBm. As explained in Sec. 5.1, the spectrums of the 1-way circuit, shown again in Fig. 31(a) for convenience, are contaminated with many spurs, either due to the leakage of the modulation signals and their higher-order harmonics or due to their mixing with the input signal resulting in IMPs close to the center frequency f_{ctr}. The 2-way circulator reduces all even-order IMPs, i.e., $f_{in} \pm f_m$, $f_{in} \pm 3f_m$, $f_{in} \pm 5f_m$, ..etc, maintaining them below –55 dBc, as shown in Fig. 31(b), which is about 25 dB improvement compared to the 1-

way circuit. The modulation leakage at f_m is also reduced from –21 dBc to –48 dBc and the third-order harmonic at $3f_m$ is reduced from –25 dBc to –48 dBc. It is worth emphasizing that these improvements are only limited by the inevitable phase errors and layout asymmetries. Should these non-idealities be reduced, the even-order IMPs and the odd-order harmonics of the modulation leakage would all approach the noise floor. Nevertheless, the 2-way circulator does not impact the odd-order IMPs, including the large spurs at $f_{in} \pm 2f_m$, nor the second-order harmonic of the modulation signals at $2f_m$. In fact, these spurs increase by about 1~3 dB compared to the 1-way circuit because of the afotrementioned non-idealities. This problem is solved by the 4-way ciurclator which reduces the IMPs at $f_{in} \pm 2f_m$ to –58 dBc and the second-order harmonic of the modulation signals at $2f_m$ to –65 dBc, as shown in Fig. 31(c). Notice that the IMPs at $f_{in} \pm 4f_m$ are almost not affected, as expected. These spurs can be suppressed by the 8-way circulator which maintains all IMPs and modulation leakage spurs below –60 dBc and –50 dBc, respectively, as shown in Fig. 31(d). As one may expect, a 16-way circulator would clean the spectrums even further, but this comes at the expense of increasing the overall size and the power consumed in generating the modulation signals considerably, therefore an 8-way circulator is arguably the optimal choice in reality. Also, as mentioned earlier, the performance of an *N*-way circulator, for a given *N*, would automatically improve if the layout symmetry is enhanced and the phase relation of (5.2) is tightly enforced.

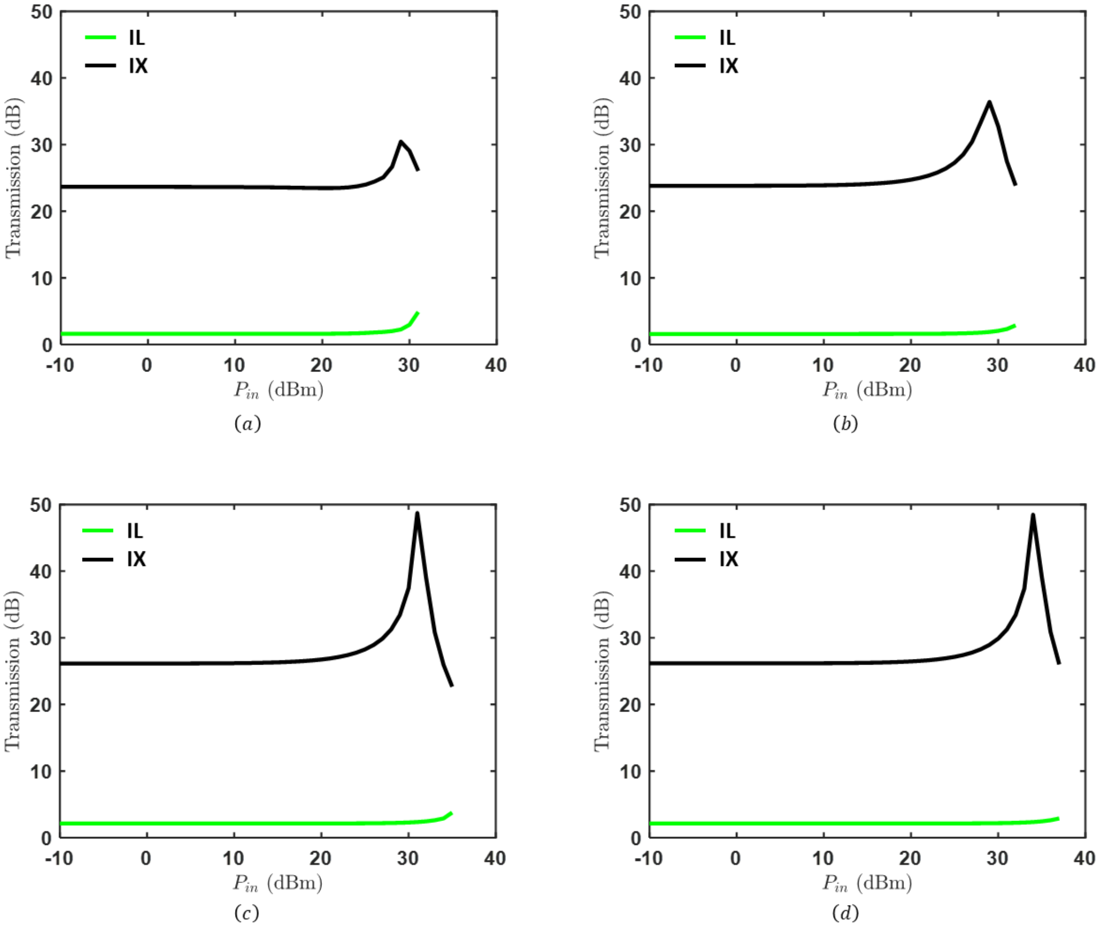

Figure 32: Simulated P1dB and IX20dB. (a) 1-way. (b) 2-way. (c) 4-way. (d) 8-way.

Fig. 32 shows the IL and IX versus the input power P_{in}. Based on the definition of Pmax pitched in (5.1) and neglecting BO, the 1-way, 2-way, 4-way, and 8-way circulators result in Pmax of +30 dBm, +33 dBm, +36 dBm, and +39 dBm, respectively. Notice that the assumption of zero BO is exact in the 4-way and 8-way circuits, since the spurious emission is drastically reduced, hence there is no need for any backoff in these cases. As expected, Pmax increases by +3 dB for each doubling of the unit elements.

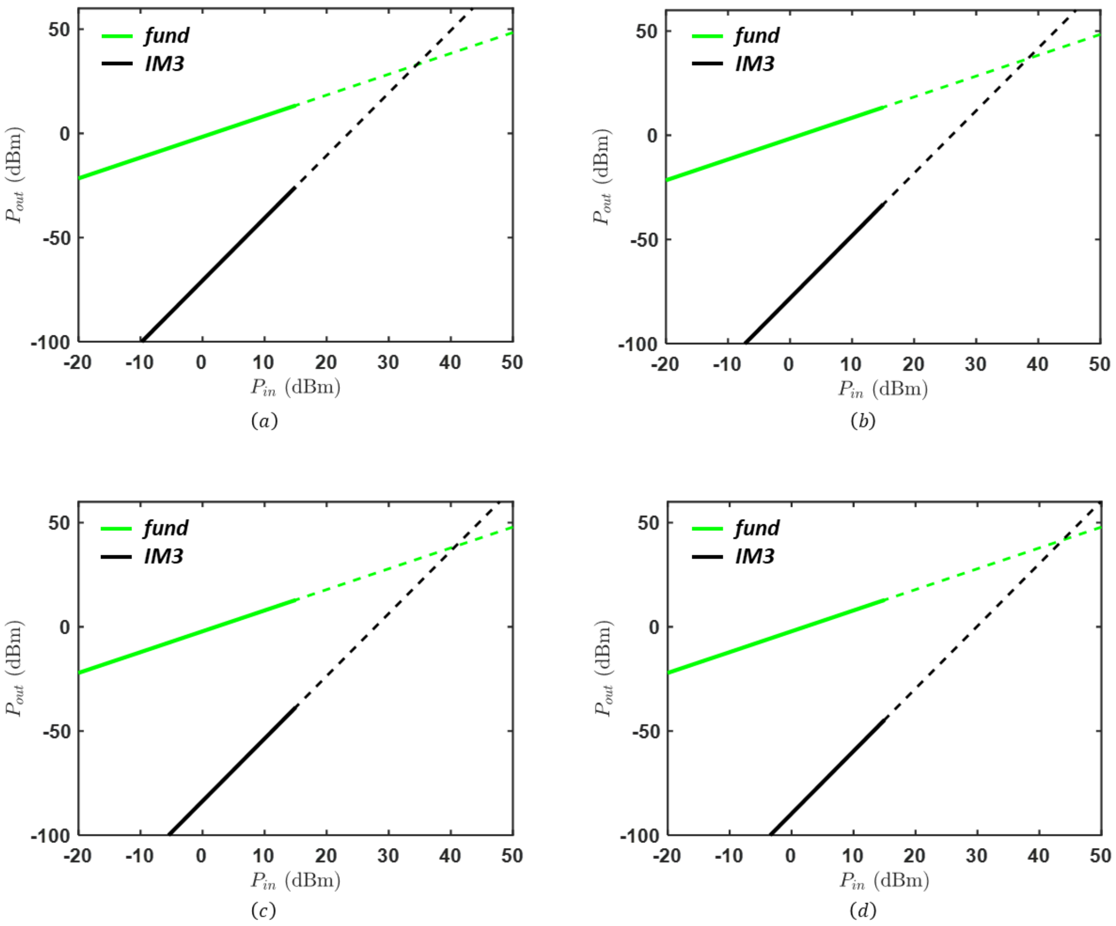

Figure 33: Simulated IIP3. (a) 1-way. (b) 2-way. (c) 4-way. (d) 8-way.

Fig. 33 also shows the output power at the ANT port for a two-tone excitation at the TX port, each at 0 dBm and separated by 1 MHz. The IIP3 achieved by the 1-way, 2-way, 4-way, and 8-way circulators are +34 dBm, +37 dBm, +40 dBm, +43 dBm, respectively.

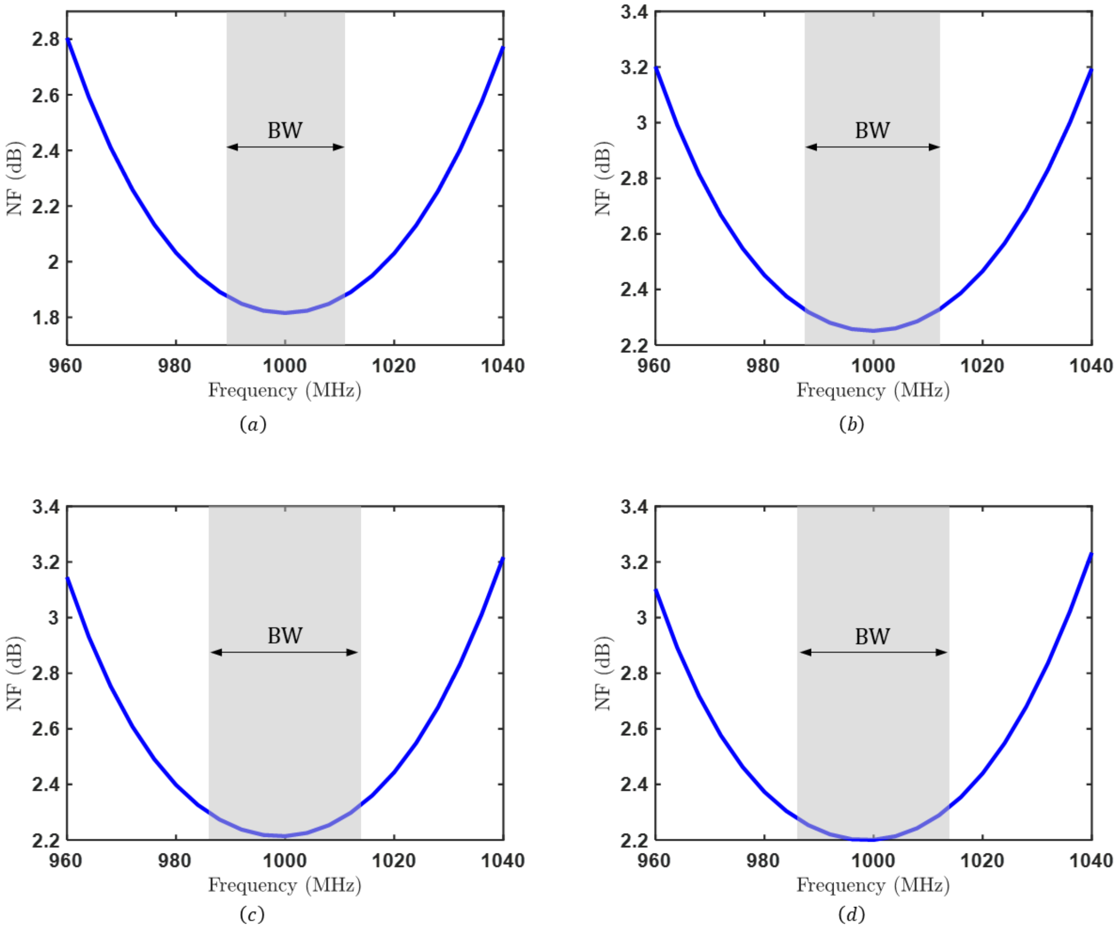

(a) (b) (c) (d)

Figure 34: Simulated NF. (a) 1-way. (b) 2-way. (c) 4-way. (d) 8-way.

Finally, Fig. 34 shows the RX NF. The minimum NF of the 1-way circulator, at the center frequency of 1 GHz, is 1.8 dB and it increases to 1.9 dB at the edges of the 2.3% bandwidth (highlighted in grey). On the other hand, the 2-way circuit results in a minimum NF of 2.25 dB at 1 GHz and it increases to 2.35 dB at the edges of the 2.6% bandwidth. Also, the 4-way and 8-way circulators both result in a minimum NF of 2.2 dB at 1 GHz and it increases to 2.3 dB at the edges of the 3% bandwidth. Similar to the IL, NF of the 2-way, 4-way and 8-way circuits is larger than that of the 1-way circuit because of the additional losses incurred by the impedance transformers. Also, NF of the 4-way and 8-way circulators results is identical to the IL, thanks to the drastic reduction of the IMPs which, in turn, reduces the noise folding into the fundamental bandwidth. For convenience, the previous results are all summarized in Table 3.

Metric\Circulator	1-way	2-way	4-way	8-way
Cent. freq. (MHz)	1000	1000	1000	1000
Mod. freq. (%)	10	10	10	10
BW (%)	2.3	2.6	3	3
IX (dB)	>20	>20	>20	>20
IL (dB)	<1.8	<2.3	<2.3	<2.3
RL (dB)	>20	>20	>20	>20
P1dB (dBm)	+30	+33	+36	+39
IX20dB (dBm)	+32	+35	+38	+41
IIP3 (dBm)	+34	+37	+40	+43
NF (dB)	<2.35	<2.33	<2.3	<2.3
IMPs (dBc)	–27 @ $f_0 \pm 2f_m$	–27 @ $f_0 + 2f_m$	–36 @ $f_0 + 4f_m$	<–62
	–30 @ $f_0 - 2f_m$ & $f_0 + f_m$	–31 @ $f_0 - 2f_m$	–50 @ $f_0 - 4f_m$	
Mod. leakage (dBc)	–21 @ f_m	–34 @ $2f_m$	–44 @ $3f_m$	–52 @ $3f_m$
	–25 @ $3f_m$	–40 @ $3f_m$	–54 @ f_m	–56 @ f_m
	–35 @ $2f_m$	–47 @ f_m	–65 @ $2f_m$	–69 @ $2f_m$

Table 3: Comparison between the simulated results of 1-way, 2-way, 4-way, and 8-way STM-AM circulators.

Chapter 6: Broadband STM-AM Circulators[4]

In this chapter, we derive a theoretical bound on the BW of STM-AM circulators for a given modulation frequency, and present a technique to approach this bound using passive matching networks. We validate the analysis with simulated and measured results, depicting a wide BW of 140 MHz at a center frequency of 1 GHz and using a modulation frequency of 100 MHz.

6.1 THEORY

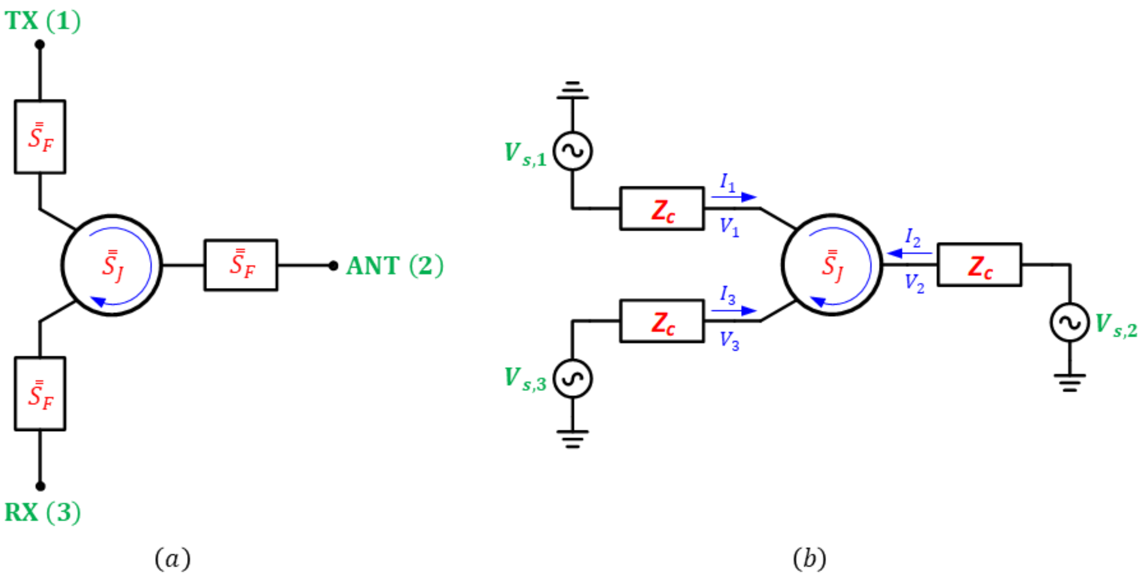

Figure 35: (a) Generic block diagram of an STM-AM circulator connected to the 50 Ohm TX, ANT, and RX ports through identical two-port passive networks. (b) Replacing the two-port networks and the 50 Ohm ports with their Thevenin's equivalent impedances and sources.

---

[4] The content of this chapter is published in [40].

Based on the results presented in previous chapters, one can predict that the instantaneous BW of STM-AM circulators, either single-ended or differential, is limited by the modulation frequency f_m, the loaded quality factor Q_l of the resonant junction, and the order of the constituent resonators. For example, first-order resonators, i.e., series or parallel *LC* tanks, with 10~20% modulation frequency and 50 Ohm termination led to a BW of about 3~4% at best. One solution to improve this further is to increase f_m but this would increase power consumption, prohibit the use of thick-oxide low-speed technologies that could handle high power, and complicate scaling the center frequency to the mm-wave bands and beyond. Therefore, it is in general desirable to keep f_m relatively small and adopt another approach to increase the BW. For example, transformers can be used to change the port impedances such that the loaded quality factor of the resonant junction is reduced and, consequently, the BW is broadened. However, parametric studies show that the required modulation amplitude in this case must increase considerably in order to lift the degeneracy of the rotating modes, which, in turn, increases power consumption and complicates the generation of the modulation signals themselves, especially in multi-phases. Alternatively, one could increase the order of the constituent resonators so that the junction supports more modes (two degenerate modes at each pole) which, consequently, can be designed to provide IX over a wider BW. While this is indeed a viable option, the main challenge is that it increases the circuit's complexity and size considerably. Furthermore, none of all these approaches guarantees that the maximum possible BW for given values of f_m and Q_l and a particular order of the junction's resonance is achieved. In order to find the optimal solution, we must derive first a global bound on the maximum possible BW as a function of the constituent elements and parameters. This, in turn, will give us an insight into the optimal technique to approach this bound, as we demonstrate next.

6.2 ANALYSIS

6.2.1 NARROWBAND JUNCTION

Fig. 35(a) shows a generic block diagram of an STM-AM circulator connected to the 50 Ohm TX, ANT, and RX ports through identical two-port passive networks. Notice that the passivity assumption of the two-port network is essential to allow signal flow in opposite directions at the ANT terminal, i.e., TX-to-ANT and ANT-to-RX. Using Thevinin's equivalence, the circuit can be redrawn as shown in Fig. 35(b) where the two port networks and the 50 Ohm ports are replaced by the equivalent voltage sources $\bar{V}_s = \{V_{s,1}, V_{s,2}, V_{s,3}\}$ and the characteristic impedance $Z_c = 1/Y_c$ which is generally complex and frequency dispersive. The circulator is also presumed IM-free such that its *S*-parameters are not perturbed by loading effects regardless of the circuit implementation of the two-port network. In other words, the junction must, in general, be an *N*-way circulator. Recall that in such circuits, the unit element was presumed differential for similar reasons. In this case, the junction becomes LTI and it can be characterized independently of its port terminations using, for example, the *Y*-parameters, which can be calculated as follows

$$\bar{\bar{Y}}_J = Y_0 \left(\bar{\bar{U}} + \bar{\bar{S}}_J\right)^{-1} \left(\bar{\bar{U}} - \bar{\bar{S}}_J\right) = \begin{bmatrix} Y_{11} & Y_{31} & Y_{21} \\ Y_{21} & Y_{11} & Y_{31} \\ Y_{31} & Y_{21} & Y_{11} \end{bmatrix}, \tag{6.1}$$

where $Y_0 = 1/Z_0$, $\bar{\bar{U}}$ is the unitary matrix, and $\bar{\bar{S}}_J$ is the *S*-matrix of the junction. Notice that both the *S*- and *Y*-matrices are cyclic-symmetric thanks to the three-fold symmetry of STM-AM circulators. Using Kirchhoff's laws, the port voltages $\bar{V} = \{V_1, V_2, V_3\}$ depicted in Fig. 35(b) can be related to the voltage sources $\bar{V}_s$ as follows

$$\bar{V} = \left(\bar{\bar{U}} + Z_c \bar{\bar{Y}}_J\right)^{-1} \bar{V}_s. \tag{6.2}$$

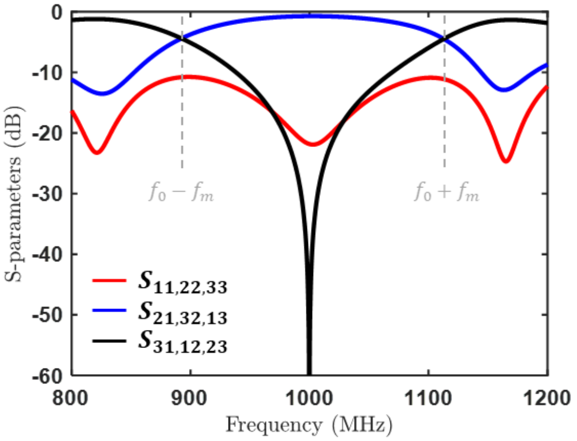

Figure 36: Analytical *S*-parameters of a current-mode bandpass/wye junction based on the values provided in Table 4.

Substituting (6.1) into (6.2) and assuming that only port 1 is excited, i.e., $\bar{V}_s = \left\{V_{s,1}, 0, 0\right\}$, yields

$$\frac{V_1}{V_{s,1}} = Y_c \frac{\left(Y_c + Y_{11}\right)^2 - Y_{21}Y_{31}}{\left\|\bar{\bar{Y}}\right\| + Y_c^3 + 3Y_{11}Y_c^2 + 3\left(Y_{11}^2 - Y_{21}Y_{31}\right)Y_c} \tag{6.3}$$

$$\frac{V_2}{V_{s,1}} = Y_c \frac{Y_{31}^2 - \left(Y_c + Y_{11}\right)Y_{21}}{\left\|\bar{\bar{Y}}\right\| + Y_c^3 + 3Y_{11}Y_c^2 + 3\left(Y_{11}^2 - Y_{21}Y_{31}\right)Y_c} \tag{6.4}$$

$$\frac{V_3}{V_{s,1}} = Y_c \frac{Y_{21}^2 - \left(Y_c + Y_{11}\right)Y_{31}}{\left\|\bar{\bar{Y}}\right\| + Y_c^3 + 3Y_{11}Y_c^2 + 3\left(Y_{11}^2 - Y_{21}Y_{31}\right)Y_c}, \tag{6.5}$$

where $\left\|\bar{\bar{Y}}\right\| = Y_{11}^3 + Y_{21}^3 + Y_{31}^3 - 3Y_{11}Y_{21}Y_{31}$. For proper operation of the circulator, IX of the combined network is required to be larger than 20 dB at least, therefore we can assume $V_3 \approx 0$, then (6.5) yields

$$Y_c = \frac{Y_{21}^2}{Y_{31}} - Y_{11}. \tag{6.6}$$

Equation (6.6) gives the theoretical port termination needed to maintain an infinite IX by the combined network at all frequencies. Obviously, this is not physically possible for it violates causality. Therefore, (6.6) can be synthesized only over a limited frequency range around the junction's center frequency f_{ctr}. In fact, since $\boldsymbol{Y}_c$ must be passive as explained earlier, one can expect this limitation is essentially due to its real part becoming negative beyond a certain BW. To investigate this hypothesis, let us consider an example where the junction is realized using the current-mode bandpass/wye topology (see Appendix B). Notice that this is essentially an *N*-way circulator with $N=1$, therefore the LTI assumption is preserved. Using the values of all elements and modulation parameters summarized in Table 4 and the analytical results of the current-mode bandpass/wye topology provided in Appendix B, the *S*-parameters of such circuit are depicted in Fig. 36. The center frequency f_{ctr} in this example is 1 GHz and the instantaneous BW of the junction is 4%. Also, IL, RL, and IX at f_{ctr} are 0.74 dB, 22 dB, and 60 dB, respectively. The *Y*-matrix of such junction can be found using (6.1), then the characteristic admittance $\boldsymbol{Y}_c$ can be calculated using (6.6), which yields the results shown in Fig. 37. At the center frequency f_{ctr}, $\boldsymbol{Y}_c$ is almost real and equal to $\boldsymbol{Y}_0$. Recall that $\boldsymbol{Y}_c$ is the required termination to achieve infinite IX at all frequencies, and since its value at f_{ctr} is already satisfied by the 50 Ohm ports themselves, then IX indeed becomes infinite at f_{ctr}. At other frequencies, however, $\boldsymbol{Y}_c$ is not equal to Y_0, hence the IX decreases. Interestingly, the real part of Y_c becomes negative at $f_{ctr} \pm f_m$, as we initially expected. The same result can be obtained for any other implementation of the junction, therefore the BW of STM-AM circulators is in general limited to $2f_m$, i.e.,

$$\mathrm{BW} < 2f_m. \tag{6.7}$$

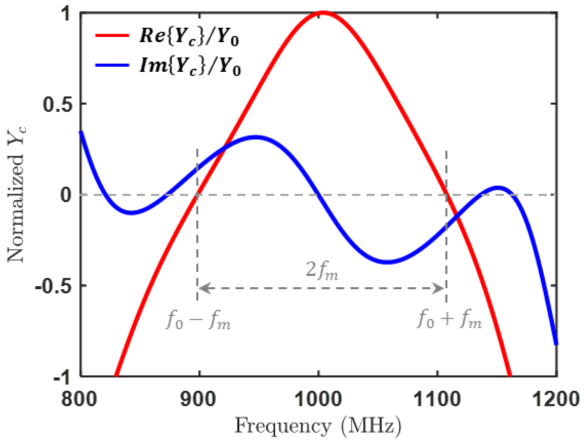

Figure 37: Normalized real and imaginary parts of the characteristic admittance Y_c versus frequency.

Fig. 37 also shows that the imaginary part of Y_c is non-foster, i.e., its slope is negative, within the BW limit of (6.7). Since the synthesis of non-foster impedances using passive elements can only be achieved approximately and over a limited frequency range, one would expect that there is another restriction on the BW. In order to find such limit, we first need to calculate the input admittance Y_{in} at any of its terminals, say terminal 1, when the other two terminals, terminals 2 and 3, are terminated with Y_c. From the definition of the Y-matrix itself, the current at terminal 1 is given by

$$I_1 = Y_{11}V_1 + Y_{21}V_1 + Y_{31}V_3 \,. \tag{6.8}$$

Recalling that $V_3 \approx 0$, then Y_{in} can be calculated as follows

$$Y_{in} = \frac{I_1}{V_1} = Y_{11} + \frac{V_2}{V_1} \,. \tag{6.9}$$

Substituting (6.6) into (6.3) and (6.4) also yields $V_2/V_1 = -Y_{31}^2/Y_{21}$. Therefore, (6.9) reduces to

$$Y_{in} = \frac{I_1}{V_1} = Y_{11} - \frac{Y_{31}^2}{Y_{21}}. \tag{6.10}$$

Furthermore, since the junction is passive and LTI, then

$$\sum_{n=1}^{N} P_n \geq 0, \tag{6.11}$$

where *n* is the port index and P_n is the input power at the *n*-th port. Equation (6.11) can be rewritten in a matrix form as follows

$$\mathrm{Re}\left\{\overline{V}^{\dagger}\overline{I}\right\} \geq 0, \tag{6.12}$$

where $\overline{V} = \{V_1, V_2, V_3\}$ and $\overline{I} = \{I_1, I_2, I_3\}$ are the vectors of the voltages and currents at the junction's terminals, respectively, and $\dagger$ is the conjugate transpose operator. Substituting for $\overline{I} = \overline{\overline{Y}}\overline{V}$ into (6.12) and assuming a lossless and cyclic-symmetric junction, then (6.12) simplifies to

$$Y_{11} + Y_{11}^* = 0 \tag{6.13}$$

$$Y_{21} + Y_{31}^* = 0. \tag{6.14}$$

Substituting (6.13) and (6.14) into (6.10) results in

$$Y_{in} = -Y_{11}^* + \frac{\left(Y_{21}^*\right)^2}{Y_{31}^*} = Y_c^*. \tag{6.15}$$

6.2.2 MATCHING FILTERS

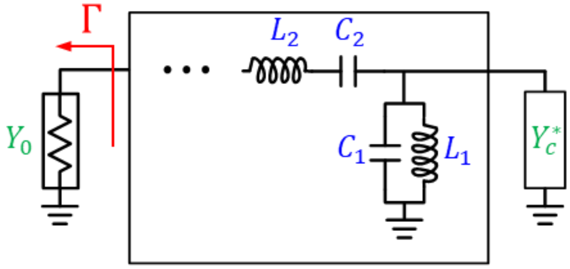

Figure 38: Synthesis of the two-port network in Fig. 37(a) using an *LC* bandpass filter loaded with an admittance Y_c^* and designed to minimize the reflection coefficient Γ from a 50 Ohm source.

Equation (6.15) implies that broadening the BW of a narrowband non-reciprocal junction is essentially a conjugate matching problem. In other words, the synthesis of Z_c is exactly the same as matching a source with an impedance Z_0 to a load with an impedance Z_c^*, as depicted in Fig. 38. If the losses of the matching network are neglected, then matching the output impedance to the load is equivalent to matching the input impedance to the 50 Ohm source, or equivalently, minimizing the input reflection coefficient Γ. Furthermore, since the load impedance Z_c^* is resonant at a center frequency f_{ctr} [see Fig. 37], then the matching circuit can be designed using an *LC* bandpass filter, also centered at f_{ctr}. From conventional filter theory, it is well known that the BW of bandpass filters is bounded by the Bode-Fano criterion, i.e., Γ can be maintained below a certain threshold only over a limited frequency range. To find such limit, a circuit model for the admittance Y_c^* is required. By inspection of Fig. 37, a first-order model can be constructed using a simple series *RLC* tank, where the values of its elements are given by

$$R_c = \left|Z_c\right|_{\omega=\omega_{ctr}} \tag{6.16}$$

$$L_c = 0.5\left|\frac{dZ_c}{d\omega}\right|_{\omega=\omega_{ctr}} \tag{6.17}$$

$$C_c = \frac{1}{\omega_{ctr}^2 L_c}. \tag{6.18}$$

The Bode-Fano criterion then requires

$$\int_0^\infty \ln\left(\frac{1}{|\Gamma|}\right) d\omega \le \frac{\pi R_c}{L_c}. \tag{6.19}$$

Notice that the circulator’s RL is also related to Γ as follows

$$\mathrm{RL} = -20\log_{10}\left(|\Gamma|\right). \tag{6.20}$$

For an IL less than α and an IX larger than β, power conservation requires

$$\mathrm{RL} > \rho = -20\log_{10}\left(1-10^{-\beta/20}-10^{-\alpha/20}\right), \tag{6.21}$$

where power dissipation was neglected for simplicity. For $\alpha = 3$ dB and $\beta = 20$ dB, a simple substitution in (6.21) yields $\rho = 14.33$ dB. Assuming brickwall matching with a constant reflection coefficient ρ inside the BW and unity elsewhere, then (6.19) yields

$$\mathrm{BW} \le \frac{\pi}{\ln(1/\rho)}\frac{f_{ctr}}{Q_c}, \tag{6.22}$$

where $Q_c = \frac{1}{\omega_{ctr} R_c C_c} = \frac{\omega_{ctr} L_c}{R_c}$. From (6.7) and (6.22), we get

$$\mathrm{BW} < \min\left\{\frac{\pi}{\ln(1/\rho)}\frac{f_{ctr}}{Q_c}, 2f_m\right\}. \tag{6.23}$$

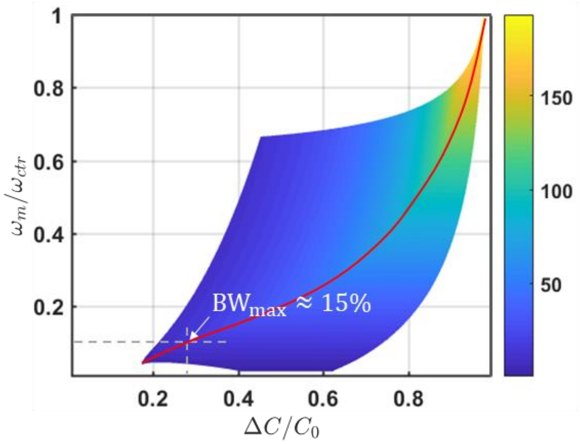

Figure 39: Maximum BW of the STM-AM circulator versus the modulation parameters f_m/f_0 and $\Delta C/C_0$ based on (6.23).

Equation (6.23) provides a global bound on the BW of STM-AM circulators. For the special case under consideration where the junction is designed based on the current-mode bandpass/wye topology, Fig. 39 shows the impact of changing the modulation parameters on this bound. The colorful portion of the figure depicts the possible combinations of f_m/f_0 and $\Delta C/C_0$ that could achieve an overall IX larger than 20 dB and a total IL less than 3 dB. Other combinations, however, as depicted by the white region cannot meet these specifications, hence the BW in this case is not defined. Within the valid range, there is also an optimal one-to-one mapping between the modulation parameters that maximizes the BW, as indicated by the red line. As an example, for $f_m/f_0 = 11\%$, the optimal $\Delta C/C_0$ is 0.28 and the maximum possible BW is about 15%. In order to approach this limit without increasing the overall IL considerably, the order of the bandpass filters should be kept small (<3 in practice). Assuming a second-order filter and initially ignoring losses to simplify the design, the input impedance Z_{in} seen by the 50 Ohm ports in Fig. 38 can be calculated as follows

$$Z_{in} = Z_2 + \frac{1}{Y_1 + Y_c^*}, \tag{6.24}$$

where

$$Y_1 = j\left(\omega C_1 - \frac{1}{\omega L_1}\right) \tag{6.25}$$

$$Z_2 = j\left(\omega L_2 - \frac{1}{\omega C_2}\right), \tag{6.26}$$

and L_k and C_k are the inductance and capacitance of the ladder's *k*-th branch, respectively, where $k = 1$ at the side of Y_c^*. Assuming a Chebyshev response, since it gives larger BW than Butterworth's while Elliptic and other responses are not worth the additional complications as noted by Fano himself, then the filter elements can be calculated by enforcing the impedance conditions

$$Z_{in}\left(f_c \pm \delta f/2\right) = Z_0, \tag{6.27}$$

where $f_c = f|_{\mathrm{Re}\{Y_c\}=0} \approx f_0$ is the resonant frequency of Y_c and δf is chosen numerically to maximize the circulator's BW and approach the bound given by (6.23).

6.2.3 COMBINED NETWORK

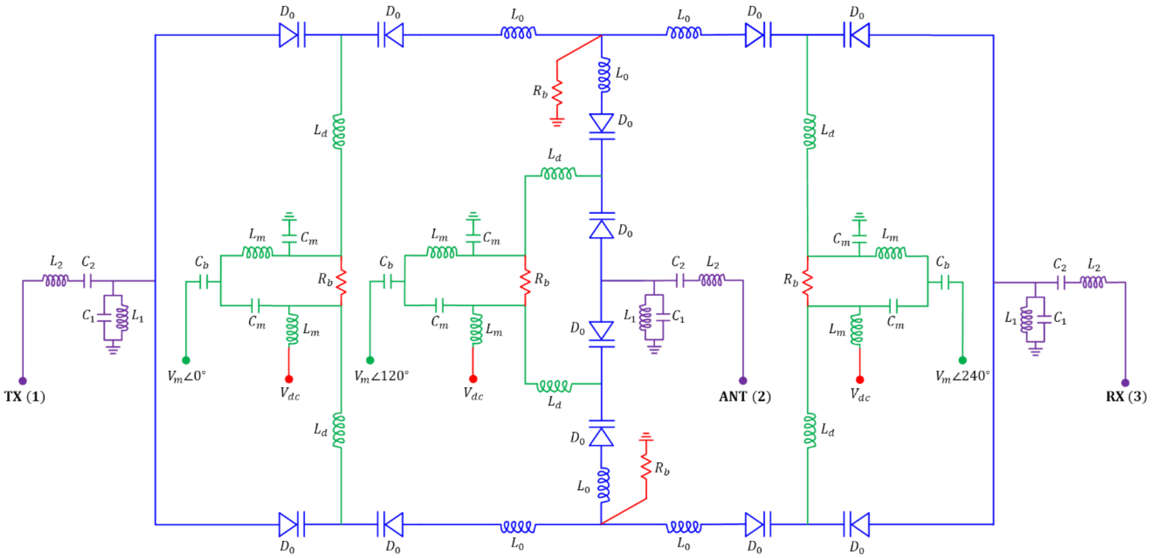

Figure 40: Complete schematic of a broadband STM-AM circulator based on a current-mode bandpass/wye circuit and second-order matching filters.

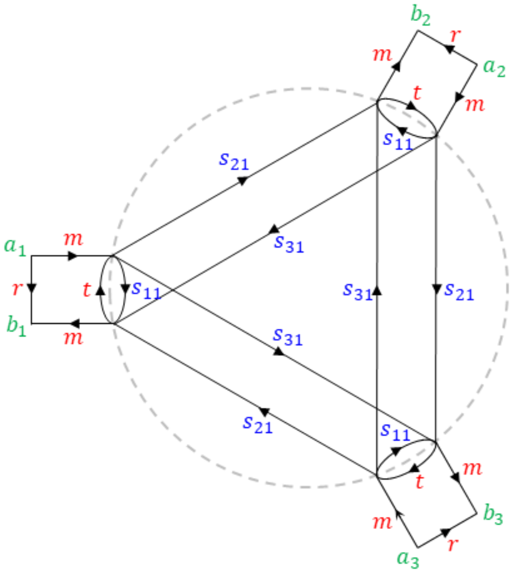

Figure 41: Signal-flow graph of the broadband STM-AM circulator shown in Fig. 35(a).

Element\Value		Theo.		Sim.	Meas.
Main circuit	f_{ctr} (MHz)	1000		1000	1000
	f_m/f_{ctr} (%)	11		11	11
	L_0 (nH)	25	$Q_0 = 70$	24 (Coilcraft)	24 (Coilcraft)
	C_0 (pF)	1.2		SMV2022 (Skyworks)	SMV2022 (Skyworks)
	$\Delta C/C_0$ (%)	54.4			
Filters	L_1 (nH)	1.76		2.4 (Coilcraft)	2.4 (Coilcraft)
	C_1 (pF)	15.6		7.8 (Murata)	7.8 (Murata)
	L_2 (nH)	10.4		11 (Coilcraft)	11 (Coilcraft)
	C_2 (pF)	3.9		2.5 (Murata)	2.5 (Murata)
Modulation network	V_m (Vpp)	N/R		6.2	6.2
	L_d (nH)	N/R		68 (Coilcraft)	68 (Coilcraft)
	L_m (nH)	N/R		220 (Coilcraft)	220 (Coilcraft)
	C_m (pF)	N/R		5 (Coilcraft)	5 (Murata)
DC bias network	V_{dc} (Volt)	N/R		8	8
	R_b (KOhm)	N/R		100 (KOA)	100 (KOA)
	C_b (pF)	N/R		1000 (Murata)	1000 (Murata)

Table 4: Values of all design parameters used in obtaining the theoretical, simulated, and measured results of the broadband current-mode bandpass/wye STM-AM circulator.

As an example, we rely on the analytical expression in previous Sections to design a broadband circulator at 1 GHz. Fig. 40 shows the complete schematic of the circuit and the values of all elements are summarized in Table 4. The *S*-parameters can be calculated using signal-flow graph analysis as depicted in Fig. 41, where a_n and b_n are the incident and reflected wave amplitudes at the *n*-th port, respectively, s_{11}, s_{21}, s_{31} are the *S*-parameters of the junction, and r, t, and m are the *S*-parameters of the matching filters which are given by

$$r = 1 - \frac{2Z_0\left(Y_0 + Y_1\right)}{1 + \left(Y_0 + Y_1\right)\left(Z_0 + Z_2\right)} \tag{6.28}$$

$$t = 1 - 2Z_0 \frac{1 + Y_1\left(Z_0 + Z_2\right)}{2Z_0 + Z_2 + Z_0 Y_1\left(Z_0 + Z_2\right)} \tag{6.29}$$

$$m = \frac{2}{1 + \left(Y_0 + Y_1\right)\left(Z_0 + Z_2\right)} . \tag{6.30}$$

Using Mason's gain formula, the *S*-parameters of the combined network can be calculated as follows

$$S_{11} = S_{22} = S_{33} = r + \frac{\Delta_1}{\Delta} m^2 s_{11} + \frac{2}{\Delta} m^2 s_{21} s_{31} t\left(1 - s_{11} t\right) + \frac{1}{\Delta} m^2 s_{21}^3 t^2 \tag{6.31}$$

$$S_{21} = S_{32} = S_{13} = \frac{1}{\Delta} m^2 \left[s_{21}\left(1 - s_{11} t\right) + s_{31}^2 t \right] \tag{6.32}$$

$$S_{31} = S_{12} = S_{23} = \frac{1}{\Delta} m^2 \left[s_{31}\left(1 - s_{11} t\right) + s_{21}^2 t \right] , \tag{6.33}$$

where

$$\Delta_1 = 1 + s_{11}^2 t^2 - \left(2 s_{11} t + s_{21} s_{31} t^2\right) \tag{6.34}$$

$$\Delta = 1 - s_{11}^3 t^3 + \left(3 s_{11}^2 t^2 + 3 s_{11} s_{21} s_{31} t^3\right) - \left(3 s_{11} t + 3 s_{21} s_{31} t^2 + s_{21}^3 t^3\right) . \tag{6.35}$$

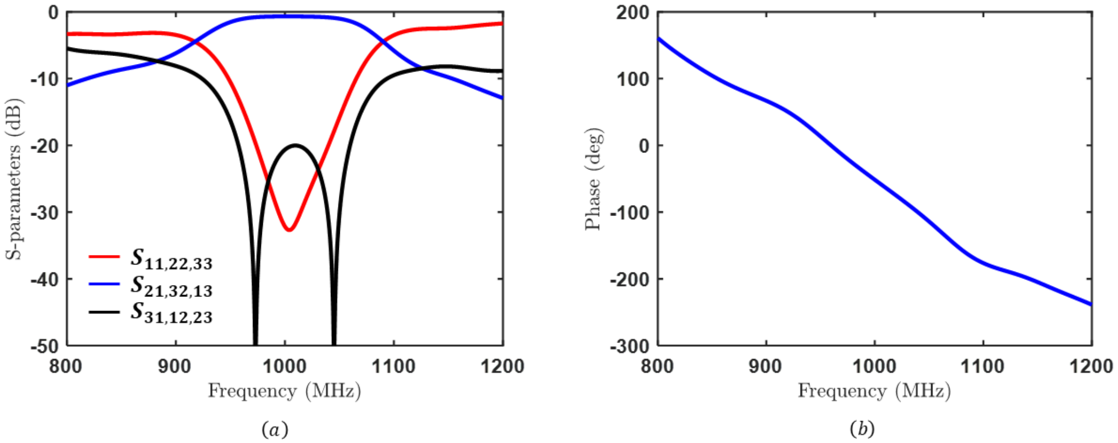

Figure 42: Analytical *S*-parameters of the broadband STM-AM circulator based on the design parameters provided in Table 4. (a) Magnitude. (b) Phase.

Based on these results, Fig. 42 shows the analytical *S*-parameters of the circuit in Fig. 40. Clearly, the IX follows a second-order Chebyshev response as expected with two notches at 972 MHz and 1045 MHz and an in-band ripple less than 20 dB. Furthermore, the achieved BW is 11% which is about 2.5 times larger than the narrowband junction's 4% and at least 4.5 times larger than the results reported in previous chapters. This value can be improved further, approaching the limit of 15% predicted from Fig. 39, by relaxing the conditions in (6.27) and not necessarily requiring IX to be infinite at any in-band frequency, as long as it is still larger than 20 dB. This will be demonstrated through simulations in the next section while taking into account the neglected dissipation and parasitics of all elements.

6.3 RESULTS

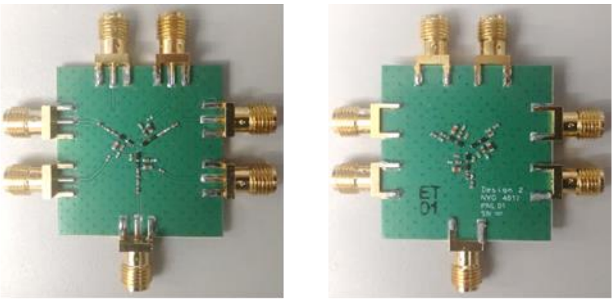

(a) (b)

Figure 43: Photograph of the fabricated broadband STM-AM circulator. (a) Top side. (b) Bottom side.

Thus far, the filters' dissipation was neglected. In practice, this nuisance not only degrades IL, but it also distorts the filter characteristics, hence the synthesized IX dispersion is perturbed. In order to account for these effects, circuit/EM co-simulations were performed in Keysight ADS while tweaking the design parameters to compensate for all parasitic effects, thus resulting in the final values summarized in Table 4. Fig. 43 shows a photograph of the fabricated board and the measured results were taken using the same experimental setups in Appendix A.

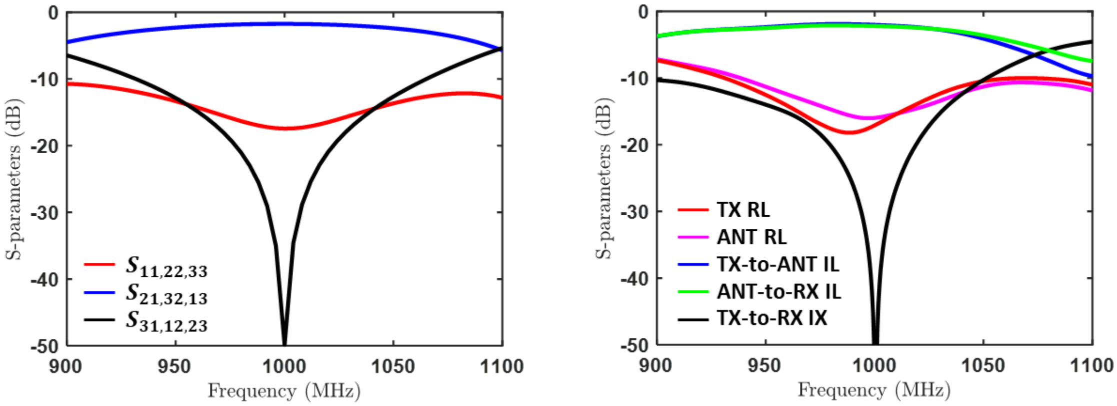

(a) (b)

Figure 44: *S*-parameters of the narrowband junction. (a) Simulated. (b) Measured.

Fig. 44(a) and Fig. 44(b) show the simulated and measured *S*-parameters, respectively, of the narrowband junction (without filters). The simulated BW is 4.1% (41 MHz), within which IX is larger than 20 dB, IL varies from 1.5 dB to 1.75 dB, and RL is less than 16 dB. Similarly, the measured BW is about 4% (40 MHz), within which TX-to-RX IX is larger than 20 dB, TX-to-ANT IL is less than 2.2 dB, ANT-to-RX IL is less 2.3 dB, while ANT RL and TX RL are less than 14.6 dB and 14 dB, respectively. Simulated and measured results are in fair agreement although the measured IL is about 0.5~0.6 dB larger than the simulated value due to inaccuracies in the commercially available spice models of the used components. Also, the measured *S*-parameters exhibit finite asymmetry, e.g., TX-to-ANT IL and ANT-to-RX IL are different, due to finite tolerances and random parasitics of the components and asymmetries in the layout.

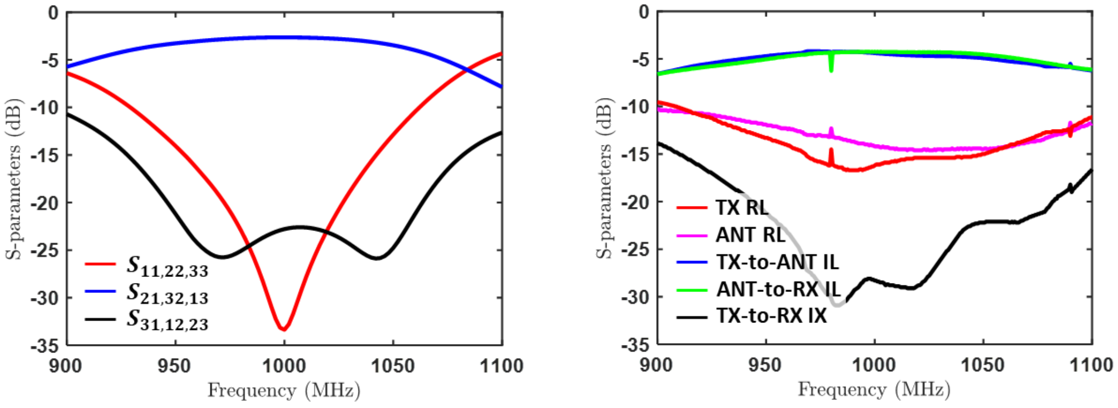

(*a*) (*b*)

Figure 45: *S*-parameters of the broadband network. (a) Simulated. (b) Measured.

Fig. 45(a) and Fig. 45(b) show a comparison between the simulated and the measured *S*-parameters, respectively, of the broadband STM-AM circulator, i.e., after adding the filters. The simulated and measured BW are 12% (120 MHz) and 14% (140 MHz), respectively, i.e., the circulator's BW increased by a factor of three, approximately, compared to the narrowband junction. Also, the simulated in-band TX-to-ANT IL and the

ANT-to-RX IL both vary from 2.5 dB at the center frequency to 4 dB at the band edges while ANT RL and TX RL both vary from 33.4 dB to 11 dB. Compared to the narrowband junction, IL of the broadband circuit increases by about 1 dB due to the added filters (each filter contributes 0.5 dB) while degradation at the edges is larger simply because the 20 dB IX BW has increased. Should IL be limited to 3 dB as required in practice, then the BW effectively reduces to 7.4% which is still 1.85 times larger than the junction's BW. This problem can be mitigated by using distributed elements, at the expense of increasing the form factor. Similarly, the measured in-band TX-to-ANT IL varies from 4.2 dB to 5.8 dB, ANT-to-RX IL varies from 4.25 dB to 5.5 dB, TX-to-RX IX is larger than 20 dB, while ANT RL and TX RL are larger than 11.7 dB and 12.6 dB, respectively. Compared to the simulated results, the higher measured IL is mainly due to model inaccuracies, particularly of the varactors which exhibited lower quality factor than presumed by their spice model in simulations. More importantly, the finite tolerance of the lumped elements in the filters distorts their characteristics and increases reflections, thus further degrading the overall IL. These problems can be overcome by improving the layout symmetry and incorporating more accurate spice models, particularly of the varactors. It is also worth mentioning that the impact of the presented BW extension technique on Pmax, IIP3, and spurious emission is negligible. Therefore, these metrics are strictly determined by the narrowband junction, which was discussed in detail in previous chapters. The NF, on the other hand, degrades in proportion to the additional losses incurred by the filters. Therefore, improving the overall IL as explained earlier would improve the broadband circulator's NF as well.

Chapter 7: CMOS Integrated STM-AM Circulators[5]

In this chapter, we present the first integrated circuit (IC) implementation of STM-AM circulators. In contrast to the designs presented in all previous chapters, the varcaps are realized herein using switched capacitors instead of varactors, which reduces the circuit complexity significantly and eases its chip-scale implementation. We also use an in-house so-called composite Floquet scattering matrix (CFSM) numerical method to expedite the study of the impact of inevitable parasitics and clock non-idealities on the overall performance. We further validate the design with simulated and measured results using a standard 180 nm CMOS technology. Compared to discrete implementations, the presented CMOS circulator chip reduces the size by an order of magnitude and occupies a total area of 36 mm^2.

7.1 DESIGN

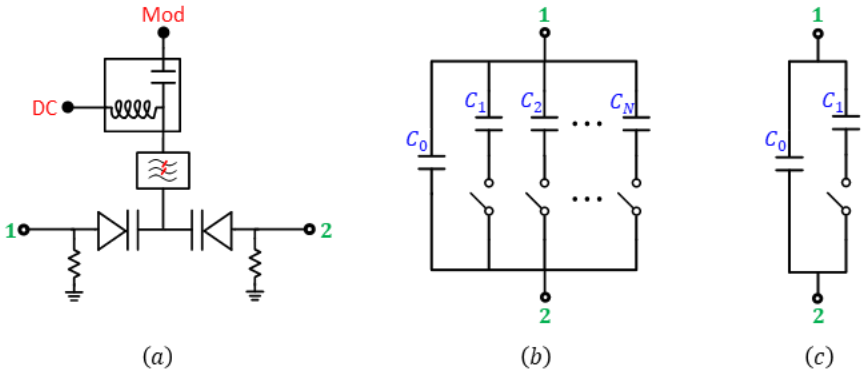

Figure 46: Implementation of the varacp using: (a) Varactors. (b) *N* periodically switched capacitors. (c) BFSK switched capacitor.

---

[5] The content of this chapter is published in [41].

In all previous chapters, the implementations of STM-AM circulators were based on PCB technology and discrete components, which limits their size and cost reduction and prohibits their large-scale production. In order to overcome this problem, an IC implementation is highly desirable. But to achieve this goal, the designs presented earlier must be revised and modified to accommodate the rules and restrictions of IC technologies. For example, the varcaps were implemented thus far using a pair of common-cathode varactors, while injecting the DC bias and the modulation signals to the common node through low-pass filters, as shown in Fig. 46(a). While such implementation does indeed result in excellent performance using discrete components as demonstrated in previous chapters, it actually suffers from several issues that complicate its CMOS integration. First and foremost, the varactors' low-pass filters require using multiple lumped elements with considerably large values, e.g., inductors in the order of hundreds of nH, which cannot be integrated on a chip. Furthermore, the required modulation index to achieve sufficient isolation can in general be quite large, i.e., in the order of 50%. While discrete varactors can achieve such value and maintain a high quality factor at the same time, it is impossible to attain similar performance using standard CMOS components. These problems can be overcome by replacing the varactors with N periodically switched capacitors, as shown in Fig. 46(b). Such implementation not only eliminates the complicated biasing networks of varactors and permits arbitrarily large modulation indices, but it also replaces the sinusoidal signals with digital clocks which are easier to generate in multiple phases and are less sensitive to amplitude noise. The downside, however, is that switched capacitors can only synthesize *quantized* modulation schemes regardless of how large N might be, which results in many IMPs and imposes a restriction on the lowest possible IL, even with ideal lossless components. Fortunately, if these products are sufficiently far from the center frequency, i.e., $f_m >> \mathrm{BW}/2$, then they can be rejected by the junction's bandpass resonance itself. Under this condition, even an abrupt periodic variation of the varcaps between two values, say C_0 and C_0+C_1 as depicted in Fig. 46(c), can lead to good performance. Obviously, this requires the circulator's topology to be of bandpass type. However, the bandstop topologies can still be used in an *N*-way architecture which would eliminate the spurious emission regardless of how quantized the modulation scheme of each unit cell is and without any necessity of further attenuation by the background resonance itself. In this chapter, however, we will focus on the differential current-mode bandpass/wye topology, as an example.

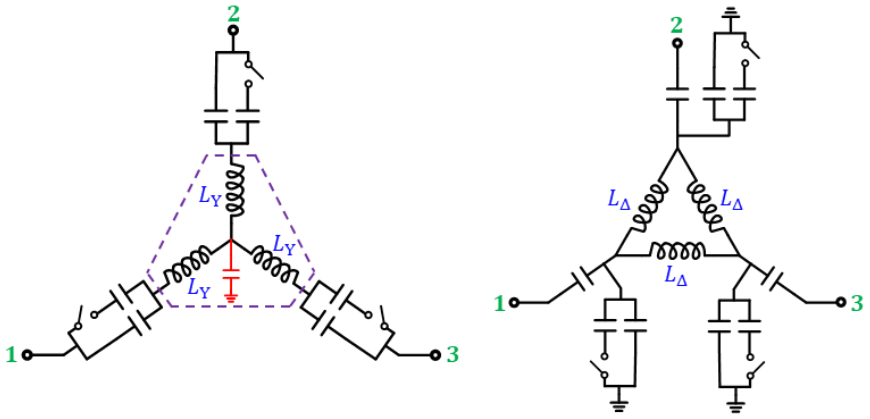

(*a*) (*b*)

Figure 47: (a) Conventional bandpwass/wye topology depicting a shunt parasitic capacitance at the central node. (b) Modified bandpass/wye topology where the inductors are transformed into a delta connection and the varacaps are connected in shunt rather than in series.

One issue specific to the current-mode bandpass/wye topology is that it is sensitive to shunt parasitic capacitance at the centeral node. This parasitic can be considerably large in IC design which reduces the coupling between the three *LC* tanks and isolates them from one another, thus degrading the overall performance. This problem can be overcome by transforming the wye inductors highlighted in Fig. 47(a) into three new delta inductors, as depicted in Fig. 47(b). The downside of this transformation, however, is that the value of each inductor triples. Notice that the switched capacitors in Fig. 47(b) are also connected in shunt rather than in series in order to reduce the swing across them when they are ON, which improves the circulator's power handling and linearity. In this case, these metrics become limited by the OFF state non-linearities which are typically much weaker than those of the ON state in most IC technologies. It is also worth mentioning that any shunt parasitic capacitance at the terminals of the inductance loop of Fig. 47(b) can be absorbed in the switched capacitors, thus easing the integration of this circuit.

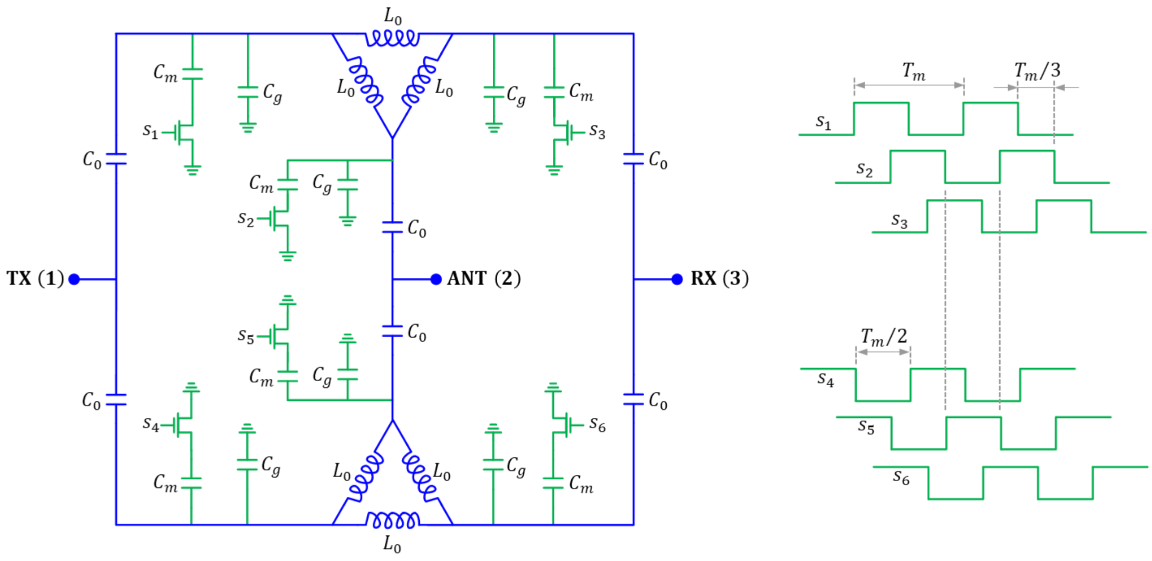

(a)

(b)

Figure 48: CMOS STM-AM circulator based on a modified differential current-mode bandpass/wye topology. (b) Complete schematic. (c) Timing diagram of the switching clocks.

Fig. 48(a) shows the complete schematic of a CMOS STM-AM circulator based on the modified current-mode bandpass/wye topology depicted in Fig. 47(b). Specifically, the circuit consists of two single-ended circulators connected in parallel, each of which consists of three inductors L_0 connected in a loop, the terminals of which are coupled to the RF ports through a capacitor C_0 and to ground through a parallel combination of a static capacitor C_g and a switched capacitor C_m. Fig. 48(b) also shows the timing diagram of the switching clocks s_n, which all have the same frequency $f_m = 1/T_m$ and they are related together as follows

$$s_{n+1}\left(t\right) = s_n\left(t - nT_m/3\right), \quad n = 1, 2, 3 \tag{7.1}$$

$$s_n\left(t\right)\Big|_{n=4,5,6} = s_n\left(t - T_m/2\right)\Big|_{n=1,2,3}. \tag{7.2}$$

In the special case of a 50% duty cycle, (7.2) simplifies to $s_n\big|_{n=4,5,6} = \overline{s}_n\big|_{n=1,2,3}$, i.e., the clocks of the two single-ended circuits are inverted versions of each other. It is worth mentioning that such clocking scheme results in the oscillation frequencies f_n of the *n*-th tank changing periodically between two values, i.e., f_0 and $f_0 - u_0$. Interestingly, this is strikingly similar to the well-known BFSK modulation scheme commonly used in digital communication systems, hence we use the same terminology and refer to the timing diagram of Fig. 48(b) as BFSK clocking. This analogy suggests that more advanced modulation schemes may improve certain metrics of the circulator, e.g., reducing spurious emission or increasing the isolation bandwidth, which is listed among the potential future work summarized in Chapter 9. Notice that this can be combined with the *N*-way architecture to boost its performance.

7.2 ANALYSIS

Element\Value	Theo.	Sim.	Meas.
f_m (MHz)	106	106	106
L_0 (nH)	40	30 (Coilcraft)	30 (Coilcraft)
C_0 (fF)	900	450 (MIM)	450 (MIM)
C_g (fF)	900	N/R	N/R
C_m (fF)	1200	2×800 (MIM)	2×800 (MIM)
V_{dd} (Volt)	N/R	3.3	3.3
W/L (μm/μm)	N/R	(150×2)/0.34	(150×2)/0.34

Table 5: Values of all design parameters used in obtaining the theoretical, simulated, and measured results of the CMOS modified current-mode bandpass/wye STM-AM circulator.

Table 5 summarizes the values of all elements and parameters used in obtaining the numerical results to be discussed in this section. The values used in obtaining the simulated and measured results, which will be discussed in Sec. 7.3, are also listed. The inductors L_0 and the capacitors C_0 were chosen such that the unmodulated circuit of Fig. 48(a) would resonate at the target frequency of 915 MHz. Then, the modulation frequency f_m was set to 106 MHz, i.e., 11.6% of the center frequency. Such a small value permits feeding the modulation signals externally from regular testbench generators as was the goal in this design. In future implementations, however, the modulation sources should be integrated with the circulator on the same chip which would allow using higher f_m if necessary. Recall that higher f_m would push the IMPs further away from the center frequency, thus improving the spurious emission of the circulator and reducing its IL, as explained earlier. It is also worth mentioning that the specific value of 106 MHz was chosen to avoid any high-order harmonics of the modulation signals landing inside the desired BW centered around 915 MHz. Based on this choice of f_m, the capacitors C_g and C_m were chosen to maximize the achieved IX at 915 MHz. Finally, the transistors were sized at $\mathrm{W/L} = (150 \times 2\mu)/340\mathrm{n}$ to minimize their on-resistance.

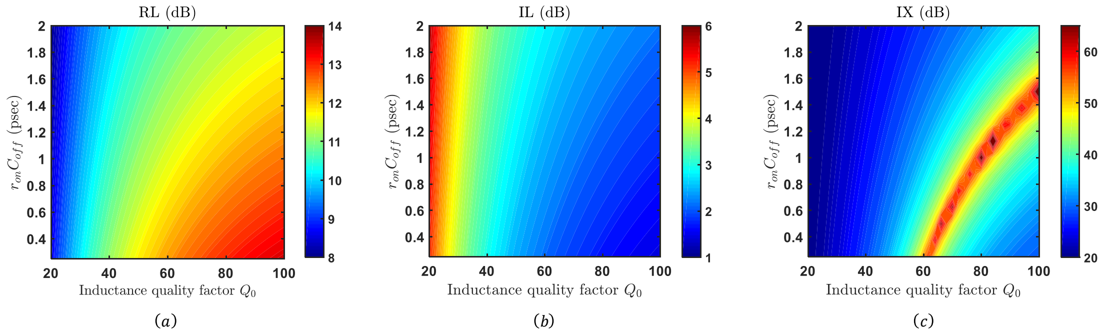

Figure 49: Impact of switch parasitics $r_{on}C_{off}$ and inductance quality factor Q_0 on the *S*-parameters. (a) RL. (b) IL. (c) IX.

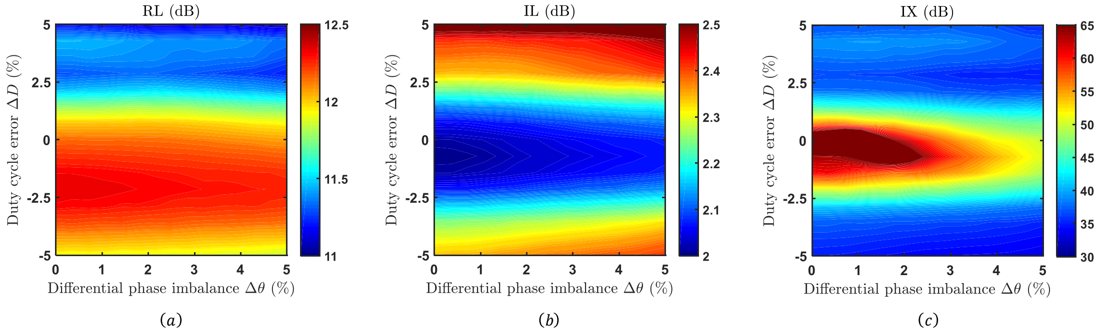

Figure 50: Impact of duty cycle error ΔD and differential phase imbalance $\Delta\theta$ on the *S*-parameters. (a) RL. (b) IL. (c) IX.

The IL of the presented CMOS STM-AM circulator strictly depends on the strength of the IMPs and the resistive losses due to finite $r_{on}C_{off}$ of the switches and Q_0 of the inductors. Since the differential architecture reduces the IMPs sufficiently, their contribution can be neglected and we may focus on studying the impact of the resistive losses. Fig. 49 shows the impact of changing these parameters on the numerical *S*-parameters obtained using an in-house so-called CFSM numerical method (see Appendix C). Intuitively, larger Q_0 and smaller $r_{on}C_{off}$ leads to better RL and IL, as indeed depicted in Fig. 49. For instance, $r_{on}C_{off} = 0.4$ psec and $Q_0 = 80$ results in RL and IL of about 12.8 dB and 1.8 dB, respectively. While such value of $r_{on}C_{off}$ can be achieved using deep-submicron CMOS technologies, $Q_0 = 80$ is only possible using off-chip inductors. The quality factor of on-chip inductors, on the other hand, is in the order of 10~20 at the first few GHz, which makes achieving low IL more challenging and limits the miniaturization of the proposed circuit. For example, Fig. 49(a) and Fig. 49(b) show that $r_{on}C_{off} = 0.4$ psec and $Q_0 = 20$ results in RL and IL of 8.6 dB and 5.2 dB, respectively. This is because STM-AM circulators, similar to their magnetic counterparts, are resonant circuits, therefore their IL is sensitive to the resonance unloaded quality factor. Therefore, we will assume that the inductors in this design are off-chip. Another reason to motivate this assumption is that the value of L_0 is quite large, i.e., 30 nH, which is difficult to be implemented on a chip. On the other hand, Fig. 49(c) shows a rather non-trivial dependence of the maximum possible IX on $r_{on}C_{off}$ and Q_0. In fact, for each $r_{on}C_{off}$ there is a specific Q_0 at which a near-perfect IX can be achieved. For example, the optimal Q_0 for $r_{on}C_{off} = 0.4$ psec is about 64. Either a smaller or even a larger Q_0 would reduce the maximum possible IX. In practice, however, it is sufficient to maintain an in-band IX larger than 20~30 dB, i.e., the level at which ANT reflections due to dynamic impedance mismatches begin to dominate the leakage at the RX port. Fig. 49(c) shows that such level is maintained for Q_0 ranging from 20 to more than 100, thus showing that the IX of the proposed circuit is insensitive to the inevitable random variations of the losses.

The clock signals in Fig. 48(b) are assumed to be generated externally using three phase-locked RF sources, thus allowing precise control of the duty cycle and the relative phases. In real applications, however, these clocks will be generated on-chip, which can be easily achieved using digital circuitry, but they will also be prone to phase noise, jitter, and duty cycle errors. In order to quantify the sensitivity of the proposed circulator to such errors, Fig. 50 shows the numerical *S*-parameters versus fractional errors ΔD and $\Delta\theta$ in the duty cycle and the phase difference between the constituent single-ended circulators, respectively. Clearly, the network is quite tolerant to differential phase imbalance, allowing $\Delta\theta \approx 2$% (for $\Delta D = 0$) without any noticeable degradation in its performance. The requirements on the duty cycle errors, however, turn out to be more stringent. For instance, $\Delta D \approx +0.7$% (expansion of the switching on-time leading to overlap periods between the clocks of the single-ended circuits) with $\Delta\theta = 0$ reduces the IX by about 20. In contrast, $\Delta D \approx -0.7$% (compression of the switching on-time) leads to only 12 dB IX degradation and even a modest improvement of RL and IL compared to the ideal case, clearly indicating that it is important to ensure that the switches in each of the circulators do not overlap.

7.3 RESULTS

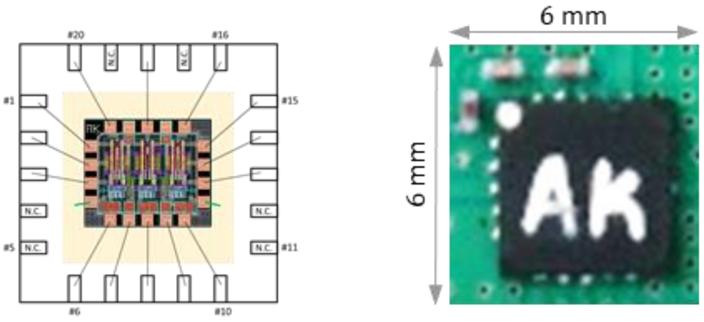

(a) (b)

Figure 51: (a) Picture of the chip layout. (b) Top-view photograph of the packaged chip mounted on a PCB. Three more inductors are placed at the bottom side of the PCB.

Based on the numerical findings of Sec. 7.2 and Sec. 7.3, an IC STM-AM circulator was designed for operation at 910 MHz using a standard 180 nm CMOS technology. Table 5 summarizes the values of all elements and parameters used in obtaining the simulated and measured results to be discussed in this section. Notice that these values are different than their numerical counterparts due to the additional parasitics of the physical elements. In particular, C_g was entirely eliminated since the shunt parasitic caps of the off-chip inductors were sufficient to realize it without requiring any additional on-chip capacitors. Fig. 51(a) also shows a picture of the chip layout where the active silicon area occupied by the circulator is only 0.2 mm^2. The chip was also mounted in a 5×5 mm^2 QFN package and connected to off-chip inductors on a PCB for testing, as shown in Fig. 51(b). The total form factor is 6×6 mm^2 which is at least one order of magnitude smaller than the discrete implementations presented in previous chapters.

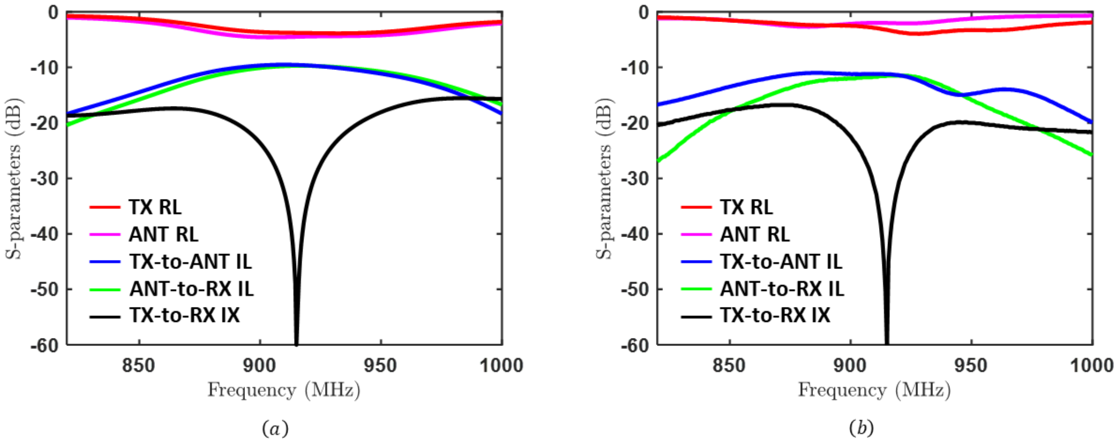

Figure 52: *S*-parameters before matching. (a) Simulated. (b) Measured.

Fig. 52(a) and Fig. 52(b) show a comparison between the simulated and measured *S*-parameters of the circulator, respectively, when its ports are all terminated with 50 Ohm impedances. Obviously, large TX-to-RX IX of more than 60 dB is achieved at a center frequency of 915 MHz in both cases, however, the circulator also exhibits significant transmission losses. Specifically, the measured TX-to-ANT IL and ANT-to-RX IL are 11 dB and 11.5 dB, respectively. These large values are not actually due to resistive or even spurious emission losses but they are rather an artifact resulting from strong impedance mismatch as evident by the significant TX RL and ANT RL of 3.8 dB and 2.3 dB, respectively. This matching problem was not predicted in our initial simulations since the custom-designed electrostatic discharge (ESD) protection circuitry was not taken into account. After taking the measurements, however, we realized that the ESD diodes introduce significant shunt parasitics at the ports, which lead to strong reflections. When the ESD circuit was accurately modeled and incorporated in post-layout simulations, the results agreed well with the measurements and the matching problem was similarly observed. Specifically, the simulated TX-to-ANT IL and ANT-to-RX IL are both found to be 9.6 dB, while the TX RL and ANT RL are 4.3 and 3.8 dB, respectively.

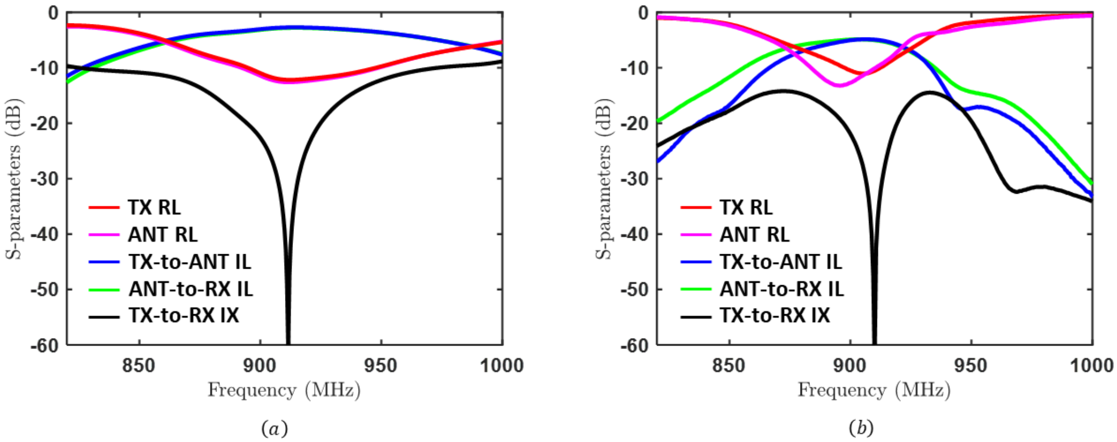

Figure 53: *S*-parameters after matching. (a) Simulated. (b) Measured.

The above problem was fixed in simulations by adding proper matching networks at the circulator's ports to tune out the ESD parasitics, thus yielding the results depicted in Fig. 53(a). As we can see, the TX RL and ANT RL both improve to 12.5 dB and, subsequently, the TX-to-ANT IL and ANT-to-RX IL reduce to about 3 dB. Also, the center frequency is shifted down to about 912 MHz. These results were experimentally validated by using three external reconfigurable impedance tuners, yielding the measured results shown in Fig. 53(b). The measured TX RL and ANT RL are 11 dB and 13 dB, respectively, the measured TX-to-ANT IL and ANT-to-RX IL are both 4.8 dB, and the center frequency is about 910 MHz. Furthermore, the simulated and measured 20 dB IX BW are 3.4% (31 MHz) and 2.4% (22 MHz), respectively. It is worth mentioning that the IL can be reduced to less than 3 dB, as predicted by the numerical analysis of Sec. III, by further optimizing the chip and the PCB layouts and by better designing the IC supplementary blocks, namely, the modulation path buffers and the ESD protection circuit. Fig. 54 also shows a comparison between the simulated and measured transmission phases, which are all quite linear within the BW of interest, similar to all previous designs based on varactors.

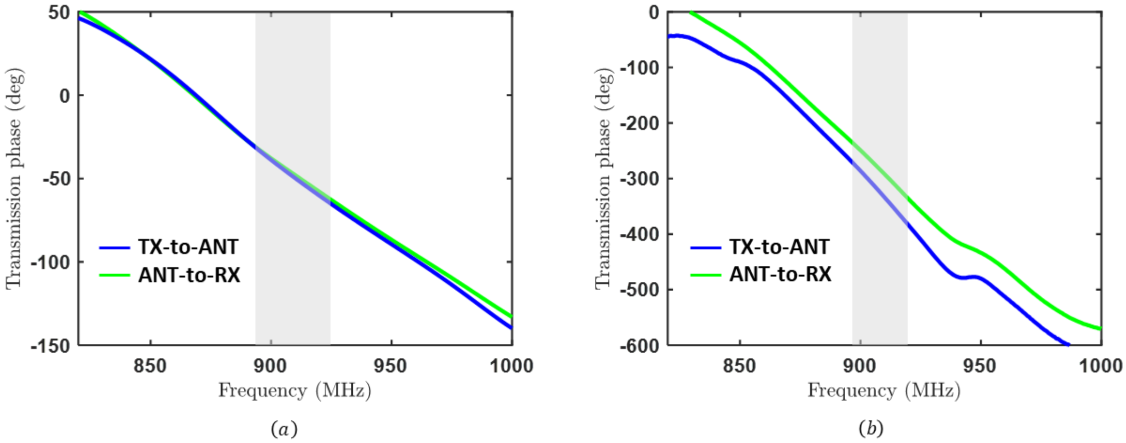

Figure 54: Transmission phase. (a) Simulated. (b) Measured.

Fig. 55(a) and Fig. 55(b) also show a comparison between the simulated and measured spectrums, respectively, at both the ANT and the RX ports for a monochromatic TX excitation with an input frequency f_{in} of 1 GHz and an input power P_{in} of 0 dBm. The fundamental harmonic at the ANT port exhibits a simulated IL of 3 dB and a measured IL of 4.8 dB, in agreement with the *S*-parameters. However, the fundamental harmonic at the RX port depicts a simulated and a measured IX of 37 dB and 42 dB, respectively, instead of 65 dB, as predicted by the *S*-parameters. This is simply because the input frequency of the TX signal is not aligned with the IX dips in Fig. 53. In addition to the fundamental component, the spectrums at both the ANT and RX ports are also contaminated with many spurs. These are essentially higher-order harmonics of the modulation signals and IMPs resulting from their mixing with the TX input signal. The largest measured IMPs are those at 809 MHz and 1021 MHz, which are –19 dBc and –22 dBc, respectively, while the simulated value of both is –22 dBc. In general, these products depend strongly on the balance of the differential circuit, hence they are more sensitive to layout asymmetries than other metrics such as the *S*-parameters. Also, as mentioned earlier, the modulation signals in this design are generated externally from regular testbench sources which are configured to generate three 120 deg phase shifted sinusoidal signals at frequency f_m. These signals are then fed to the chip through ESD protected pins and buffered through a series of inverters that transform them into digital clocks which are eventually applied to the gates of the switches. As one may expect, these clocks are not perfect square waves and they may incur considerable amplitude variations which enrich their frequency content. This, in turn, explains why the beat frequency in Fig. 55(a) and Fig. 55(b) is smaller than f_m. As one may expect, such spurious emission must be further suppressed in order to comply with the spectral mask regulations of commercial systems and to avoid interference with adjacent channels. This can be achieved by using the *N*-way architecture presented in Chapter 5. Also, the modulation signals ought to be generated on chip rather than feeding them from external sources, which would ease controlling their frequency content and ensure that they are exactly square waves with a fundamental frequency f_m. This, in turn, eliminates many spurs and allows to increase f_m in order to push the IMPs away from the BW of interest so that they exhibit more attenuation by the natural bandpass response of the resonant wye junctions themselves.

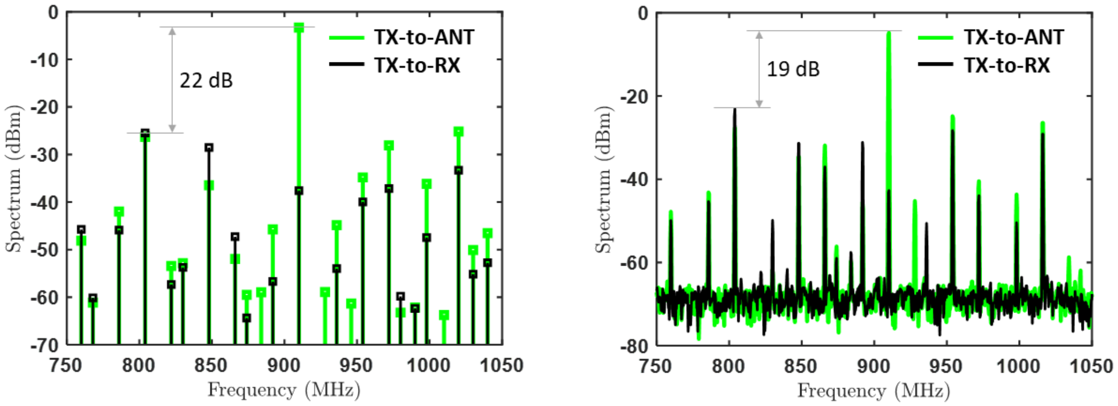

(a) (b)

Figure 55: ANT and RX spectrums for a monochromatic TX excitation with an input frequency f_{in} of 910 MHz and an input power P_{in} of 0 dBm. (a) Simulated. (b) Measured.

Finally, the TX-to-ANT and ANT-to-RX IIP3 are measured and found to be +6.1 dBm and +6 dBm, respectively. These values are, in fact, currently limited by the ESD protection circuitry which, as mentioned earlier, was not optimally designed. Therefore, should this issue be fixed in future designs, the IIP3 is expected to increase. Also, an RX NF of 5.2 dB was measured at the center frequency of 910 MHz. This is only 0.4 dB larger the ANT-to-RX IL, thus showing negligible degradation due to the modulation phase and amplitude noise.

Chapter 8: MEMS STM-AM Circulators[6]

In this chapter, we explore the use of high-Q MEMS resonators to reduce the modulation frequency and the total required inductance in STM-AM circulators, thus permitting low-power highly miniaturized implementations of such components. As an example, we use commercial off-the-shelf thin-film bulk acoustic resonators (FBARs) to design a current-mode bandpass/wye STM-AM circulator at a center frequency of 2.5 GHz with a modulation frequency of 40 MHz (1.6% of 2.5 GHz) and six 12 nH inductors. In contrast to conventional LC implementations presented in previous chapters, the inductors herein do not play any role in breaking reciprocity and are merely to tune out the parasitic parallel capacitance of the MEMS devices. Therefore, they can be further reduced using custom-designed contour-mode resonators (CMRs).

---

[6] The content of this chapter is published in [42].

8.1 ANALYSIS

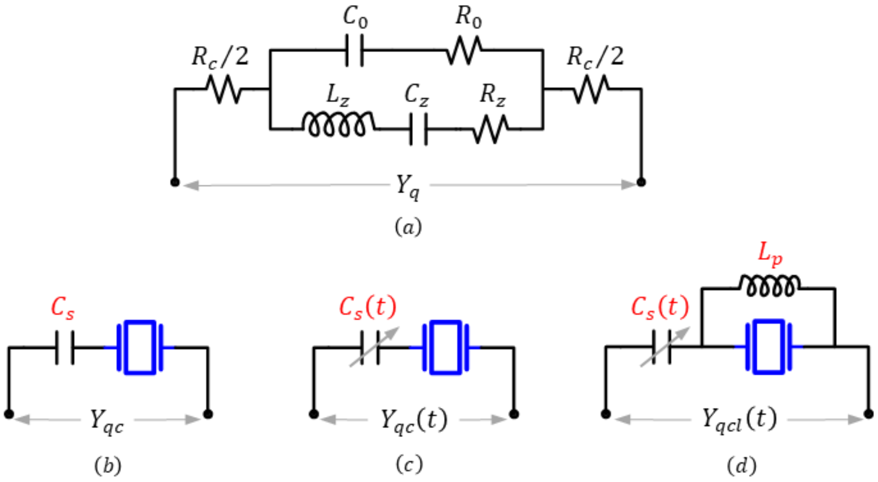

Figure 56: (a) MBVD electrical model of MEMS resonators. (b) MEMS resonator in series with a static capacitor C_s. (c) MEMS resonator in series with a varcap $C_s(t)$. (d) MEMS resonator in parallel with an inductor L_p, and both are in series with a varcap $C_s(t)$.

MEMS resonators, such as FBARs or CMRs, are micro-machined integrated devices which rely on Aluminum Nitride (AlN) piezoelectric materials and refractory motional metal electrodes to realize super high-*Q* oscillations. The electrical characteristics of such devices can be accurately described from a terminal perspective by means of equivalent circuit models, which simplify the design and analysis of more complicated networks composed of one or more of these devices in addition to other elements. For one-port resonators, the lumped-element modified Butterworth Van Dyke (MBVD) model shown in Fig. 56(a) can be extracted from the measured device impedance $Z_q = 1/Y_q$ and it consists of a motional R_z - L_z - C_z arm in parallel with another static R_0 - C_0 arm, all in series with two electrode resistors $R_c/2$. This model shows that the device exhibits both series and parallel (or anti) resonances, the center frequencies of which can be calculated from $\mathrm{Im}\{Z_q\} \to 0$ and $\mathrm{Im}\{Z_q\} \to \infty$, respectively, which results in

$$f_s = \frac{1}{2\pi\sqrt{L_z C_z}} \tag{8.1}$$

$$f_p = f_s\sqrt{1+\frac{C_z}{C_0}}\,. \tag{8.2}$$

An effective electromechanical coupling coefficient k_t^2 relating f_s and f_p is also defined as follows

$$k_t^2 = \frac{\pi^2}{4}\frac{f_s}{f_p}\left(1-\frac{f_s}{f_p}\right). \tag{8.3}$$

Assuming $C_z << C_0$, which is typically the case in practice, and substituting (8.3) into (8.1) and (8.2) yield

$$C_z \approx \frac{8}{\pi^2} C_0 k_t^2 \tag{8.4}$$

$$L_z = \frac{1}{\omega_s^2 C_z}\,. \tag{8.5}$$

The finite quality factors Q_s and Q_p of the series and parallel resonances, respectively, are also given by

$$Q_s = \frac{\omega_s L_z}{R_z} \tag{8.6}$$

$$Q_p = \frac{1}{\omega_p C_0 R_0}, \tag{8.7}$$

where R_z and R_0 are the losses due to the mechanical motion and thermal dissipation in the AlN material, respectively. Since R_c is usually much smaller than both R_z and R_0, then it can be neglected, in which case, the device admittance Y_q can be calculated as follows

$$Y_q = \frac{1/R_0}{1 - jQ_p \dfrac{f_p}{f}} + \frac{1/R_z}{1 - jQ_s \dfrac{f_s}{f}\left(1 - \left(\dfrac{f}{f_s}\right)^2\right)}. \tag{8.8}$$

Now using this model, we can study the performance of the MEMS device when it is connected to other elements with the goal of building an STM-AM circulator in mind. First, consider adding a static capacitor C_s in series with a MEMS device as depicted in Fig. 56(b). Using simple circuit analysis and assuming $C_s >> C_z$, one can show that the new series resonance frequency $f_{s,qc}$ of the combined circuit is related to the original $f_{s,q}$ by

$$f_{s,qc} \approx f_{s,q}\left[1 + \frac{C_z}{2\left(C_0 + C_s\right)}\right]. \tag{8.9}$$

Also, the new device admittance Y_{qc} at $f_{s,qc}$ reads

$$Y_{qc}\left(f_{s,qc}\right) \approx \frac{Y_q\left(f_{s,q}\right)}{1 + C_0/C_s}. \tag{8.10}$$

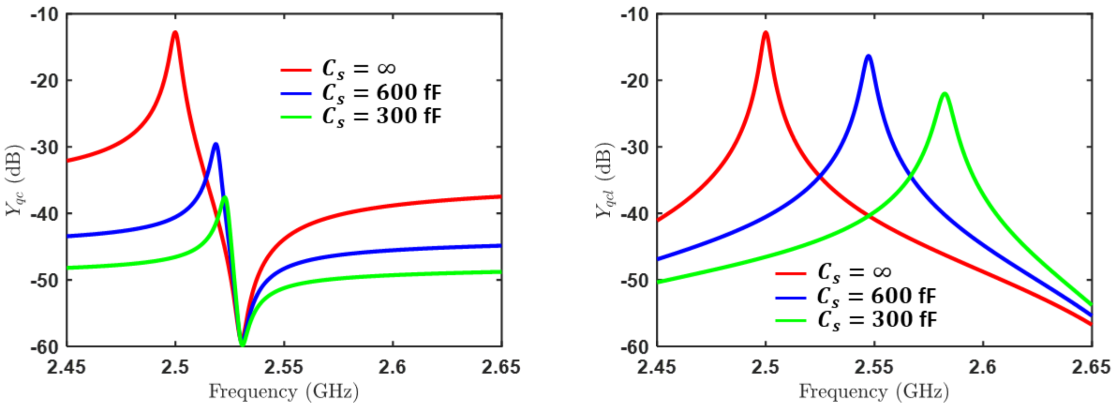

(a) (b)

Figure 57: Effective device admittance. (a) MEMS device in series with a static cap C_s. (b) MEMS device in parallel with a small inductor L_p and both are in series with C_s.

Equations (8.9) and (8.10) show that by reducing C_s, not only $f_{s,qc}$ increases but also Y_{qc} decreases. For example, Fig. 57(a) shows the simulated Y_{qc} with k_t^2 of 3%, Q_s of 600, f_s of 2.5 GHz, and different values of C_s. Indeed, Y_{qc} decreases from –12.8 dB → –29.6 dB → –37.6 dB and $f_{s,qc}$ increases from 2.5 GHz → 2.518 GHz →2.523 GHz, as C_s decreases from ∞ → 600 fF → 300 fF. The tunability of $f_{s,qc}$ implies that a modulated bandpass resonance can be realized by connecting a MEMS device in series with a varcap $C_s(t)$ as depicted in Fig. 56(c). Recall that such varcap is implemented by using either varactors or switched capacitors, which results in a sinusoidal or a discrete capacitance variation, respectively, between two thresholds, say $C_{s,1}$ and $C_{s,2}$. Also, if the modulation frequency f_m is maintained sufficiently low, i.e., $f_m/f_s < 5\%$, then samples of the dyanmic admittance $Y_{qc}(t)$ corresponding to certain values of $C_s(t)$, e.g., ∞, 600 fF, and 300 fF, can be approximated by the quasi-static results shown in Fig. 57(a). In other words, $Y_{qc}(t)$ and, consequently, transmission through it are both expected to dramatically reduce if either the average capacitance of the varcap $(C_{s,1}+C_{s,2})/2$ became small or the modulation index $\Delta C = (C_{s,2}-C_{s,1})/2$ became large. But a large modulation index is necessary, as explained in previous chapters, to achieve large IX and low IL in STM-AM circulators. In order to overcome this problem, an inductor L_p can be connected in parallel with the MEMS device, as shown in Fig. 56(d), to tune out C_0, where

$$L_p = \frac{1}{\omega_s^2 C_0}. \tag{8.11}$$

In this case, the new resonance frequency $f_{s,qcl}$ and effective total admittance Y_{qcl} can be calculated by substituting $C_0 \approx 0$ in (8.9) and (8.10), respectively, resulting in $Y_{qcl}\left(f_{s,qcl}\right) \approx Y_q\left(f_{s,q}\right)$ and $f_{s,qcl} \approx f_{s,q}\left(1+C_z/2C_s\right)$. In other words, the series resonance of the MEMS device can be strongly modulated by $C_s(t)$ without much impact on the total effective admittance. In order to validate this result, an inductor of 4 nH inductor is connected in parallel with the same MEMS device used earlier and the the total effective admittance Y_{qcl} is calculated for the same values of C_s, i.e., ∞, 600 fF, and 300 fF. Fig. 57(b) shows that Y_{qcl} decreases from –12.8 dB → –16.33 dB → –22 dB and $f_{s,qcl}$ increases from 2.5 GHz → 2.547 GHz →2.582 GHz, respectively, thus showing that the reduction of Y_{qcl} is indeed significantly mitigated while $f_{s,qcl}$ is still strongly modulated. Moreover, the anti-resonance $f_{p,dcl}$ is shifted to higher frequencies, thus improving the symmetry of the series resonance's dispersion, which would improve the *S*-parameters of the circulator. Equation (8.11) also shows that L_p can be reduced by simply using a MEMS device with a larger C_0. For example, $C_0 = 10$ pF, which is a very realistic value, results in L_p of only 0.4 nH. Such a small inductor can be easily integrated at a small factor. In fact, it can be even realized using bondwires which also exhibit a high quality factor, although *Q* of L_p is not of significant importance and its impact on the circulator's IL is negligible because it is not part of the modulated resonance that leads to non-reciprocity. Therefore, an on-chip chiral inductor with a *Q* of 10~20 is still sufficient.

8.2 DESIGN

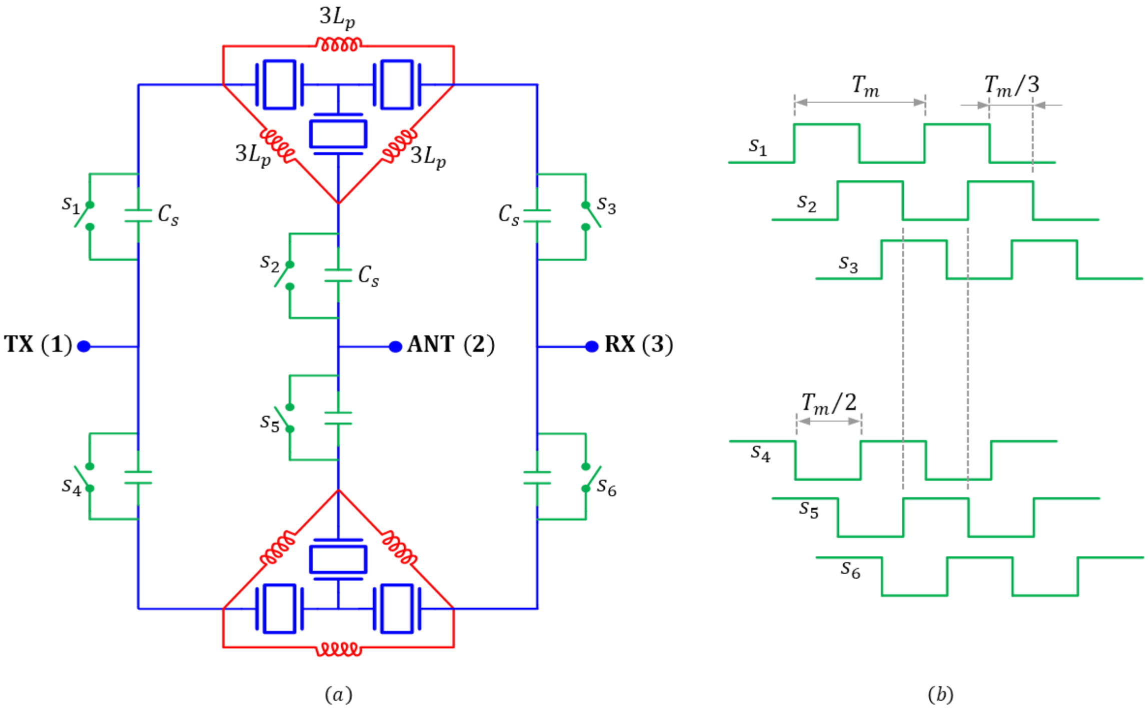

Figure 58: MEMS STM-AM circulator based on the current-mode bandpass/wye topology. (a) Complete schematic. (b) Timing diagram of the switching clocks.

Fig. 58(a) shows the complete schematic of a MEMS STM-AM circulator based on the current-mode bandpass/wye topology. The circuit consists of two single-ended circulators connected in parallel, each of which contains three MEMS devices, three parallel inductors, and three varcaps. The inductors tune out the parasitic capacitance C_0 of the MEMS devices, and they are connected in a loop rather than to the central node of the MEMS devices using the wye-to-delta transformation illustrated in Chapter 7 to simplify the layout. Notice that this transformation increases the value of each inductor by a factor of 3 but since the experimental validation presented in this chapter is already based on discrete components, then this is not of major concern and it is more important to simplify the layout. In a fully integrated implementation, however, which is listed among the potential future work summarized in Chapter 9, this transformation should not be used and the inductors should be kept small. Also, the varcaps are implemented using a single capacitor C_s in parallel with a switch s_n, where *n* is the switch index , i.e., $C_{s,1} = \infty$ and $C_{s,2} = C_s$, therefore the resonance frequency changes between f_s and $f_s\left(1+C_z/2C_s\right)$, respectively. Fig. 58(b) shows the timing diagram of the switching clocks, which all have the same frequency f_m and the same duty cycle of 50%. Similar to the CMOS circulator presented in Chapter 7, the three clocks of each single-ended circuit are mutually shifted by $T_m/3$, where $T_m = 1/f_m$ is the period, and that the two single-ended circuits use inverted clocks. It is also worth mentioning that this circuit can be used as a unit element to build an *N*-way STM-AM circulator to increase the power handling and improve the spurious emission as explained in Chapter 5. Also, all implementations must be based on a bandpass topology, either wye or delta. The bandstop topologies, on the other hand, cannot be used since MEMS devices are essentially bandpass resonators. In the next Section, we validate this circuit with both simulated and measured results using commercial FBAR resonators.

8.3 RESULTS

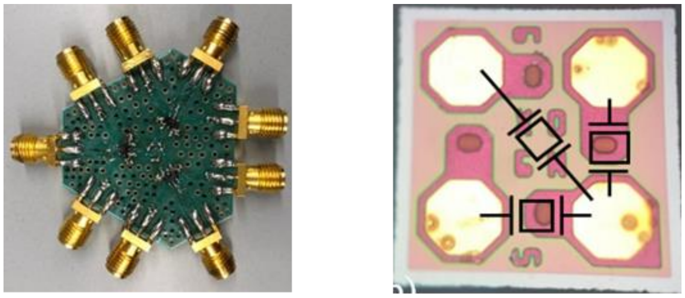

(*a*) (*b*)

Figure 59: (a) Photograph of the fabricated board. (b) Micro-photograph of the MEMS devices.

Element\Value		Theo. & Sim.	Meas.
MEMS	f_{ctr} (MHz)	~2550	~2500
	k_t^2 (%)	3	Broadcom FBAR custom-designed chip
	Q_s	600	
	C_0 (pF)	1	
Inductors	$3L_p$ (nH)	12	12 (Coilcraft)
Modulation	f_m / f_{ctr} (%)	1.56	1.6
	V_m (Vpp)	N/R	5
	C_s (fF)	200	200 (Murata)

Table 6: Values of all design parameters used in obtaining the theoretical, simulated, and measured results of the MEMS current-mode bandpass/wye STM-AM circulator.

Fig. 59(a) shows a photograph of the fabricated board based on the schematic of Fig. 58(a) and the measured results were taken using the same experimental setups in Appendix A. Each three wye-connected MEMS devices were implemented using a single non-commercial custom-designed chip from Broadcom Incorporate, a microphotograph of which is depicted in Fig. 58(b). The series resonance of all devices is ~2.5 GHz, k_t^2 is ~3%, Q_s is ~600, and C_0 is ~1 pF. Thereafter, L_p can be calculated using (8.11) which results in 4 nH. Also, each pair of differential switches, e.g., s_1 and s_4, were also implemented using a MACOM single-pole double-throw (SPDT) switch. Finally, the optimal modulation parameters, i.e., C_s and f_m, were chosen through parametric studies in simulations, resulting in 200 fF and 40 MHz, respectively. Notice that the modulation frequency is 1.6% of the 2.5 GHz center frequency, which is the smallest among all magnetless parametric circulators presented to the date of writing this dissertation. On the other hand, the form factor is 10mm×10mm which is quite large compared to the CMOS chip presented in Chapter 7, merely because we relied in this experimental demonstration on discrete off-the-shelf components, as mentioned earlier. For convenience, Table 6 summarizes the values of all elements and parameters discussed above.

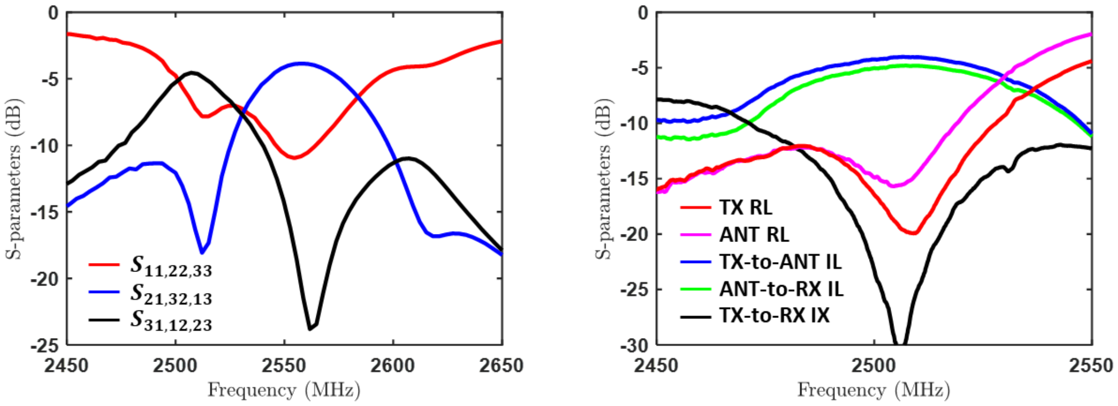

(a) (b)

Figure 60: *S*-parameters. (a) Simulated. (b) Measured.

Fig. 60(a) and Fig. 60(b) show the simulated and measured *S*-parameters, respectively. The simulated 20 dB IX BW is ~15 MHz, i.e., 0.6% of the ~2.55 GHz center frequency, within which IL varies from 3.6 dB dB to 4.2 dB and RL varies from 8.7 dB to 11 dB. On the other hand, the measured 20 dB IX BW is about 18 MHz (0.72%), within which TX-to-ANT IL varies from 4 dB to 4.4 dB and ANT-to-RX IL varies from 4.8 dB to 5.2 dB while ANT RL varies from 12 dB to 15.6 dB and TX RL varies from 15 dB to 20 dB. Obviously, the BW is quite narrowband, i.e., about 5 times less than the BW of conventional *LC* implementations. Nevertheless, it can be improved by applying the BW extension technique presented in Chapter 6. The measured results also exhibit finite asymmetry, e.g., TX-to-ANT IL and ANT-to-RX IL are different, due to finite tolerances and random parasitics of the components and asymmetries in the layout. Finally, the other metrics, namely, spurious emission, power handling, linearity, and NF, are not particularly impacted by the use of MEMS devices but they are rather dependent on the switches. Specifically, the measured second-order IMP are –20 dBc, the measured P1dB is +28 dBm, and the measured IIP3 is +40 dBm, which are in the same order of previous results of conventional *LC* implementations.

Chapter 9: Conclusions and Future Work

In this final chapter, we draw our conclusions and summarize the results presented in this dissertation. We also provide an outlook on future directions in this exciting line of research.

9.1 CONCLUSIONS

Metric\Design	S.E. (meas.)	Diff. (meas.)	8-Way (sim.)	Broad. (meas.)	CMOS (meas.)	MEMS (meas.)
Technology	Discrete	Discrete	N/A	Discrete	CMOS 180nm	MEMS /Discrete
Center freq. (MHz)	1000	1000	1000	1000	915	~2500
Mod. freq. (%)	19	10	10	11	12	1.6
BW (%)	2.4	2.3	3	14	4.3	0.72
IX (dB)	>20	>20	>20	>20	>20	>20
IL (dB)	<3.4	<2	<2.3	<5.8	<5	<5
RL (dB)	>9	>20	>20	>12.6	>9	>15
Trans. Phase (deg)	Linear	Linear	Linear	Linear	Linear	Linear
P1dB (dBm)	+29	+29	+39	+23	N/A	+28
IX20dB (dBm)	+29	+28	+41	+23	N/A	N/A
IIP3 (dBm)	+33	+32	+43	+35	+6.1	+40
NF (dB)	<4.5	<2.7	<2.3	N/A	<5.4	N/A
Max. IMPs (dBc)	–11 @ $f_0 \pm f_m$	–30 @ $f_0 \pm f_m$	<–62	N/A	–19 @ $f_0 \pm f_m$	–20 @ $f_0 \pm f_m$
Size (mm2)	143	286	N/A	480	36	100

Table 7: Summary of all the results presented in this dissertation. The best values of all metrics are highlighted in green.

In this dissertation, we introduced the underlying physical principles, the detailed circuit implementations, and the theoretical, simulated, and measured results of the so-called STM-AM magnetless circulators. Several new time-varying networks that mimic magnetic-biased ferrite cavities were invented. Specifically, four single-ended (S.E.) topologies based on connecting series or parallel *LC* tanks in a loop or to a central node were presented. Differential (Diff.) voltage- and current-mode architectures were also developed in order to cancel the IMPs resulting from time variation in the single-ended circuits, thus improving the performance of several metrics, e.g., IL and NF, and allowing to reduce the modulation frequency considerably. The differential circuits were also used as unit elements to develop *N*-way circulators which result in near zero-spurious emission and allow to handle arbitrarily high input powers. A broadband (Broad.) implementation was also developed by connecting identical bandpass filters with a particular output impedance at the ports of a narrowband differential circulator in order to match it over a wider frequency range to the TX, RX, and ANT ports. Furthermore, the first CMOS implementation of such components was developed in order to reduce their size, cost, and allow their large scale production. The use of MEMS devices such as FBARs to reduce the total inductance was also investigated. A rigorous analysis of all circuits was performed to facilitate their design, to gain an insight into the impact of changing all parameters on the overall performance, and to derive upper bounds on crucial metrics such as the isolation bandwidth. The analytical results were also validated through simulations and measurements, exhibiting excellent agreement and showing unprecedented performance in many metrics, including large isolation, small insertion loss, excellent matching, linear transmission phase, wide bandwidth, large power handling, high linearity, small noise figure, near-zero spurious emission, small size, low cost, and low power consumption. For convenience, all results are summarized in Table 7. This technology can help enable low-cost commercial full-duplex radios by allowing the TX and RX nodes of each transceiver to share a single antenna while achieving the first critical 20 dB of the total required self-interference cancellation thus relaxing the design of the following layers of isolation based on mixed-signal or DSP techniques.

9.2 FUTURE WORK

The work presented hitherto has shown for the first time that magnetless circulators can satisfy the challenging requirements of practical full-duplex radios. Several new circuits have been invented, analyzed, and experimentally validated. Nevertheless, several points are still required to push this technology forward until it is successfully commercialized, which include:

1. Experimental validation of the single-ended and differential bandpass/delta and bandstop/wye topologies.
2. Experimental validation of the *N*-way circulator.
3. Development of a CMOS broadband *N*-way STM-AM circulator.
4. Development of a fully-integrated MEMS STM-AM circulator.
5. Development of an inductorless magnetless circulator based on STM-AM biasing of lowpass or highpass RC filters.
6. Testing the circulator in an actual full-duplex system.

Appendices

A. Experimental Setups

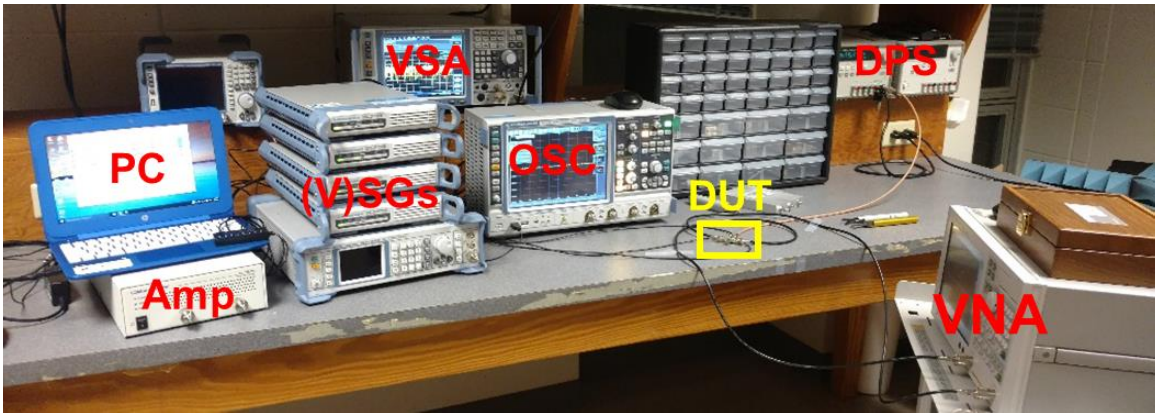

Figure 61: Photograph of the experimental setup.

Instrument	**Manufacturer**	**Model**	**Quantity**
Digital power supply (DPS)	Keysight	E3631A	2
Vector network analyzer (VNA)	Keysight	E5071C	1
Vector signal analyzer (VSG)	Rhode & Schwarz	FSVA40	1
Vector signal generator (VSG)	Rhode & Schwarz	SGT100A	1
Signal generator (SG)	Rhode & Schwarz	SGS100A	2
Oscilloscope (OSC)	Rhode & Schwarz	RTO1044	1
Average power sensor (PS)	Rhode & Schwarz	NRP-Z24	1
High power amplifier (Amp)	Minicircuits	TVA-4W-422A+	1
Excess noise ratio (ENR) source	Keysight	346A	1

Table 8: List of equipment used in obtaining the measured results of all designs presented in this dissertation.

In this Appendix, we present the experimental setups used to take the measured results provided in this dissertation. Fig. 61 shows a photograph of the setup and Table 8 lists the used equipment. In all previous chapters, the device under test (DUT) always had 7 ports in total. One of these is for DC biasing, three are for the modulation signals, and the remaining three are the circulator's terminals themselves. The DC port is connected to the output of a digital power supply that is preconfigured to the required DC voltage. Also, the DUT modulation ports are connected to three phase-locked RF SGs. These sources are pre-configured using a laptop and a USB connection to have a 120 deg phase increment while maintaining the required frequency and amplitude. Thereafter, the DUT circulator ports are connected to different equipment to characterize the performance of all relevant metrics. All equipment are calibrated before the measurements to de-embed any cable losses or dispersion and ensure that the reference planes are at the DUT circulator's ports.

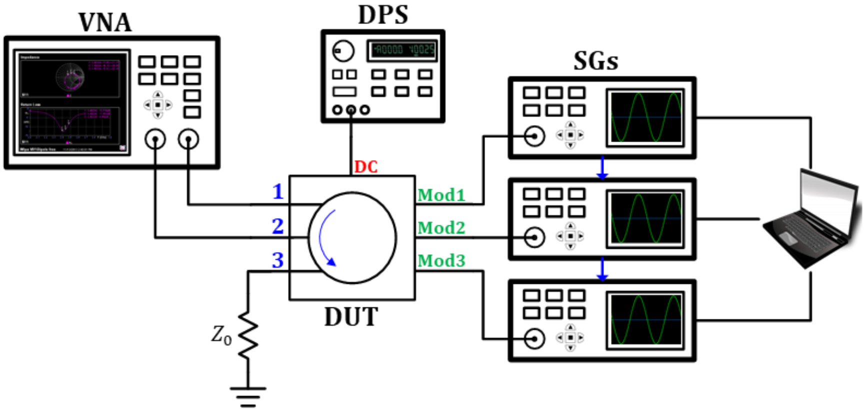

Figure 62: *S*-parameters experimental setup.

Fig. 62 shows a block diagram of the experimental setup used to measure the S-parameters. The circulator's S-matrix is constructed from the results of three identical two-port measurements, where in each, two of the DUT circulator's ports are connected to a two-port VNA and the third port is terminated with a matched load.

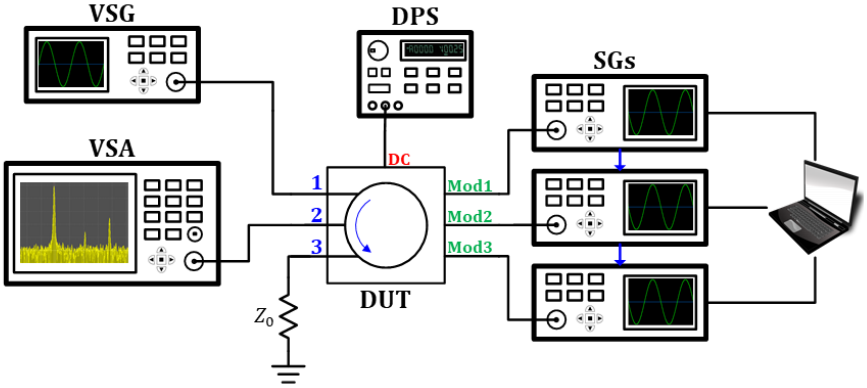

Figure 63: Spurious emission experimental setup.

Fig. 63 shows a block diagram of the experimental setup used to measure the spurious emission. An input signal at the circulator’s center frequency is generated via an SG and applied to one of the circulator’s ports, say port 1. Then, the spectrums at ports 2 and 3 are measured consecutively by connecting one of them at a time to a VSA while terminating the other with a matched load. The results are then normalized to the output power of the SG.

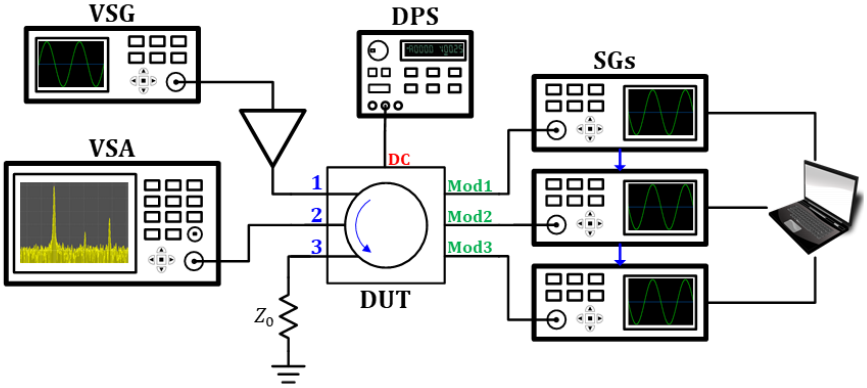

Figure 64: P1dB and IX20dB experimental setup.

Fig. 64 shows a block diagram of the experimental setup used to measure the power handling, namely, P1dB and IX20dB. These metrics were expected from simulations to be larger than the maximum output power of the SG. Therefore, an Amp was used to provide a sufficient gain for the SG output such that it compresses the circulator. Also, the Amp itself was chosen such that its compression point is guaranteed to be larger than the expected P1dB and IX20dB of the circulator. The SG is configured to generate a signal at the circulator's center frequency, which is then injected to one of the circulator's ports, say port 1. The input power is swept and the output powers at ports 2 and 3 are measured consecutively by connecting them one at a time to a VSA while terminating the other with a matched load.

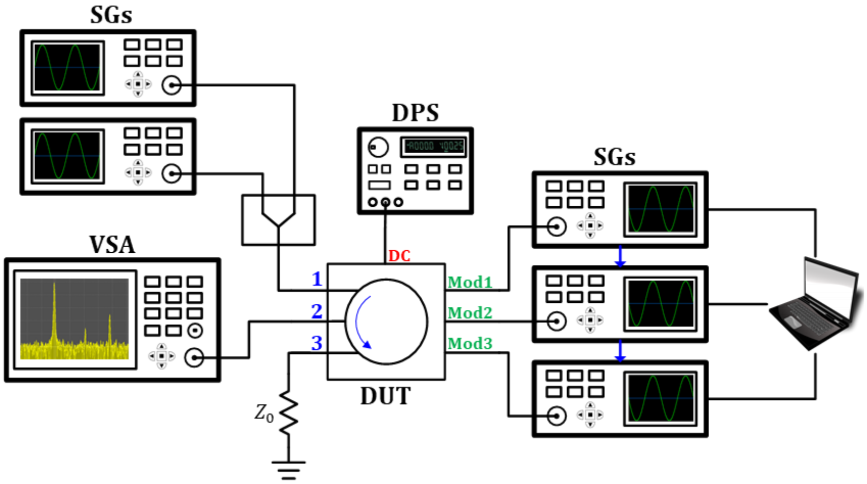

Figure 65: IIP3 experimental setup.

Fig. 65 shows a block diagram of the experimental setup used to measure the linearity, namely, IIP3. Two SGs are configured to generate two tones offseted from the circulator's center frequency by a certain desired amount. The two tones are combined using a power combiner and are then fed to one of the circulator's ports, say port 1. The power of both tones is then identically swept and the output power at port 2 (the through port) of the fundamental and third-order IMP is recorded while port 3 (the isolated port) is terminated with a matched load.

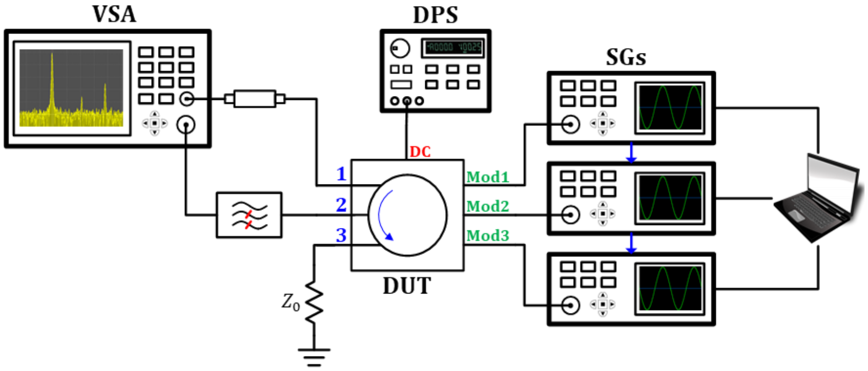

Figure 66: NF experimental setup.

Fig. 66 shows a block diagram for the experimental setup used to measure the NF based on the Y factor method. A 6 dB ENR source is connected to one of the circulator's ports, say port 1, and DC biased at 28 Volt. Port 2 (the through port) is then connected to a VSA through a high-pass filter with a cut-off larger than the modulation frequency but much smaller than the circulator's center frequency in order to reject any residual leakage from the modulation signals which may overload the VSA when configured for such sensitive measurement. The NF calculations are then performed using the VSA itself. Notice that the DC bias of the ENR is generated from the VSA itself and that it is calibrated using the same VSA before measuring the NF of the DUT itself.

B. Differential Current-Mode Bandpass/Wye Topology

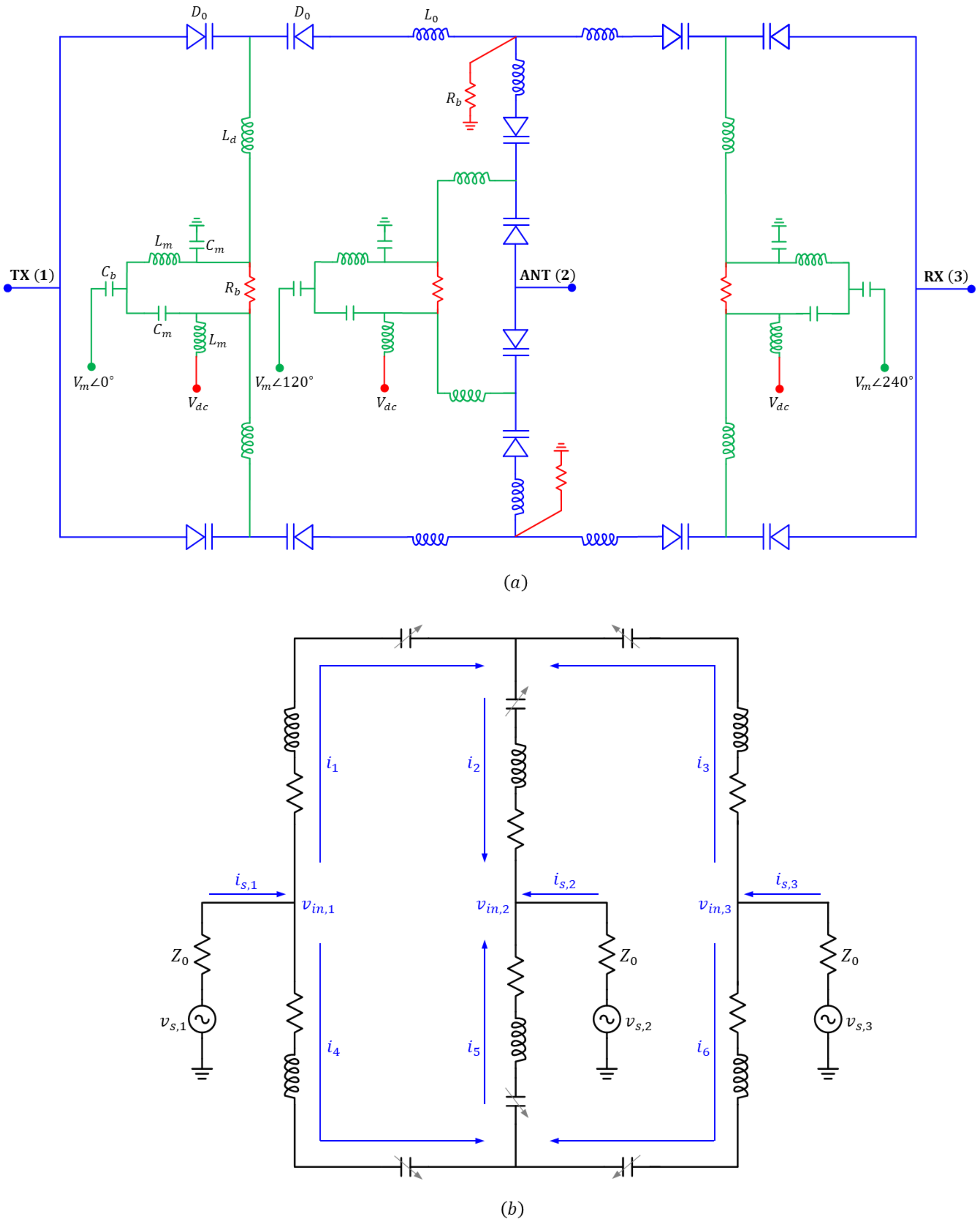

(a)

(b)

Figure 67: Current-mode bandpass/wye topology. (a) Complete schematic. (b) Small-signal model.

In this appendix, we present the analysis of the current-mode bandpass/wye topology. Fig. 67(a) shows the complete circuit implementation of this circuit, which consists of two single-ended bandpass/wye topologies connected in parallel. The differential modulation signals are generated through *LC* baluns (L_m and C_m) from three sources. Recall that these sources have the same amplitude V_m and frequency f_m but their phases increase by 120 deg in the clockwise direction. Large resistors R_b are used for DC biasing and the bias voltage itself V_{dc} is injected through the shunt inductance of the modulation baluns. Also, recall that each single-ended circuit consists of three series *LC* tanks realized using inductors L_0 and a pair of varactors D_0. The varactors are in common-cathode configuration and the common node is connected to an inductor L_d so that they form together a bandpass resonance at f_m, allowing the modulation signal to pass through while, at the same time, prohibiting the RF signal from leaking out of the delta loop. Under the small-signal assumption, Fig. 67(a) can be simplified as shown in Fig. 67(b), where the TX, RX, and ANT ports are replaced by voltage sources with an impeance Z_0. Also, the common-cathode varactors and the DC/modulation network are replaced by varcaps, the instantaneous capacitance of which is given by (4.4). Applying Kirchhoff's laws to the *n-th* tank, we get the following differential equations which govern the constituent single-ended circulators

$$L_0\bar{i}''_{SE1} + R_0\bar{i}'_{SE1} + \frac{1}{3C_0}\bar{\bar{E}}\left(\sigma\bar{\bar{U}} - \rho\bar{\bar{C}}_c\right)\bar{i}_{SE1} = \frac{1}{3}\bar{\bar{E}}\bar{v}'_{in} \tag{1}$$

$$L_0\bar{i}''_{SE2} + R_0\bar{i}'_{SE2} + \frac{1}{3C_0}\bar{\bar{E}}\left(\sigma\bar{\bar{U}} - \rho\bar{\bar{C}}_c\right)\bar{i}_{SE2} = \frac{1}{3}\bar{\bar{E}}\bar{v}'_{in}\,, \tag{2}$$

where $\bar{i}_{SE1} = \{i_1, i_2, i_3\}$ and $\bar{i}_{SE2} = \{i_4, i_5, i_6\}$ are the vectors of the tank currents of constituent single-ended circulators, respectively, $\bar{v}_{in} = \{v_{in,1}, v_{in,2}, v_{in,3}\}$ is the vector of the input voltages, and

$$\sigma = \frac{1}{\sqrt{1-\left(\Delta C/C_0\right)^2}} \tag{3}$$

$$\rho = \frac{2C_0}{\Delta C}\left(1-\frac{1}{\sqrt{1-\left(\Delta C/C_0\right)^2}}\right) \tag{4}$$

$$\bar{\bar{E}} = \begin{bmatrix} 2 & -1 & -1 \\ -1 & 2 & -1 \\ -1 & -1 & 2 \end{bmatrix}. \tag{5}$$

The tank currents $\bar{i}_{SE1}$ and $\bar{i}_{SE2}$ can, similarly, be expressed as a superposition of differential ($\bar{i}_d$) and common ($\bar{i}_c$) components as follows

$$\bar{i}_{SE1} = \bar{i}_c + \bar{i}_d \tag{6}$$

$$\bar{i}_{SE2} = \bar{i}_c - \bar{i}_d\ . \tag{7}$$

The port terminations of Fig. 67(b) also results in the following boundary equation

$$\bar{v}_{in} = \bar{v}_s - 2Z_0\bar{i}_c\ , \tag{8}$$

where $\bar{v}_s = \left\{v_{s,1}, v_{s,2}, v_{s,3}\right\}$ is the vector of the source voltages. Substituting (6)-(8) into (1) and (2) yields

$$\bar{i}''_d + \frac{R_0}{L_0}\bar{i}'_d + \frac{\sigma}{3L_0C_0}\bar{\bar{E}}\bar{i}_d - \frac{\rho}{3L_0C_0}\bar{\bar{E}}\bar{\bar{C}}_c\bar{i}_c = 0 \tag{9}$$

$$\bar{i}''_c + \frac{3R_0+2Z_0}{L_0}\bar{\bar{E}}\bar{i}'_c + \frac{\sigma}{3L_0C_0}\bar{\bar{E}}\bar{i}_c - \frac{\rho}{3L_0C_0}\bar{\bar{E}}\bar{\bar{C}}_c\bar{i}_d = \frac{1}{3L_0}\bar{\bar{E}}\bar{v}'_s\,. \tag{10}$$

Similar to the analysis in Chapter 4, (9) and (10) can be further simplified if we express $\bar{i}_d$ and $\bar{i}_c$ as a superposition of their in-phase, clockwise, and counter-clockwise modes as follows

$$\bar{i}_d = \bar{\bar{T}}\hat{i}_d \tag{11}$$

$$\bar{i}_c = \bar{\bar{T}}\hat{i}_c \,, \tag{12}$$

where $\hat{i}_d = \{i_{d,0}, i_{d,+}, i_{d,-}\}$ and $\hat{i}_c = \{i_{c,0}, i_{c,+}, i_{c,-}\}$ are the vectors of the modal currents for the differential and common components, respectively, and the operator $\bar{\bar{T}}$ is given by (3.19). If we further assume that $\bar{v}_s = \{1, 0, 0\}$ and recognize that the in-phase voltages $i_{d,0}$ and $i_{c,0}$ are both equal to zero, then substituting (11) and (4.13) into (9) and (10) results in

$$\begin{pmatrix} i''_{d,+} \\ i''_{d,-} \end{pmatrix} + \frac{R_0}{L_0}\begin{pmatrix} i'_{d,+} \\ i'_{d,-} \end{pmatrix} + \frac{\sigma}{L_0C_0}\begin{pmatrix} i_{d,+} \\ i_{d,-} \end{pmatrix} + \frac{\rho}{2L_0C_0}\begin{pmatrix} 0 & e^{-j\omega_m t} \\ e^{+j\omega_m t} & 0 \end{pmatrix}\begin{pmatrix} i_{c,+} \\ i_{c,-} \end{pmatrix} = 0 \tag{13}$$

$$\begin{pmatrix} i''_{c,+} \\ i''_{c,-} \end{pmatrix} + \frac{R_0 + 2Z_0}{L_0}\begin{pmatrix} i'_{c,+} \\ i'_{c,-} \end{pmatrix} + \frac{\sigma}{L_0C_0}\begin{pmatrix} i_{c,+} \\ i_{c,-} \end{pmatrix} + \frac{\rho}{2L_0C_0}\begin{pmatrix} 0 & e^{-j\omega_m t} \\ e^{+j\omega_m t} & 0 \end{pmatrix}\begin{pmatrix} i_{d,+} \\ i_{d,-} \end{pmatrix} = \frac{1}{3L_0}v'_{s,1} \,. \tag{14}$$

Fourier transforming (13) and (14) yields

$$\frac{I_{c,\pm}(\omega)}{V_{s,1}(\omega)} = \frac{\dfrac{j\omega}{3L_0}\left[(\omega \pm \omega_m)^2 - \dfrac{R_0}{L_0}j(\omega \pm \omega_m) - \dfrac{\sigma}{L_0C_0}\right]}{D_\pm(\omega)} \tag{15}$$

$$\frac{I_{d,\mp}(\omega \pm \omega_m)}{V_{s,1}(\omega)} = \frac{\rho}{6L_0^2C_0}\frac{j\omega}{D_\pm(\omega)} \,, \tag{16}$$

where $D_\pm(\omega)$ is given by

$$D_\pm(\omega) = \left(\frac{\rho}{2L_0C_0}\right)^2 + \left[-\omega^2 + \frac{R_0 + 2Z_0}{L_0}j\omega + \frac{\sigma}{L_0C_0}\right]\left[(\omega \pm \omega_m)^2 - \frac{R_0}{L_0}j(\omega \pm \omega_m) - \frac{\sigma}{L_0C_0}\right]. \tag{17}$$

In order to find the *S*-parameters, the source currents $\bar{I}_s = \{I_{s,1}, I_{s,2}, I_{s,3}\}$ are calculated as follows

$$\bar{I}_s = \bar{I}_{SE1} + \bar{I}_{SE2} = 2\bar{I}_c \,, \tag{18}$$

where $\bar{I}_c = \{I_{c,1}, I_{c,2}, I_{c,3}\}$ is given by

$$I_{c,n}(\omega) = e^{j(n-1)2\pi/3}I_{c,+}(\omega) + e^{-j(n-1)2\pi/3}I_{c,-}(\omega) \,. \tag{19}$$

Finally, the *S*-parameters can be calculated as follows

$$S_{11}(\omega)=1-\frac{4Z_0}{V_{s,1}(\omega)}\left[I_{c,+}(\omega)+I_{c,-}(\omega)\right] \tag{20}$$

$$S_{21}(\omega)=\frac{2Z_0}{V_{s,1}(\omega)}\left[I_{c,+}(\omega)+I_{c,-}(\omega)-j\sqrt{3}\left(I_{c,+}(\omega)-I_{c,-}(\omega)\right)\right] \tag{21}$$

$$S_{31}(\omega)=\frac{2Z_0}{V_{s,1}(\omega)}\left[I_{c,+}(\omega)+I_{c,-}(\omega)+j\sqrt{3}\left(I_{c,+}(\omega)-I_{c,-}(\omega)\right)\right]. \tag{22}$$

Due to the circulator's threefold rotational symmetry, the rest of the *S*-parameters can be found by rotating the indices as $(1,2,3)\rightarrow(2,3,1)\rightarrow(3,1,2)$. With proper choice of the circuit elements and modulation parameters, $I_{c,\pm}$ can be designed to destructively interfere at one port and sum up at the other, as required to achieve infinite isolation.

C. Composite Floquet Scattering Matrix Method

The sensitivity analysis of the CMOS circulator presented in Sec. XX of Chapter 7 was performed using an in-house so-called composite floquet scattering matrix (CFSM) frequency-domain numerical method. Compared to commercial circuit simulators, this method expedites the study of parasitic effects and the impact of synchronization errors on the relevant metrics of parametric circuits, thus giving an insight into the robustness of these circuits and allowing to optimize their performance rapidly. In this appendix, we briefly describe the underlying principles of this method. In general, the incoming and outgoing waves at each port of an LPTV multi-port network can be written as a superposition of infinite number of harmonics as follows

$$v^{\pm}(t) = \sum_{n=-\infty}^{\infty} v_n^{\pm} e^{j(\omega + n\omega_s)t} , \tag{23}$$

where $v_n^{\pm}$ are the corresponding Fourier series coefficients, and ω_s is the modulation frequency. In what follows, we take advantage of the fact that such linear time-periodic network can be treated as a linear *time-invariant* system with infinite number of harmonic ports per each physical port. This allows us to introduce a Floquet scattering matrix (FSM) which for a two-port system with the same real reference impedance Z_0 takes the following form

$$\begin{pmatrix} \mathbf{v}_1^- \\ \mathbf{v}_2^- \end{pmatrix} = \begin{pmatrix} \mathbf{S}_{11} & \mathbf{S}_{12} \\ \mathbf{S}_{21} & \mathbf{S}_{22} \end{pmatrix} \begin{pmatrix} \mathbf{v}_1^+ \\ \mathbf{v}_2^+ \end{pmatrix}, \tag{24}$$

where $\mathbf{S}_{ij}$ are square matrices relating the incoming and outgoing power waves at all frequencies of the physical ports *i* and *j*, i.e.

$$S_{ij,nm} = v_{i,m}^- \big/ v_{j,n}^+ , \tag{25}$$

where *n* and *m* denote the corresponding harmonics in the expansion (23). To obtain the FSM of an arbitrary circuit, the FSMs of each separate element are first aggregated into a single matrix relating the incoming and outgoing power waves at the terminals of all elements, hence

$$\mathbf{v}_i^- = \sum_j \mathbf{S}_{ij} \mathbf{v}_i^+ \, . \tag{26}$$

Next, the port indexes are split into two subsets corresponding to inner connections of the network and external ports denoted by small and capital indexes *p*, *q* and *P*, *Q*, respectively:

$$\begin{aligned} \mathbf{v}_p^- &= \sum_q \mathbf{S}_{pq} \mathbf{v}_q^+ + \sum_Q \mathbf{S}_{pQ} \mathbf{v}_Q^+ \\ \mathbf{v}_P^- &= \sum_q \mathbf{S}_{Pq} \mathbf{v}_q^+ + \sum_Q \mathbf{S}_{PQ} \mathbf{v}_Q^+ \end{aligned} \, . \tag{27}$$

Since the inner ports are, by definition, interconnected, the following additional relation can be found

$$\mathbf{v}_p^- = \sum_q \mathbf{F}_{pq} \mathbf{v}_q^+ \, . \tag{28}$$

For example, if only the inner ports 2 and 3 are directly tied together, then we have $\mathbf{v}_2^- = \mathbf{v}_3^+$ and $\mathbf{v}_3^- = \mathbf{v}_2^+$, leading to $\mathbf{F}_{23} = \mathbf{F}_{32} = \mathbf{I}$ with $\mathbf{I}$ being the identity matrix, and the rest of $\mathbf{F}_{pq}$ matrix being zero. Combining (27) and (28), we can find the CFSM relating the power waves only at the external ports as follows

$$\mathbf{v}_P^- = \sum_Q \tilde{\mathbf{S}}_{PQ} \mathbf{v}_Q^+ \, , \tag{29}$$

where

$$\tilde{\mathbf{S}}_{PQ} = \mathbf{S}_{PQ} + \sum_{p'q'} \mathbf{S}_{Pq'} [(\mathbf{F}_{pq}) - (\mathbf{S}_{pq})]^{-1}_{q'p'} \mathbf{S}_{p'Q} \, . \tag{30}$$

References

[1] Y. Niu, Y. Li, D. Jin, L. Su, and A. V. Vasilakos, “A survey of millimeter wave communications (mmWave) for 5G: opportunities and challenges,” *Wireless Netw.*, vol. 21, no. 8, pp. 2657-2676, Nov. 2015.

[2] S. Akoum, O. El Ayach, and R. W. Heath, “Coverage and capacity in mmWave cellular systems,” in *Proc. 46th ASILOMAR conf. Signals Syst. Comput.*, Pacific Grove, CA, USA, Nov. 2012, pp. 688-692.

[3] D. Korpi, J. Tamminen, M. Turunen, T. Huusari, Y. S. Choi, L. Anttila, S. Talwar, and M. Valkama, “Full-duplex mobile device: pushing the limits,” *IEEE Commun. Mag.*, vol. 54, no. 9, pp. 80–87, September 2016.

[4] A. Sabharwal, P. Schniter, D. Guo, D. W. Bliss, S. Rangarajan, and R. Wichman, “In-Band Full-Duplex Wireless: Challenges and Opportunities,” *IEEE J. Sel. Areas Commun.*, vol. 32, no. 9, pp. 1637–1652, Sept 2014.

[5] J. I. Choi, M. Jain, K. Srinivasan, P. Levis, and S. Katti, “Achieving single channel, full duplex wireless communication,” in *Proc. 16th Annu. Int. Conf. Mobile Comput. Netw. ACM,* Chicago, IL, USA, Sept. 2010, pp. 1-12.

[6] M. Duarte, C. Dick, and A. Sabharwal, “Experiment-driven characterization of full-duplex wireless systems,” *IEEE Trans. Wireless Commun.*, vol. 11, no. 12, pp. 4296-4307, Dec. 2012.

[7] A. Kord, D. L. Sounas, and A. Alù, “Achieving Full-Duplex Communication: Magnetless Parametric Circulators for Full-Duplex Communication Systems,” *IEEE Microw. Mag.*, vol. 19, no. 1, pp. 84-90, Jan. 2018.

[8] B. Debaillie, D. van den Broek, C. Lavín, B. van Liempd, E. A. M. Klumperink, C. Palacios, J. Craninckx, B. Nauta, and A. Pärssinen, “Analog/RF Solutions Enabling Compact Full-Duplex Radios,” *IEEE J. Sel. Areas Commun.*, vol. 32, no. 9, pp. 1662–1673, Sept 2014.

[9] J. Zhou, N. Reiskarimian, J. Diakonikolas, T. Dinc, T. Chen, G. Zussman, and H. Krishnaswamy, “Integrated full duplex radios,” *IEEE Commun. Mag.*, vol. 55, no. 4, pp. 142–151, Apr. 2017.

[10] M. Jain, J. I. Choi, T. Kim, D. Bharadia, S. Seth, K. Srinivasan, P. Levis, S. Katti, and P. Sinha “Practical, real-time, full duplex wireless,” in *Proc. 17th Annu. Int. conf. Mobile Comput. Netw. ACM*, Las Vegas, NV, USA, Sept. 2011, pp. 301-312.

[11] D. Bharadia, E. Mcmilin, and S. Katti, “Full duplex radios,” *ACM SIGCOMM Comput. Commun. Rev.*, vol. 43, no. 4, pp. 375-386, Sept. 2013.

[12] B. V. Liempd, B. Hershberg, B. Debaillie, P. Wambacq, and J. Craninckx, “An electrical-balance duplexer for in-band full-duplex with<-85dBm in-band distortion at +10dBm TX-power,” in *41st European Solid-State Circuits Conf. (ESSCIRC)*, pp. 176-179, 2015.

[13] L. Laughlin, M. A. Beach, K. A. Morris, and J. L. Haine, “Optimum single antenna full duplex using hybrid junctions,” *IEEE J. Sel. Areas Commun.*, vol. 32, no. 9, pp. 1653–1661, Sept. 2014.

[14] B. K. O'Neil and J. L. Young, “Experimental investigation of a self-biased microstrip circulator,” *IEEE Trans. Microw. Theory Techn.*, vol. 57, no. 7, pp. 1669-1674, 2009.

[15] J. A. Weiss, N. G. Watson, and G. F. Dionne, “New uniaxial-ferrite millimeter-wave junction circulators,” in *Proc. IEEE MTT-S Int. Microw. Symp. (IMS)*, Long Beach, CA, USA, 1989, vol. 1, pp. 145–148.

[16] A. Saib, M. Darques, L. Piraux, D. Vanhoenacker-Janvier, and I. Huynen, “Unbiased microwave circulator based on ferromagnetic nanowires arrays of tunable magnetization state,” *J. Phys. D, Appl. Phys.*, vol. 38, no. 16, pp. 2759–2763, Aug. 2005.

[17] L. P. Carignan, A. Yelon, D. Menard, and C. Caloz, “Ferromagnetic nanowire metamaterials: Theory and applications,” *IEEE Trans. Microw. Theory Techn.*, vol. 59, no. 10, pp. 2568–2586, Oct. 2011.

[18] S. A. Oliver, P. Shi, W. Hu, H. How, S. W. McKnight, N. E. McGruer, P. M. Zavaracky, and C. Vittoria, “Integrated self-biased hexaferrite microstrip circulators for millimeter-wavelength applications,” *IEEE Trans. Microw. Theory Techn.*, vol. 49, no. 2, pp. 385-387, 2001.

[19] J. Wang, A. Yang, Y. Checn, Z. Chen, A. Geiler, S. M. Gillette, V. G. Harris, and C. Vittoria, “Self-biased Y-junction circulator at Ku band,” *IEEE Microw. Wireless Compon. Lett.*, vol. 21, no. 6, pp. 292-294, 2011.

[20] T. Kodera, D. L. Sounas, and C. Caloz, “Magnetless nonreciprocal metamaterial (MNM) technology: application to microwave components,” *IEEE Trans. Microw. Theory Techn.*, vol. 61, no. 3, pp. 1030–1042, Mar. 2013.

[21] T. Kodera, D. L. Sounas, and C. Caloz, “Artificial Faraday rotation using a ring metamaterial structure without static magnetic field,” *Appl. Phys. Lett.*, vol. 99, Jul. 2011, Art. no. 03114.

[22] S. Wang, C. H. Lee, and Y. B. Wu, “Fully Integrated 10-GHz Active Circulator and Quasi-Circulator Using Bridged-T Networks in Standard CMOS,” *IEEE Trans. Very Large Scale Integr. (VLSI) Sys.*, vol. 24, no. 10, pp. 3184–3192, Oct. 2016.

[23] C.-H. Chang, Y.-T. Lo, and J.-F. Kiang, “A 30 GHz active quasicirculator with current-reuse technique in 0.18 μm CMOS technology,” *IEEE Microw. Wireless Compon. Lett.*, vol. 20, no. 12, pp. 693–695, Dec. 2010.

[24] G. Carchon and B. Nanwelaers, “Power and noise limitations of active circulators,” *IEEE Trans. Microw. Theory Techn.*, vol. 48, no. 2, pp. 316–319, Feb. 2000.

[25] D. L. Sounas, J. Soric, and A. Alù, “Broadband passive isolators based on coupled nonlinear resonances,” *Nat. Electronics*, vol. 1, pp. 113–119, Feb. 2018.

[26] L. Fan, J. Wang, L. T. Varghese, H. Shen, B. Niu, Y. Xuan, A. M. Weiner, and M. Qi, “An all-silicon passive optical diode,” *Science*, vol. 335, no. 6067, pp. 447–450, 2012.

[27] K. Gallo and G. Assanto, “All-optical diode in a periodically poled lithium niobate waveguide,” *Appl. Phys. Lett.*, vol. 79, no. 3, pp. 314-316, July 2001.

[28] S. Qin, Q. Xu, and Y. E. Wang, “Nonreciprocal components with distributedly modulated capacitors,” *IEEE Trans. Microw. Theory Techn.*, vol. 62, no. 10, pp. 2260-2272, Oct. 2014.

[29] N. Reiskarimian and H. Krishnaswamy, “Magnetic-free non-reciprocity based on staggered commutation,” *Nat. Commun.*, vol. 7, Apr. 2016.

[30] N. Reiskarimian, J. Zhou, and H. Krishnaswamy, “A CMOS Passive LPTV Non-Magnetic Circulator and Its Application in a Full-Duplex Receiver,” *IEEE J. Solid-State Circuits*, vol. 52, no. 5, pp. 1358-1372, May 2017.

[31] T. Dinc, M. Tymchenko, A. Nagulu, D. Sounas, A. Alù, and H. Krishnaswamy, “Synchronized conductivity modulation to realize broadband lossless magnetic-free non-reciprocity,” *Nat. Commun.*, vol. 8, no. 1, p. 795, Oct. 2017.

[32] A. Nagulu, A. Alù, and H. Krishnaswamy, “Fully-Integrated Non-Magnetic 180nm SOI Circulator with >1W P1dB, >+50dBm IIP3 and High Isolation Across 1.85 VSWR,” in *IEEE Radio Freq. Integ. Circuits Symp. (RFIC)*, Philadelphia, PA, USA, Jun. 2018.

[33] M. M. Biedka, R. Zhu, Q. M. Xu, and Y. E. Wang, “Ultra-Wide Band Non-reciprocity through Sequentially-Switched Delay Lines,” *Sci. Rep.*, vol. 7, Jan. 2017.

[34] M. M. Biedka, Q. Wu, X. Zou, S. Qin, and Y. E. Wang, “Integrated time-varying electromagnetic devices for ultra-wide band nonreciprocity,” in *IEEE Radio Wireless Symp. (RWS)*, Anaheim, CA, USA, Jan. 2018, pp. 80–83.

[35] N. A. Estep, D. L. Sounas, J. Soric, A. Alù, “Magnetic-free non-reciprocity and isolation based on parametrically modulated coupled-resonator loops,” *Nat. Phys.*, vol. 10, no. 12, pp. 923-927, Nov. 2014.

[36] N. A. Estep, D. L. Sounas, and Andrea Alù, “Magnetless Microwave Circulators Based on Spatiotemporally Modulated Rings of Coupled Resonators,” *IEEE Trans. Microw. Theory Techn.*, vol. 64, no. 2, pp. 502-518, Feb. 2016.

[37] A. Kord, D. L. Sounas, and A. Alù, “Magnetless Circulators Based on Spatio-Temporal Modulation of Bandstop Filters in a Delta Topology,” *IEEE Trans. Microw. Theory Techn.*, vol. 66, no. 2, pp. 911-926, Feb. 2018.

[38] A. Kord, D. L. Sounas, and A. Alù, “Pseudo-Linear Time-Invariant Magnetless Circulators Based on Differential Spatio-Temporal Modulation of Resonant Junctions,” *IEEE Trans. Microw. Theory Techn.*, vol. 66, no. 6, pp. 2731-2745, Jun. 2018.

[39] A. Kord, H. Krishnaswamy, and A. Alù, “Magnetless Circulators with Spur Suppression Based on *N*-Way Cyclic-Symmetric Time-Varying Networks," *Phys. Rev. Appl.*, under review since Apri 1st, 2019.

[40] A. Kord, D. L. Sounas, Z. Xiao, and A. Alù, “Broadband Cyclic-Symmetric Magnetless Circulators and Theoretical Bounds on their Bandwidth,” *IEEE Trans. Microw. Theory Techn.*, vol. 66, no. 12, Dec. 2018, pp. 5472-5481.

[41] A. Kord, M. Tymchenko, D. L. Sounas, H. Krishnaswamy, and A. Alù, “CMOS Integrated Magnetless Circulators Based on Cyclic-Symmetric Angular-Momentum Biasing,” *IEEE Trans. Microw. Theory Techn.*, under review since Sept. 28th, 2019.

[42] Y. Yu, F. Pop, G. Michetti, P. Kulik, M. Pirro, A. Kord, D. Sounas, A. Alù, and M. Rinadli, “Highly-linear Magnet-free Microelectromechanical Circulator,” *IEEE J. Microelectromech. Syst. (MEMS)*, in prep.

[43] D. L. Sounas, N. A. Estep, A. Kord, and A. Alù, “Angular-Momentum Biased Circulators and Their Power Consumption,” *IEEE Antennas Wireless Propag. Lett.*, vol. 17, no. 11, Nov. 2018, pp. 1963-1967.

[44] A. Kord, D. L. Sounas, and A. Alù, “Differential Magnetless Circulator Using Modulated Bandstop Filters,” in *Proc. IEEE MTT-S Int. Microw. Symp. (IMS)*, Honolulu, HI, USA, Jun. 2017.

[45] A. Kord, D. L. Sounas, and A. Alù, “Low-Loss Broadband Magnetless Circulators for Full-Duplex Radios,” in *Proc. IEEE MTT-S Int. Mircow. Symp. (IMS)*, Philadelphia, Pennsylvania, USA, Jun. 2018.

[46] C. Xu, E. Calayir, and G. Piazza, “Magnetic-free electrical circulator based on AlN MEMS filters and CMOS RF switches,” in *Proc. 31st IEEE Int. Conf. Micro Electro-Mech. Sys. (MEMS)*, Belfast, UK, Jan. 2018, pp. 755-758.

[47] Y. Yu, F. Pop, G. Michetti, P. Kulik, M. Pirro, M. Rinadli, A. Kord, D. Sounas, and A. Alù, “Radio Frequency Magnet-Free Circulators Basedon Spatiotemporal Modulation of Surface Acoustic Wave Filters,” *IEEE Trans. Microw. Theory Techn.*, in prep.

[48] C. Cassella, G. Michetti, M. Pirro, Y. Yu, A. Kord, D. Sounas, A. Alù, and M. Rinaldi, “Radio Frequency Angular Momentum Biased Quasi-LTI Nonreciprocal Acoustic Filters,” *IEEE Trans. Ultrason. Ferroelectr. Freq. Control (UFFC)*, under review since Feb. 6th, 2019.

[49] Y. Yu, G. Michetti, A. Kord, D. Sounas, F. V. Pop, P. Kulik, M. Pirro, Z. Qian, A. Alù, and M. Rinaldi, “Magnetic-Free Radio Frequency Circulator based on Spatiotemporal Commutation of MEMS Resonators,” in *Proc. 31st IEEE Int. Conf. Micro Electro-Mech. Sys. (MEMS)*, Belfast, UK, Jan. 2018, pp. 154-157.

[50] Y. Yu, G. Michetti, A. Kord, D. Sounas, F. V. Pop, P. Kulik, M. Pirro, Z. Qian, A. Alù, and M. Rinaldi, “2.5 GHz Highly-Linear Magnetic-Free Microelectromechanical Resonant Circulator,” in *Proc. IEEE Int. Freq. Cont. Symp. (IFCS)*, Olympic Valley, CA, May 2018.

[51] M. M. Torunbalci, T. J. Odelberg, S. Sridaran, R. C. Ruby, and S. A. Bhave, “An FBAR Circulator,” *IEEE Microw. Wireless Compon. Lett.*, vol. 28, no. 5, pp. 395-397, May 2018.

[52] R. Fleury, D. L. Sounas, C. F. Sieck, M. R. Haberman, and A. Alù, “Sound isolation and giant linear nonreciprocity in a compact acoustic circulator,” *Science*, vol. 343, pp. 516-519, Jan. 2014.

[53] Z. Yu and S. Fan, “Complete optical isolation created by indirect interband photonic transitions,” *Nat. Photon.*, vol. 3, pp. 91–94, Feb. 2009.

[54] H. Lira, Z. Yu, S. Fan, and M. Lipson, “Electrically driven nonreciprocity induced by interband photonic transition on a silicon chip,” *Phys. Rev. Lett.*, vol. 109, Jul. 2012, Art. no. 033901.

[55] K. Fang, Z. Yu, and S. Fan, “Photonic Aharonov–Bohm effect based on dynamic modulation,” *Phys. Rev. Lett.*, vol. 108, no. 15, Apr. 2012, Art. no. 153901.

[56] A. Kamal, J. Clarke, and M. H. Devoret, “Noiseless non-reciprocity in a parametric active device,” *Nat. Phys.*, vol. 7, no. 4, pp. 311–315, Apr. 2011.

[57] J. Kerckhoff, K. Lalumière, B. J. Chapman, A. Blasi, and K. W. Lehnert, “On-Chip Superconducting Microwave Circulator from Synthetic Rotation,” *Phys. Rev. Appl.*, vol. 4, no. 3, Sept. 2015.

[58] K. M. Sliwa, M. Hatridge, A. Narla, S. Shankar, L. Frunzio, R. J. Schoelkopf, and M. H. Devoret, "Reconfigurable Josephson Circulator/Directional Amplifier," *Phys. Rev. X*, vol. 5, no. 4, Nov. 2015.

[59] F. Lecocq, L. Ranzani, G. A. Peterson, K. Cicak, R. W. Simmonds, J. D. Teufel, and J. Aumentado, "Nonreciprocal Microwave Signal Processing with a Field-Programmable Josephson Amplifier," *Phys. Rev. Appl.*, vol. 7, no. 2, Feb. 2017.

[60] A. M. Mahmoud, A. R. Davoyan, and N. Engheta, "All-passive nonreciprocal metastructure," *Nat. Commun.*, vol. 6, no. 8359, July 2015.

Vita

Ahmed Kord received his B.S. and M.S. degrees in Electronics and Electrical Communications Engineering from Cairo University, Cairo, Egypt, in 2011 and 2014, respectively. From Dec. 2016 to Aug. 2017, he was with Eureka Aerospace Inc., Pasadena, CA, USA, as a Part-time Consultant, where he worked on antennas and high-power microwave sources. In 2015 and 2018, he held internship positions at Intel Labs, Intel Corp., Hillsboro, OR, USA, and Qualcomm Inc., Boxborough, MA, USA, respectively, where he worked on various RF circuits and communication systems. Since 2015, he has been involved with the startup company Silicon Audio/RF Circulator LLC, Austin, TX, USA, in the commercialization of his Ph.D. research on magnetless circulators. His research interests include multiple interdisciplinary topics in RF/microwave circuits, applied/computational electromagnetics, and photonics. He is particularly interested in investigating fundamental concepts in physics with emphasis on practical aspects to develop new devices with superior performance for a variety of applications, including wireless communications, biomedical systems, and quantum computing.

Dr. Kord was also a recipient of several prestigious awards including the Qulacomm Innovation Fellowship, the IEEE Microwave Theory and Techniques Society Graduate Fellowship, the IEEE Antennas and Propagation Society Doctoral Research Award, the Graduate Dean's Fellowship and the Douglas Wilson Fellowship, both from the University of Texas at Austin, the Graduate Fellowship from Cairo University, the Undergraduate Excellence Award from the Egyptian Ministry of Higher Education, and the First Place Award in the Texas Instruments Outstanding Student Designer Competition, the First Place Award in the Student Design Contest on Magnetless Parametric Circulators at the IEEE International Microwave Symposium in 2017, the First Place Award in the

Student Poster Competition at the IEEE Texas Symposium on Wireless Microwave Circuits and Systems in 2017, and multiple travel fellowships.

This dissertation was typed by Ahmed Kord.

Email: ahmed.kord@utexas.edu.